NRL Report 7388

Analysis of Experimental Data From a Scaled Ocean-Surveillance Radar

D. F. HEMENWAY

The Aerospace Radar Branch
Radar Division

March 7, 1972

NAVAL RESEARCH LABORATORY
Washington, D.C.

CONTENTS

ABSTRACT

To validate various theoretical models used in the design and specification of a proposed satellite-borne, ship-detection, ocean-surveillance radar, an airborne test-bed radar system has been developed and used to acquire experimental data. The major operating and performance parameters of the test-bed radar are either identical to or are scaled to the equivalent parameters of the satellite sensor.

The analysis of experimental data acquired with the test-bed radar indicates that the satellite radar system should meet the objective of automatically detecting ship targets with radar cross sections equal to or greater than 200 square meters. The analysis of the experimental data covers a variety of ships, ship aspects, ship lengths, sea states, and grazing angles. All of the ship-target data analyzed resulted in measures of processed-radar-video signal/(clutter plus noise) ratios ($S/(C + N)$) greater than 16 dB. The same data normalized for a satellite sensor system indicates that the 16-dB $S/(C + N)$ required for automatic detection would be realized for 200-square-meter ship targets.

The experimental data confirm that for the 0.016-second interpulse time period the sea clutter is for practical purposes completely decorrelated.

AUTHORIZATION

NRL Problem R02-46
Project PM 16-40 058C 2W44150000

Manuscript submitted January 10, 1972.

ANALYSIS OF EXPERIMENTAL DATA FROM A SCALED OCEAN-SURVEILLANCE RADAR [Unclassified Title]

SUMMARY

Objectives

An experimental, airborne, scaled radar sensor was used for the study, evaluation, and validation of a proposed satellite-borne ocean-surveillance radar. This report describes the scaled radar system (test-bed radar), the data acquisition program, and the initial results of the analysis of the experimental data.

The primary objective of the program was to provide experimental data that could be applied to the validation of the predicted performance of a proposed noncoherent, sidelooking, satellite-borne radar. Secondary objectives included the formation of a library of magnetic-tape records of wideband radar video for a variety of targets and sea states for the subsequent laboratory development of automatic-target-detection circuitry and logic, the design and development of a solid-state digital data processor, and the development and evaluation of components and subsystem elements for satellite-borne radars.

Conclusions

Detection and Signal/(Clutter Plus Noise) —Large and small ship targets were detected with the test-bed radar at steep (28°) and shallow (1.5°) grazing angles in sea states of 1 to 5. Analysis of the experimental data indicates that the proposed satellite-borne radar sensor will be capable of the required automatic detection of a fluctuating 200-square-meter ship target. The experimental data confirm that with appropriate data processing an output of greater than 16 db for the signal/(clutter plus noise) ratio can be consistently achieved for ship targets with radar cross sections of 200 or more square meters.

Sea-Clutter Decorrelation —In the NRL parametric analysis of satellite-borne ocean-surveillance radars it was postulated that, for the pulse repetition frequency selected, the sea clutter would be decorrelated. Experimental data acquired with the test-bed radar confirms that for the minimum 0.016-second interpulse period the sea clutter on a pulse-to-pulse basis is decorrelated.

Radar Cross-Section Measurements —Experimental radar cross-section measurements on small ship targets, ideally located so as to include the entire target within a single resolution cell, compare well with the cross sections of similar targets measured with a calibrated, precision radar.

Ocean Oil-Well Platforms and Icebergs —Offshore oil-well platforms and icebergs constitute shiplike radar targets which must be accounted for in an ocean-surveillance radar system. Analysis of a limited data sample for these two types of targets indicates that ship-sized radar cross sections are the normal expectation and that the population density was a high as 4 icebergs and 9 oil-well platforms per 100 square nautical miles.

Radar-Video Magnetic-Tape Library —Unprocessed wideband (chirp) radar video data for a variety of ship targets, target aspects, sea states, ranges, and grazing angles have been recorded on magnetic tape. The magnetic-tape library is made up of 32 rolls of tape recorded in flight, with each tape containing approximately 40 minutes of radar data.

INTRODUCTION AND BACKGROUND

Since 1967 the NRL Aerospace Radar Branch has been engaged in the study, analysis, specification, and development of systems, techniques, and components related to the development of satellite-borne radar sensor systems for the worldwide surveillance of surface ocean-ship traffic (1-9). One of the more recent studies (10) develops the philosophy, problems and solutions involved in the use of an aircraft-borne scaled radar sensor for the study, evaluation, and validation of a proposed satellite-borne ocean-surveillance radar sensor. Major factors considered in the subject scaling study are shown in Table 1.

Table 1
Factors Considered in Scaling the Radar System

Performance Considerations	Examples of Critical Parameters
Target Response	Frequency Pulse length Grazing angle Platform velocity Receiver bandwidth Power Target size
Clutter effects	Frequency Azimuth beamwidth Pulse length Grazing angle
Integration improvement	Azimuth beamwidth Pulse repetition frequency Platform velocity
Environmental factors	Frequency Grazing angle

This report describes the subject aircraft-borne test-bed radar, the data acquisition effort, and the initial results of the reduction and analysis of the experimentally acquired radar data.

The primary objective of the test-bed-radar program was to provide experimental data that could be applied to the validation of the theoretically predicted performance of a proposed noncoherent sidelooking satellite-borne radar. Additional objectives of the program included the formation of a library of radar video tapes for a variety of ship targets and sea conditions for subsequent laboratory clutter-target studies and particularly for the laboratory development and optimization of automatic target detection techniques, logic, and circuitry; the design and development of a solid-state digital radar data processor; and the development and evaluation of components and subsystem elements which were considered as having a potential for use in a satellite-borne radar system.

RADAR SYSTEM PARAMETERS

Major parameters for the satellite-borne ocean-surveillance radar (OSR) system, the reference system, and the scaled airborne test-bed radar are shown in Table 2. Two separate antennas and two corresponding sets of operating conditions apply for use of the test-bed radar. This marked departure from the reference system is a result of the scaling requirements and an intent to evaluate scaled performance at the two potentially most critical radar coverage regions: for the far-range shallow grazing angle and the near-range steep grazing angle. Resolution-cell dimensions for the satellite-borne system are approximately 50 ft in range depth by 4.3 n.mi. in arc length for the steep grazing angle and 50 feet in range depth by an arc length of 12 n.mi. at the 1.5° grazing angle. These two cells are the footprints for the near and far ranges of the OSR system and are nearly matched by the two separate antennas provided for the test-bed radar.

The test-bed radar is described in Appendix A.

AIRBORNE DATA ACQUISITION

Flight Operations

Two types of flight geometries were specified for data acquisition. One for radar data at steep grazing angles and short ranges (5 to 6 n.mi.) required that the aircraft fly 20-n.mi. data tracks with the alignment as indicated in Fig. 1a. The majority of the short-range, steep-grazing-angle flights were conducted with the project aircraft maintaining an altitude of 15,000 feet. On some flights the aircraft track was modified to provide the modified box pattern shown in Fig. 1b, which provided an opportunity to acquire data on the target bow, beam, and stern. When practicable the aircraft position and flight path was checked and related to shore-based navigational aids such as TACAN.

Table 2

System Parameters for the Proposed Satellite System* and for the Airborne Test-Bed Radar with Two Antennas

Frequency (MHz)	Effective Pulse Length (μsec)	Signal-to-Noise Ratio (dB)	Polarization	Transmitter Power		Pulse Compression Ratio	PRF (pps)	Vehicle Attitude (n.mi.)	Antenna							Radar Range (n.mi.)		Pulses Integrated		Power for Detection of a 200-m^2 Target	
									Length (ft)	Height (ft)	Beamwidth (deg)		Gain (dB)	Beam Depression Angle (deg)	Rotation Rate (rpm)						
				Av (W)	Peak (kW)						Azimuth	Elevation				Far: at 1.5°	Near: at 28°	Far Range	Near Range	Av (W)	Peak (kW)
Satellite System (With Maximum and Minimum Grazing Angles of 28° and 1.5°)																					
1230	0.1	16.0	Horiz	600	294	280:1	73	200	86.5	7.2	0.63	Shaped†	39.5	19.1		1103	391	179	64	600	294
Test-Bed Radar (Antenna and Operating Conditions for the 28° Grazing Angle)																					
1230	0.1	16.0	Horiz	18.75	15	200:1	62.5	1.98	1.2	2.0	44.0	19.5	13.3	20.0	5.3		5.3		64	.08	.06
Test-Bed Radar (Antenna and Operating Conditions for the 1.5° Grazing Angle)																					
1230	0.1	16.0	Horiz	18.75	15	200:1	39.1	2.47	5.4	3.0	10.7	38.0	22.2	1.0	0.3	68.5		179		6.6	8.4

*The single-side range extent of the swath width of the satellite system is 725 n.mi.

†The elevation beamwidth is shaped by applying the weighting function $\csc^{0.67}$ to the angle of depression relative to the boresight angle.

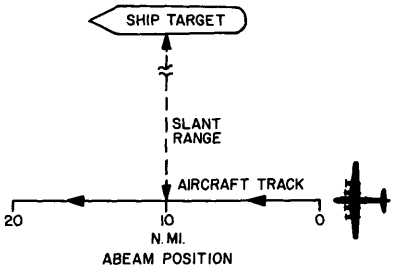

(a) Aircraft track for acquiring data at both steep and shallow grazing angles. For data at the steep grazing angles, the aircraft altitude was about 15,000 feet and the slant range was about 5 n.mi.; for data at the shallow grazing angles, the aircraft altitude was about 12,000 feet and the slant range was about 60 n.mi.

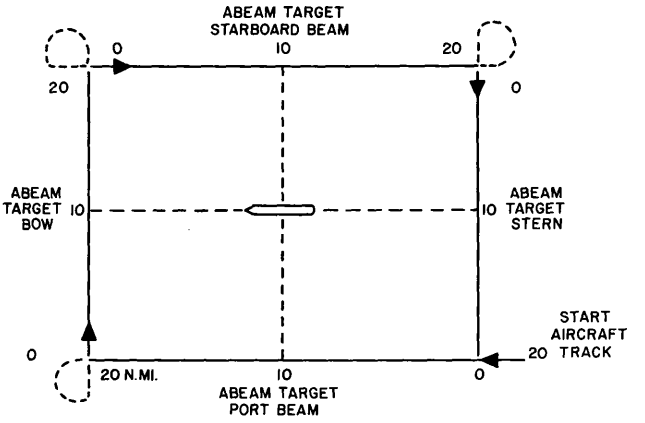

(b) Modified box pattern of aircraft tracks at steep grazing angles for acquiring data for bow, beam, and stern aspects

Fig. 1 (Unclassified)—Flight operations

The second type of flight path was that required for acquiring data at long range and shallow grazing angles (Fig. 1a). The majority of these flights were flown with the aircraft maintaining an altitude of 12,000 feet. The flight path specified was such that initial tracks were parallel to the track of the surface vessel and at closest approach had a slant range of 60 n.mi. Aircraft data tracks for the long-range data were also 20 n.mi. in length with the midpoint of the track coinciding with the target abeam position.

On all flights the targets were targets of opportunity. The routine procedure was to search for a target while the test-bed system was becoming thermally stabilized. After the targets course and heading were determined, the aircraft would take up station to provide the required data tracks. When the situation permitted, either at the beginning or the end of a series of data tracks, the aircraft would descend to 200 or 300 feet and pass within 1/4 n.mi. of the target for photographic documentation of the target and sea state.

Data Acquisition

The Ampex AR-500 wideband (6-MHz) video magnetic tape recorder was the primary data recorder. The wideband video channel of the recorder was used to record the unprocessed radar video, a marker pulse, the system reference trigger (PRF) pulse, and pulse-width-coded antenna-azimuth data. The format of the video data tape is shown in Fig. 2.

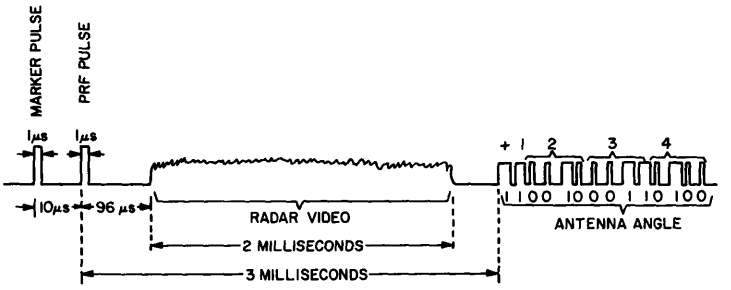

Fig. 2 (Unclassified)—Format of data recorded on video tape

An auxiliary channel of the AR-500 recorder was used for recording data on the system status; the aircraft altitude, velocity, and heading; and notations on the in-flight observation of target returns displayed on the several oscilloscopes and the PPI. A block diagram of the airborne data recording system is shown in Fig. 3.

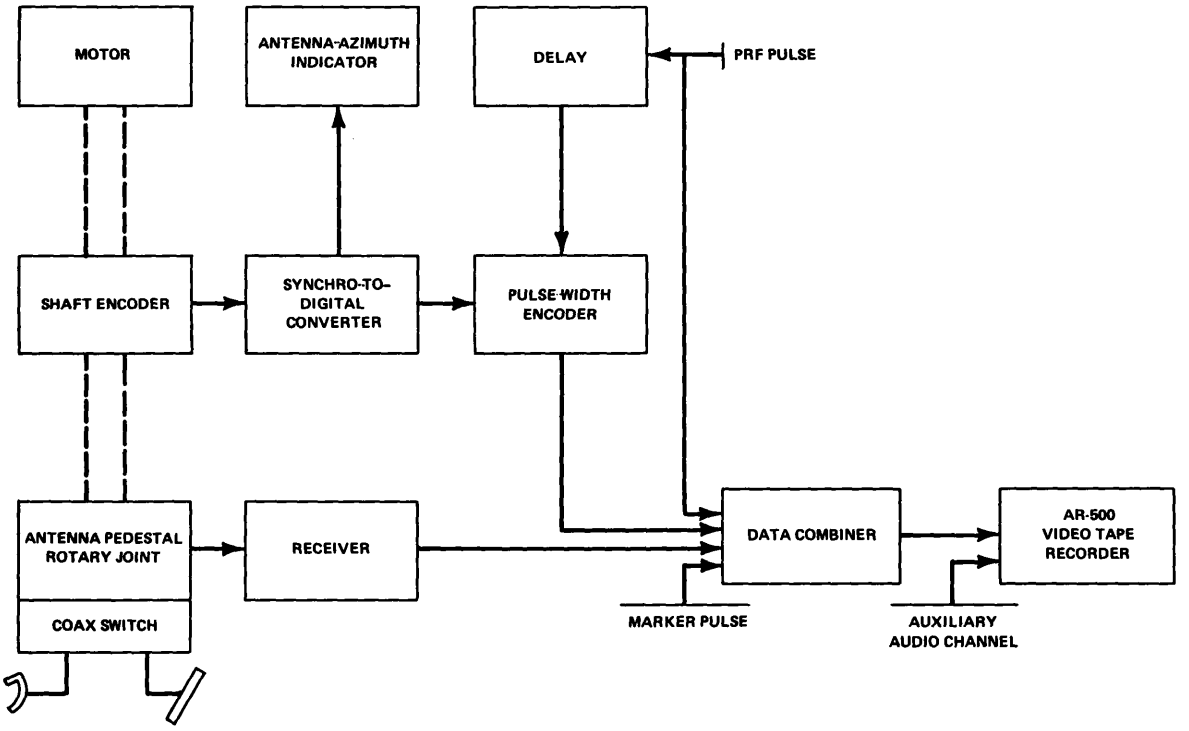

Fig. 3 (Unclassified)—The airborne data-recording system

During the initial hour of flight operations a routine of radar status checks and system calibration measurements were carried out. The video tape recorder was used to record some of the system calibration data such as pulse lengths, timing, minimum detectable signal, and receiver linearity. The first 2 to 3 minutes of record time for each video tape used in flight contains a signal to test, calibrate, and align the recorder.

At the start of a data run the AR-500 recorder was started and the unprocessed radar video data was recorded continuously for the duration of a nominal 20-n.mi. aircraft track past the target. For the initial detection of a selected target, for checks on the alignment of the aircraft track throughout a run, and for a track history to confirm target identification, it was necessary to start data runs with relatively high transmitter powers. During a run the transmitter power would be reduced incrementally up to the point of closest approach to the target. The incremental power changes with range require a normalization of power and signal levels to match the scaled values indicated in Appendix C for the points of closest approach (Tables C1 and C2).

At the end of a 20-n.mi. data run the tape recorder was stopped and additional system calibration measurements were made during the 5 to 10 minutes required for the aircraft to be turned and realigned for the reverse or next-scheduled data track. Two or more data runs were made for each target aspect.

The time available per roll of magnetic tape (40 to 43 minutes) was sufficient to record radar video data for four to six aircraft data runs. The airborne data-acquisition phase of this program has resulted in 32 rolls of magnetic tape with test-bed-radar video data.

The solid-state digital data processor was used regularly during data acquisition runs, with a real-time display of the processor data output being used as an in-flight monitor of processor performance. An A-scope display of the processed video data was occasionally recorded with an oscilloscope camera. Lengthy records of processed radar video were not recorded in flight. One purpose and intended use of the tape records is a source of unprocessed video which can on playback in a laboratory enviroment be processed by a variety of operations that may be evaluated during the development and optimization of an automatic detection capability.

DATA ANALYSIS

Target Identification

Test-bed-radar video data has been acquired on various targets. The data selected for analysis in this report is for a few unique or representative targets. The target data analyzed is, with one exception, for positively identified targets. An oil tanker approximately 400 feet long was the one unidentified ship target for which some data are presented. The data are included because they provide a good example of enhancement by the radar processor of a ship target in heavy sea clutter.

The necessity of having to acquire data on only targets of opportunity did present a problem of identification. Positive target identification was based on a combination of visual and radar checks on the target position relative to the aircraft before, during, and after data runs; on low-altitude photographic runs past the target to record topside structural details and particularly to photograph the vessel's name; and a check on the targets

physical characteristics with those listed in references such as Lloyd's Register of Ships (11, 12).

The determination of ship aspects for noncooperative targets at long range is an additional problem in determining the target status. The two sets of long-range (shallow-grazing-angle) data on ships included in the data analysis are the result of fortunate circumstances. In one case the target (*Tresfonn*, Fig. 4a) was observed anchored far offshore, and the ship heading was unchanged between initial and final observations. The second positively identified target observed at long range was a U.S. Coast Guard cutter (*Owasco*, Fig. 4b) which was cooperative and confirmed ship's heading by radio during the course of data runs.

(a) A bulk cargo carrier, the 557-foot *Tresfonn*

Fig. 4 (Unclassified)—Target ships whose aspects were known at long range

The majority of the targets encountered were large vessels from 400 to 700 feet long. These large vessels were of three types: oil tankers (Figs. 5a and 5b), bulk cargo carries (Fig. 4a), and container ships (Fig. 5c), with the oil tankers being the most frequently observed. Targets observed with lengths from 100 to 400 feet included tankers, coastal steamers, container ships, freighters, tugs, and fishing boats.

Unique targets for which data were acquired include Texas-tower structures such as the light station Chesapeake off of Norfolk, Virginia, and the oceanographic platform Argus Island (Fig. 6a) 25 miles southwest of Bermuda. Somewhat similar targets are a variety of oil-well platforms 30 to 40 miles off the Louisiana Coast (Fig. 6b). Other unique targets were two icebergs (Fig. 7).

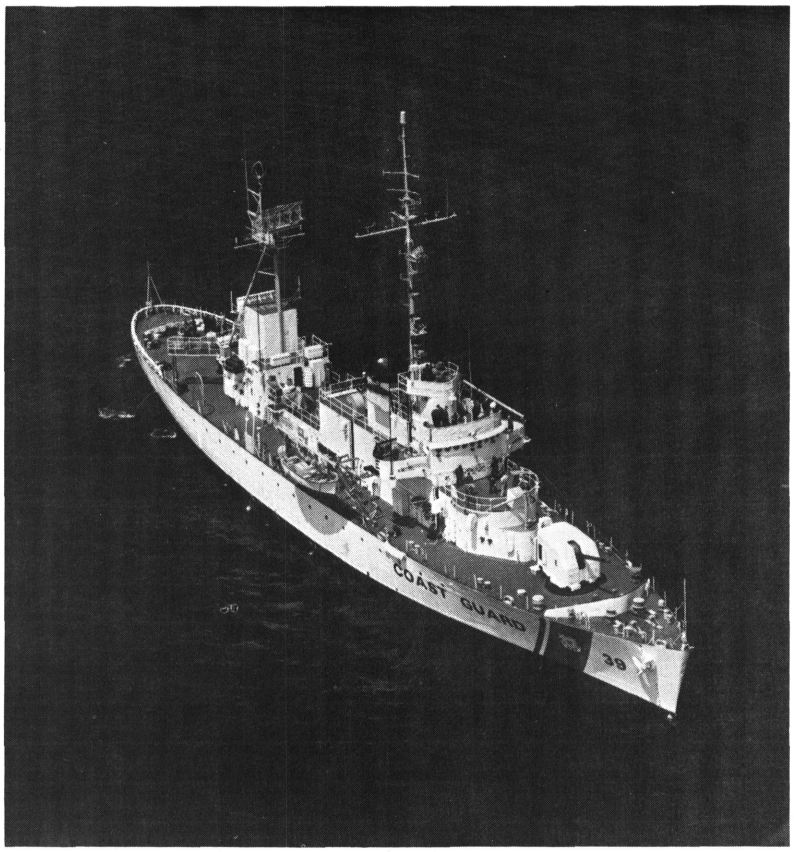

(b) The U.S. Coast Guard 254-foot high-endurance cutter, *Owasco*/ WHEC-39 (Coast Guard photograph)

Fig. 4 (Unclassified)—Target ships whose aspects were known at long range

For each class of target analyzed in this report additional, as yet unprocessed and analyzed data exist on targets of a similar class. As an example, this report includes data on the positively identified 128-foot stern trawler *Lady Maria* (Fig. 8a). Radar data was also acquired on a nearly identical but unidentified stern trawler (Fig. 8b). A cursory inspection of the radar video data from the unidentified trawler did not indicate radar characteristics significantly different from those of the *Lady Maria*. Because of more data as well as a positive identification, the *Lady Maria* was selected as the representative small-ship target for detailed analysis.

Each of the targets specifically referred to in the data analysis is listed in Table 3, and all of these targets are shown in Figs. 4 through 8.

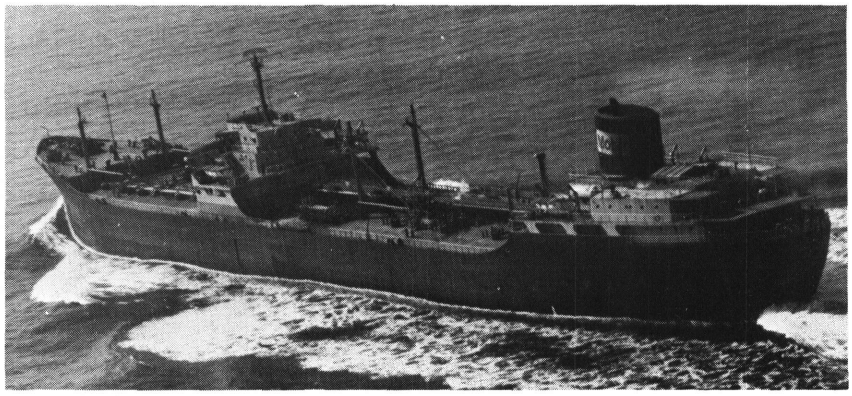

(a) An oil tanker, the 641-foot *Mobil Aero*

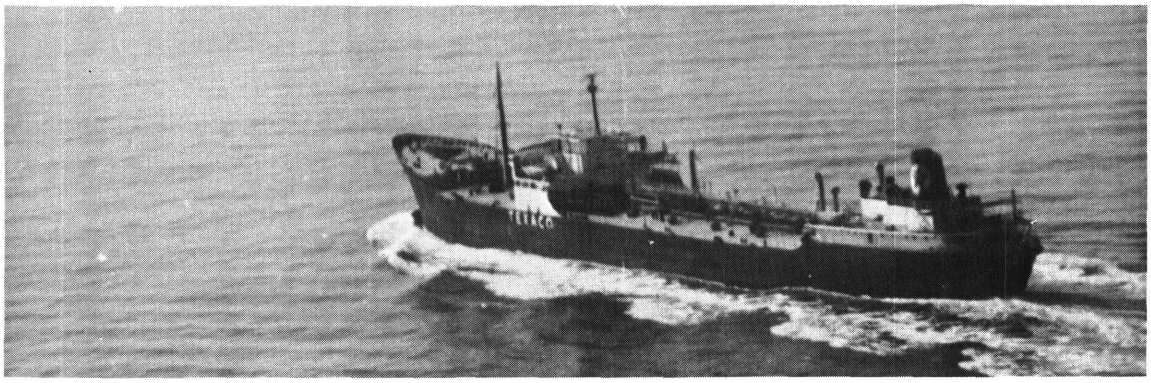

(b) An oil tanker, the *Texaco Wyoming*

(c) A container ship, the 695-foot *Atlantic Champagne*

Fig. 5 (Unclassified)—Large vessels used as targets

(a) *Argus Island*, an oceanographic research platform 25 miles southwest of Bermuda

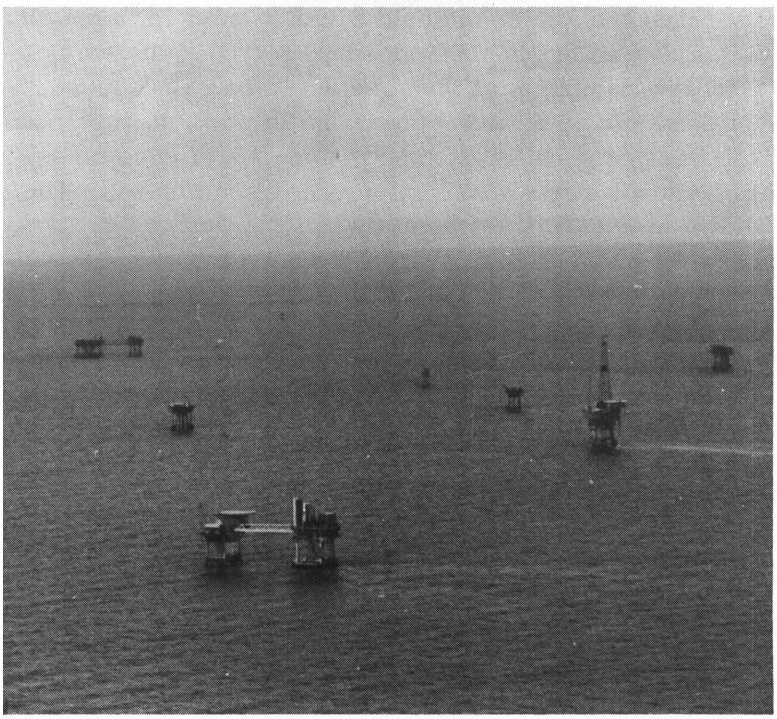

(b) A cluster of oil-well platforms off the Louisiana coast

Fig. 6 (Unclassified)—Offshore platforms used as targets

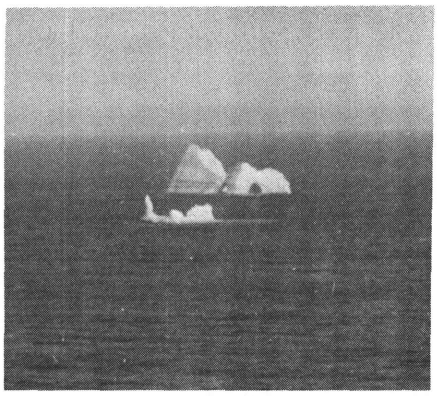

Fig. 7 (Unclassified)—The small (nearest) and large (more distant) icebergs used as targets

Data Reduction

The steps in reducing the unprocessed radar video data start with selection of a data run and playback of the video data on the ground-based Ampex AR-900 wideband magnetic tape recorder and reproducer. The laboratory equipment setup for the playback, display, and processing of the radar video tapes is shown in Fig. 9. Either the unprocessed radar video or one of 15 overlapping 10-mile range segments of processed video can be displayed on the PPI.

In reducing the data the sample-and-hold circuitry is set for a range-bin position known to include the desired target. On video-tape playback the start of a data load results in 1024 successive samplings of the signal level for a fixed-range resolution cell. Figure 10 is a representation of the successive azimuth positions (one position per radar pulse) at which the received signal is gated and sampled at a fixed range. The individual cell shown in Fig. 10 is not representative of a radar resolution cell. The azimuth dimension of the bin shown in Fig. 10 is representative of the time and arc length associated with successive sampling intervals, and is directly related to the dot symbol which represents the pulse-to-pulse progression of the antenna beam center as the antenna rotates.

The peak voltage sampled in each successive range bin is held for the interpulse interval, during which time that signal is processed by an analog-to-digital converter. Each successive data value is temporarily stored in the direct memory access unit. On command the data in the direct memory access is called and provides the driving signals for the XY plotter, a teleprinter, and a paper-tape punch.

The punched tape record, a binary-coded digital representation of the sampled video voltage levels, for both the unprocessed and the processed radar video, becomes the secondary source of data for additional processing on a Hewlett-Packard 2116B general-purpose computer or for processing on the larger CDC-3800 computers. The types of output obtained to date, many of which are included in this report, include

(a) The 128-foot *Lady Maria*

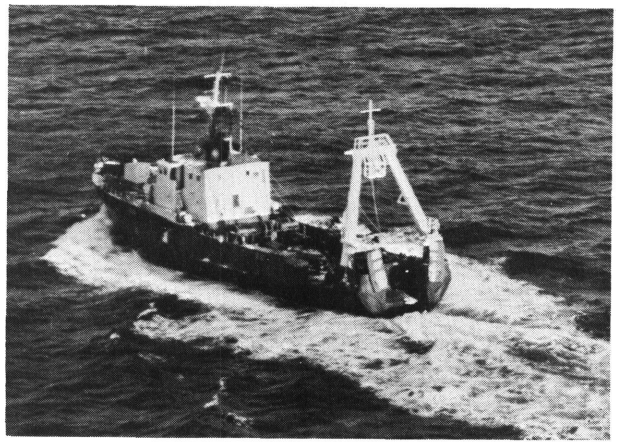

(b) Unidentified

Fig. 8 (Unclassified)—Stern trawlers used as targets

Table 3 (Unclassified)
General Information on Selected Test-Bed-Radar Targets

Identification	Registry	Length (ft)	Breadth (ft)	Gross Tons	Date Data Acquired	Sea State	Geographical Area of Operations	Comments
Stern trawler *Lady Maria*	Canada	128	28	434	2-25-71	3	Nova Scotia coast; 44° 18′N, 62° 30′W	Observed underway about 10 miles offshore; speed about 10 knots
High-endurance Coast Guard cutter *Owasco* WHEC/39	U.S.	254	43	1,563	7-27-71	1	Midway between Newfoundland and Greenland; 56° 30′N,51° 0′W	Station keeping; speed approximately 0 knots
Container ship *Atlantic Champagne*	France	696	92	15,351	2-25-71	3	Nova Scotia coast; 44° 18′N, 62° 0′W	Observed underway about 10 miles offshore; speed about 20 knots
Tanker *Texaco Wyoming*	U.S.	575	79	14,242	2-26-71	5	Near Boston; 42° 30′N, 70° 18′W	Unladen, riding high; speed about 10 knots
Tanker *Mobile Aero*	U.S.	641	84	18,616	2-26-71	5	Near Boston; 42° 30′N, 70° 18′W	Unladen, riding high; speed about 10 knots
Bulk carrier *Tresfonn*	Norway	557	70	13,471	2-23-71	4	Near Halifax, N.S.; 44° 26′N, 63° 24′W	At anchor
Ocean research platform Argus Island	U.S.	60	60	—	7-14-71 7-16-71	4 3	25 miles southwest of Bermuda; 31° 56′40″N, 65° 10′40″W	Platform 30 feet high with its base about 70 feet above the sea
Offshore oil-well platforms	U.S.	—	—	—	7-20-71 7-21-71	3 3	100 miles southwest of New Orleans; 28° 30′N, 91° 0′W	Data acquired on a single platform, a group of three, and a cluster of about 18
Icebergs	—	—	—	—	7-26-71	2	Newfoundland coast	Two icebergs: ≈ 100 and 250 feet high

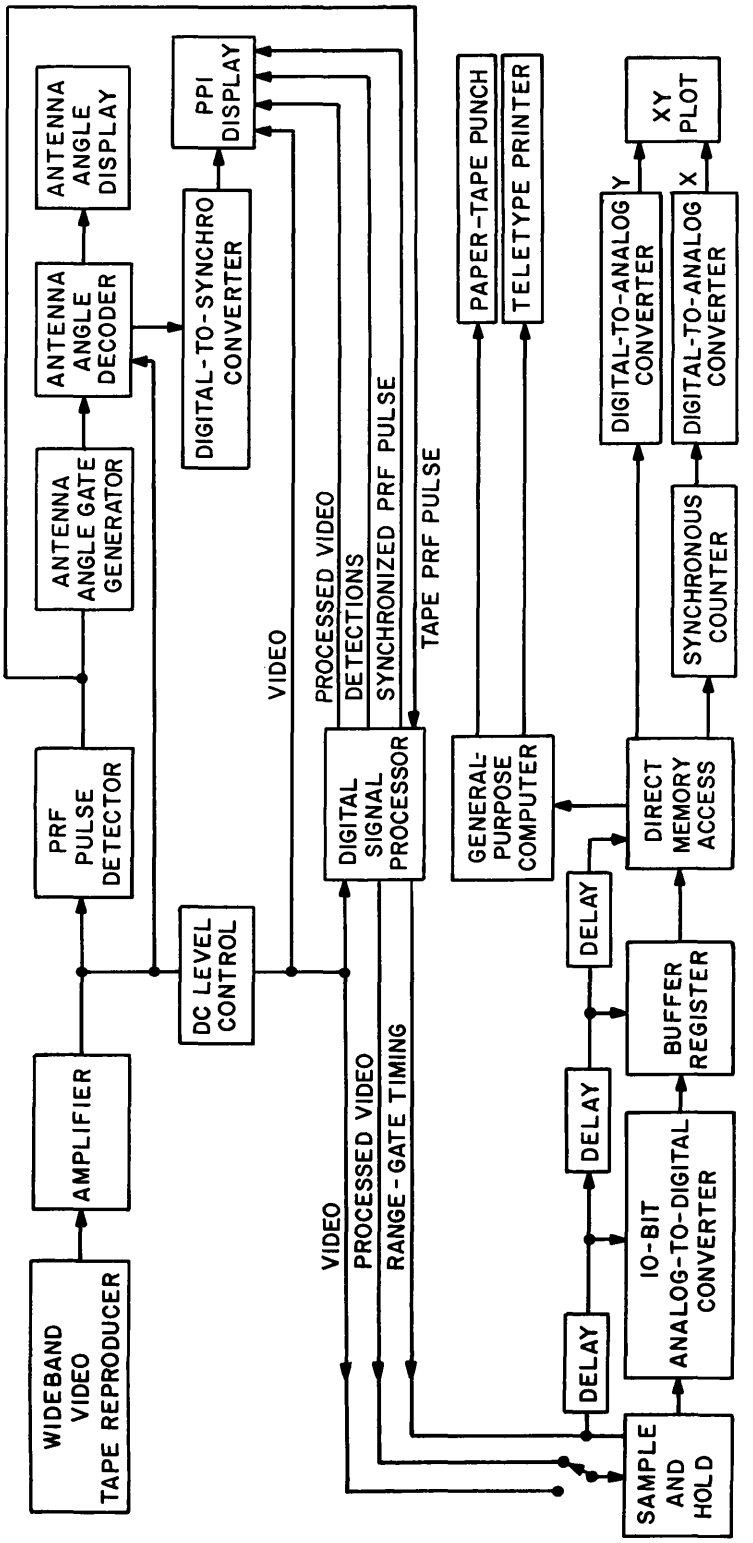

Fig. 9 (Unclassified)—Radar video tape playback and data reduction instrumentation

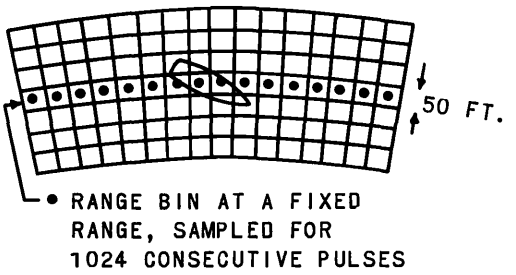

Fig. 10 (Unclassified)—A diagramatic representation of the successive sampling of data in range bins located at a fixed range

- machine-computer plots of
  - Unprocessed radar video: signal/(clutter plus noise)
  - Processed radar video: signal/(clutter plus noise)
  - Autocorrelation coefficients
  - Power spectrum

- computations of
  - Unprocessed video: rms signal/(clutter plus noise)
  - Processed video: peak signal/rms (clutter plus noise)
  - Normalized signal/(clutter plus noise) ratios
  - Experimental radar cross sections
  - Autocorrelation coefficients.

Signal/(Clutter plus Noise)

The signal/(clutter plus noise) ($S/(C + N)$) ratios serve as measures of the radar-system detection performance. By prior analysis (10) an output from a radar-signal processor with a $S/(C + N)$ of 16 dB or more is necessary to assure the required system performance. That required performance calls for automatic detection of targets with a 90-percent probability of detection of a fluctuating target whose average radar cross section is 200 square meters, in all sea states, and with a probability of false alarms of 10^{-10}.

Figures 11 through 24 (except Fig. 16) are reproductions of some of the computer/machine plots of unprocessed and processed radar video from which $S/(C + N)$ ratios have been calculated. The data plots shown in Figs. 11a and 11b represent the signal voltage sampled at a fixed radar range for 1024 successive radar pulses (data points) and displayed in sequence. The data in Fig. 11a are for unprocessed radar video and were acquired with the test-bed-radar antenna scanning at approximately 5 rpm. The resulting data plot shows the noiselike character of the successive sea-clutter returns for data sampled at a fixed range and a succession of 1024 azimuth antenna positions.

At about data point 410 the signal returns from the target, the trawler *Lady Maria*, become distinguishable from sea clutter and noise. Target returns associated with the trawler merge into the general clutter-noise level at about data point 465. The envelope formed by the target record reflects the modulation of the received target data by the azimuth pattern of the scanning radar antenna. The antenna scan rate was 32 degrees

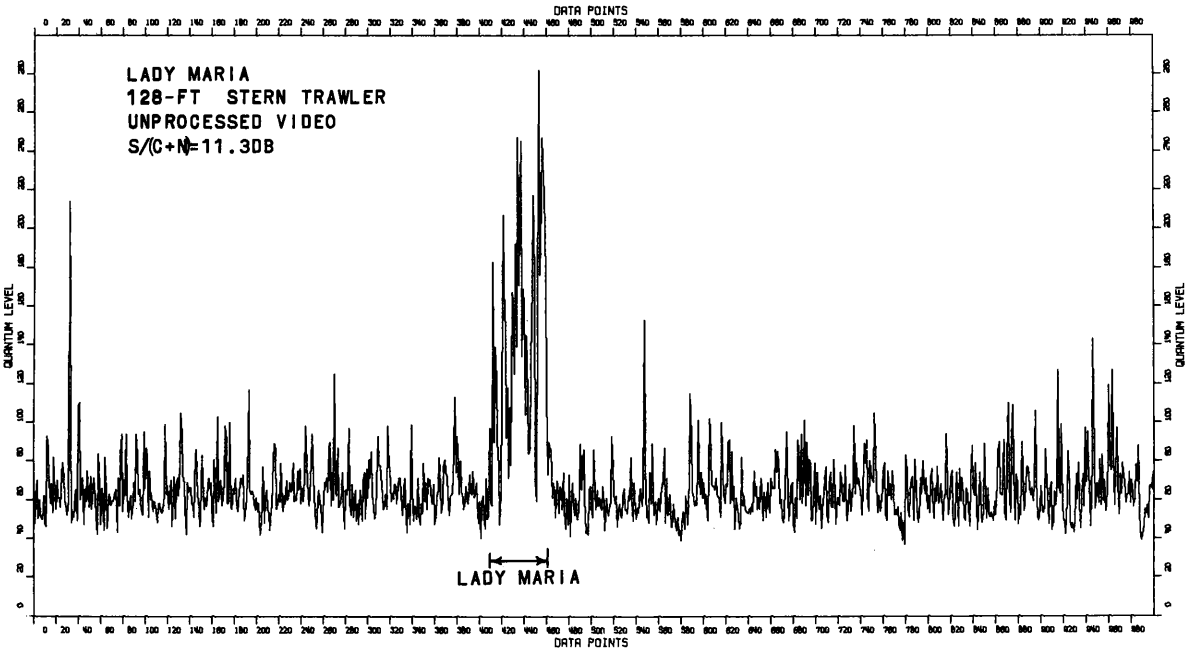

Fig. 11a —Unprocessed radar video for 1024 successive pulses sampled at a fixed range, showing sea clutter and radar returns from the stern trawler *Lady Maria*

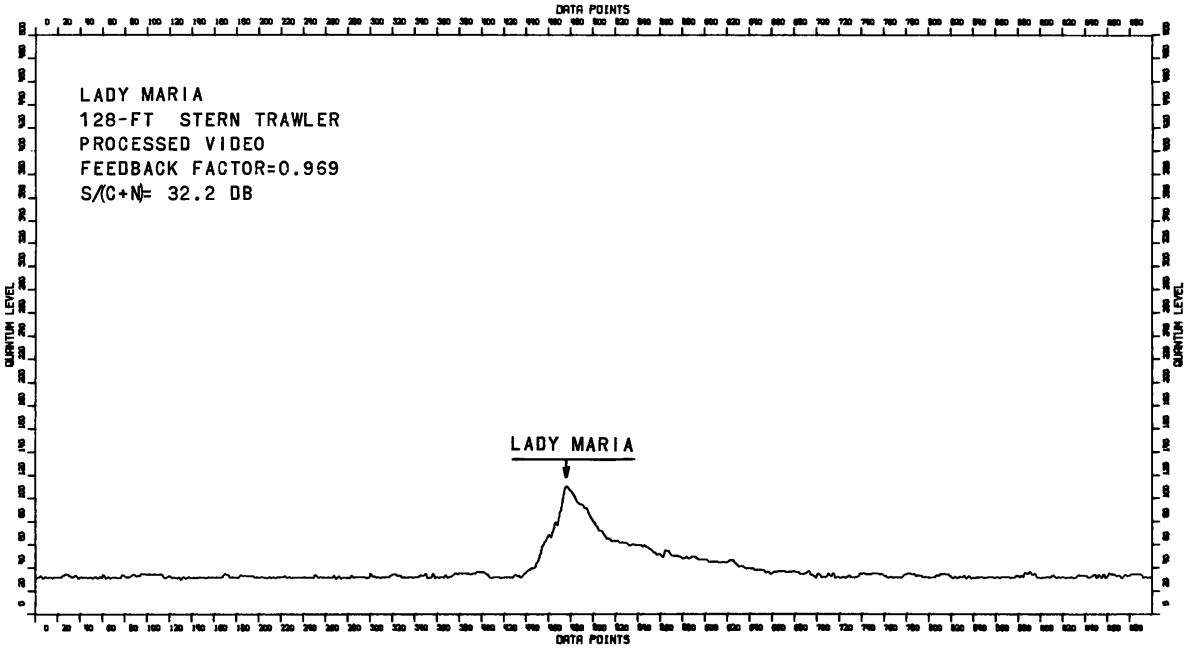

Fig. 11b —Processed radar video for the same data as in Fig. 11a

per second, and the antenna 3-dB azimuth beamwidth was 44 degrees. With a 62.5-pps pulse repetition frequency a discrete target would be illuminated by 86 pulses while within the 3-dB beamwidth of the scanning antenna. The width of the target data of about 55 pulses in Fig. 11a is then appropriate for a small ship target.

Table 4, contains a record of the successive pulse voltages associated with each data point of Fig. 11a. The development of the $S/(C + N)$ ratio for the data plotted in Fig. 11a is a combined manual-and-computer procedure. On the basis of an examination of a plot like that of Fig. 11a a range of successive pulses is selected for a clutter-plus-noise reference, and an estimate is made as to the number of successive pulses associated with the ship target. The selected limits for the clutter-plus-noise sample and target data pulses are incorporated in a computer routine for the computation of $S/(C + N)$ ratios.

In Fig. 11a, and Table 4, a data point is a PRF pulse and a quantum level is equivalent to 9.77 millivolts. The dc component for the data shown is equal to 0.36 volts. The root-mean-square (rms) value for the ac component of the clutter and noise, based on pulses 1 to 200 and 600 to 800 is 0.31 volt. The rms value for the ac component of the target signal, pulse 411 to 465, is 1.15 volts. The $S/(C + N)$ ratio for the unprocessed radar video data shown in Fig. 11a is then determined to be 11.3 dB (20 × log (1.15/0.31)).

Processing the same video data used to obtain Fig. 11a with the feedback integrator (digital signal processor in Fig. 9) produces the plot shown in Fig. 11b. The $S/(C + N)$ ratios for the processed data are based on the peak signal versus the rms value of the ac component of the clutter plus noise. The rms value of the processed clutter plus noise, from pulse 101 to 400, was determined to be 0.022 volt, and the peak processed target signal was measured as 0.92 volt. The ratio of the peak signal value to the rms clutter-plus-noise value was then found to be 32.2 dB (20 × log (0.92/0.022)).

The two $S/(C + N)$ values, 11.3 and 32.3 dB for unprocessed and processed radar video, are derived from experimental data, with the target being the stern trawler *Lady Maria*. The two ratios were based on data acquired at a slant range of 6.2 n.mi., at an aircraft altitude of 15,000 feet, and with a peak transmitter power of 416 watts. The target azimuth aspect was approximately 45°. Table C1 in Appendix C indicates that for the proper scaling relationship the power for a 15,000-foot altitude and a 6.2-n.mi. range should have been 100 watts instead of 416 watts. Radar cross sections and subsequent normalizing of power or target size were computed using the following form of the radar equation:

$$P_{av} = \frac{K\,(4\pi)^3\,\tau_c\,B_n\,N_0\,(\mathrm{PRF})\,R_s^4\,\left(\dfrac{S}{C+N}\right)_n\,L}{G^2\,\lambda^2\,S_i(n)\left[\sigma_T - \dfrac{\sigma_c\,\left(\dfrac{S}{C+N}\right)_n}{S_i(n_c)}\right]} \text{ watts,} \tag{1}$$

for which definitions of the units and associated relationships are presented in Appendix D.

Table 4
Pulse-to-Pulse Signal Levels for the Unprocessed Radar Video Shown in Fig. 11a.
(The second column in the table, as an example, gives data points 51 through 100.)
The blocked-in data are pulses 411 through 465 associated with the *Lady Maria*
in Fig. 11a. Values are quantum levels; 1 quantum level = 9.77 millivolts.

PAGE 1	1	2	3	4	5	6	7	8	9	10	11	12	13	14	15	16	17	18	19	20
1	48	72	87	83	54	72	81	99	40	99	51	48	58	71	74	69	53	59	54	58
2	63	55	81	70	58	62	71	69	59	170	86	74	63	65	63	105	71	50	53	81
3	70	66	51	55	42	47	85	95	62	282	64	58	52	49	55	82	76	66	55	57
4	50	71	79	61	44	48	63	71	51	176	55	89	49	64	62	67	61	52	86	83
5	60	61	60	57	57	60	56	69	45	212	65	62	102	57	45	53	50	51	68	59
6	52	51	62	63	77	65	50	70	71	247	57	52	96	51	55	62	66	53	63	70
7	50	42	54	71	48	58	53	60	50	225	61	59	68	69	63	54	59	51	47	54
8	50	84	59	66	61	57	69	58	52	219	57	47	67	58	71	57	77	49	65	55
9	62	67	57	69	65	43	93	68	97	175	55	57	67	53	77	69	58	59	69	80
10	48	47	54	55	55	54	78	47	59	113	67	61	65	71	52	76	60	52	44	119
11	46	66	48	46	53	69	78	52	57	73	58	54	71	66	48	79	68	68	49	78
12	93	61	58	81	44	67	73	62	183	90	44	63	63	66	68	52	61	85	64	75
13	87	44	58	64	55	71	62	65	90	86	61	68	61	66	74	49	49	90	57	127
14	69	82	54	53	57	64	55	82	139	86	55	70	61	86	56	75	59	63	65	82
15	58	64	53	103	81	87	57	67	123	61	52	87	51	74	56	62	64	62	127	57
16	68	45	55	59	89	90	63	53	91	69	56	48	100	85	81	68	94	63	66	76
17	53	61	62	65	87	57	55	59	77	64	59	71	72	73	63	60	68	91	63	97
18	82	63	99	70	55	74	98	78	47	51	93	52	63	58	47	75	52	53	99	67
19	63	57	63	57	58	60	78	81	64	70	77	55	58	60	61	65	63	49	57	52
20	55	59	67	61	63	129	76	74	113	68	63	63	68	51	60	52	71	82	90	73
21	70	59	55	68	59	64	59	72	207	53	58	46	67	48	57	55	75	110	48	63
22	61	61	61	98	79	62	63	62	169	67	62	46	90	54	74	52	51	67	42	79
23	61	64	70	91	58	87	61	52	147	65	46	58	91	79	67	56	46	53	60	71
24	56	65	46	58	54	56	68	62	92	55	54	52	58	95	59	47	53	92	85	69
25	73	63	61	59	62	58	67	63	118	74	58	47	85	63	59	44	74	109	65	58
26	79	71	72	100	58	58	58	63	71	54	52	44	60	49	78	53	63	73	48	62
27	72	57	50	56	70	74	67	84	108	45	51	51	67	61	54	39	46	49	45	63
28	60	83	68	55	60	60	71	113	78	61	62	42	45	67	49	48	76	73	48	74
29	55	94	71	66	62	45	71	74	167	47	66	44	61	69	63	37	59	68	43	58
30	52	54	62	63	69	65	62	93	162	73	55	39	57	47	68	83	71	47	49	70
31	59	70	77	71	64	63	52	78	125	41	55	53	52	43	54	75	63	56	73	63
32	214	62	105	61	66	67	60	63	192	56	53	54	45	61	59	55	51	52	60	56
33	101	94	94	54	79	97	71	80	139	69	62	45	48	50	68	51	49	90	79	61
34	48	62	73	60	59	58	59	64	247	58	60	62	82	91	98	65	66	74	57	78
35	54	51	68	68	61	52	43	61	171	52	82	54	57	79	63	71	62	54	45	69
36	51	58	55	71	60	68	58	55	202	61	60	47	62	60	79	72	55	59	62	88
37	62	62	42	68	75	51	57	60	245	50	49	71	55	94	68	49	46	76	73	54
38	65	50	69	73	65	58	47	67	134	50	69	115	54	58	71	81	71	77	56	43
39	49	58	64	49	76	65	99	59	169	63	55	93	53	73	65	66	88	73	97	39
40	109	69	66	53	58	49	64	58	160	89	50	64	54	101	65	55	66	65	69	42
41	110	59	66	61	66	58	49	73	104	65	56	61	55	57	52	48	62	62	95	46
42	60	94	58	71	59	47	57	64	145	76	53	57	53	90	66	52	79	66	73	55
43	68	83	57	117	71	65	55	63	115	86	66	60	58	62	89	71	56	59	59	53
44	71	63	51	65	98	61	50	75	84	61	65	57	54	81	79	63	44	69	46	57
45	47	65	83	63	79	49	71	61	86	43	57	101	75	79	91	80	61	106	80	50
46	65	58	86	64	69	70	52	63	131	45	65	77	62	49	62	70	74	70	143	67
47	59	53	61	62	57	74	47	69	172	42	153	63	67	50	54	63	52	51	81	67
48	75	52	61	58	63	50	58	58	217	65	77	74	55	63	80	71	48	49	55	66
49	62	95	46	55	79	76	53	48	175	67	91	61	61	79	72	55	53	55	68	74
50	56	66	52	61	94	81	79	99	70	56	54	69	55	47	71	62	89	67	67	55

MIN = 37 MAX = 282 02257124-10-76AA BEAM 6DB

Using Eq. (1) and experimental data acquired within the linear dynamic range of the receiver, the target radar cross section σ_T was computed (Table 5). The same form of the equation was then solved for a normalized $S/(C + N)$ ratio using the experimental radar cross section and a scaled power of 100 watts. The amount of processor gain measured prior to scaling was applied equally to normalized data. For the present example, prior to normalizing the processor gain was measured as 21.1 dB. After normalizing the unprocessed data, an rms $S/(C + N)$ ratio of 8.1 dB was computed; adding the equivalent processor gain of 21.1 dB results in a normalized processor $S/(C + N)$ ratio of 29.2 dB. This development of a normalized $S/(C + N)$ ratio for both the unprocessed and processed video data is supported by measurements in which the normalization process was bypassed and transmitter power levels were changed by 3-dB and 6-dB factors; the resulting unprocessed and processed $S/(C + N)$ ratios were within 1 dB of the theoretically predicted values.

Table 5
Radar Cross Sections Measured With the Test-Bed Radar (1.23612)

Target Ft. Length/Beam	Sea State	Range (n.mi.)	Grazing Angle (deg)	Aspect Angle* (deg)	Cross Section	
					Square Meters	dBsm
Lady Maria 128/28	3	4.5	33.3	90	660	28.2
	3	6.2	23.5	46	710	28.6
	3	8.1	17.5	48	340	25.3
Owasco 254/43	1	4.0	37.7	0	180	22.5
	1	4.9	30.6	180	255	24.1
	1	6.9	21.9	90	3140	35.0
	1	63.1	1.8	90	6530	38.1
Texaco Wyoming 578/79	5	6.0	24.4	34	1100	30.4
	5	6.6	22.0	30	1400	31.4
	5	7.9	18.1	25	1020	30.1
Mobil Aero 641/84	5	6.3	23.1	33	1770	32.5
	5	8.3	17.4	23	1880	32.7
Atlantic Champagne 696/92	3	9.9	14.9	19	1280	31.1
Tresfonn 557/70	4	61.5	1.8	25	3100	34.9
Argus Island	3	5.7	25.8	—	1910	32.8
	4	58.3	2.2	—	5130	37.1
Oil wells	3	5.7	25.8	—	7220	38.6
	3	58.3	1.8	—	1270	31.0
Small iceberg	2	4.5	33.3	—	320	25.0
Large iceberg	2	4.6	32.5	—	860	29.3

*Bow aspect is 0°, beam aspect is 90°, and stern aspect is 180°.

Thus with the $S/(C + N)$ ratios based on a normalized transmitter power, values of 8.1 and 29.2 dB respectively for the unprocessed and processed video are representative of values that would be expected with the referenced satellite radar sensor system. That is, the satellite radar system at a 200-n.mi. altitude and with 600 watts of transmitter power would for the same target, aspect, grazing angle, and sea state, produce approximately a 29.2-dB $S/(C + N)$ ratio at the output of the data processor.

The radar system performance measured for different targets can be compared by normalizing the radar cross sections of the specific targets to a 200-square-meter radar

target. Continuing with the same *Lady Maria* data of the preceding discussion, the computed radar cross section was 710 square meters. Thus the *Lady Maria* for that specific set of conditions had a cross section 5.5 dB greater than the 200 square meters of the reference target. Normalizing the target radar cross section to 200 square meters then results in an indicated $S/(C + N)$ ratio of −2.8 dB for the unprocessed video and 23.7 dB for the processed video.

Figures 12a through 12d are derived from the same data set, with Fig. 12a being for unprocessed video data and the remaining three plots being for varying integration feedback ratios. (This data set is for a different data run than that represented in Figs. 11a and 11b.) The rms $S/(C + N)$ ratio for the unprocessed video in Fig. 12a was measured as 10.6 dB. The $S/(C + N)$ ratios for the processed video was 21.9, 28.5, and 24.1 dB respectively for feedback factors of 0.938, 0.969, and 0.984. These feedback factors are representative of the feedback integration of 16, 32, and 64 successive pulses.

Figures 12b, 12c, and 12d show the effect of variation of the feedback integration factor on the $S/(C + N)$ ratios achieved and show that the greatest processor gain was in this instance achieved with a feedback factor of 0.969.

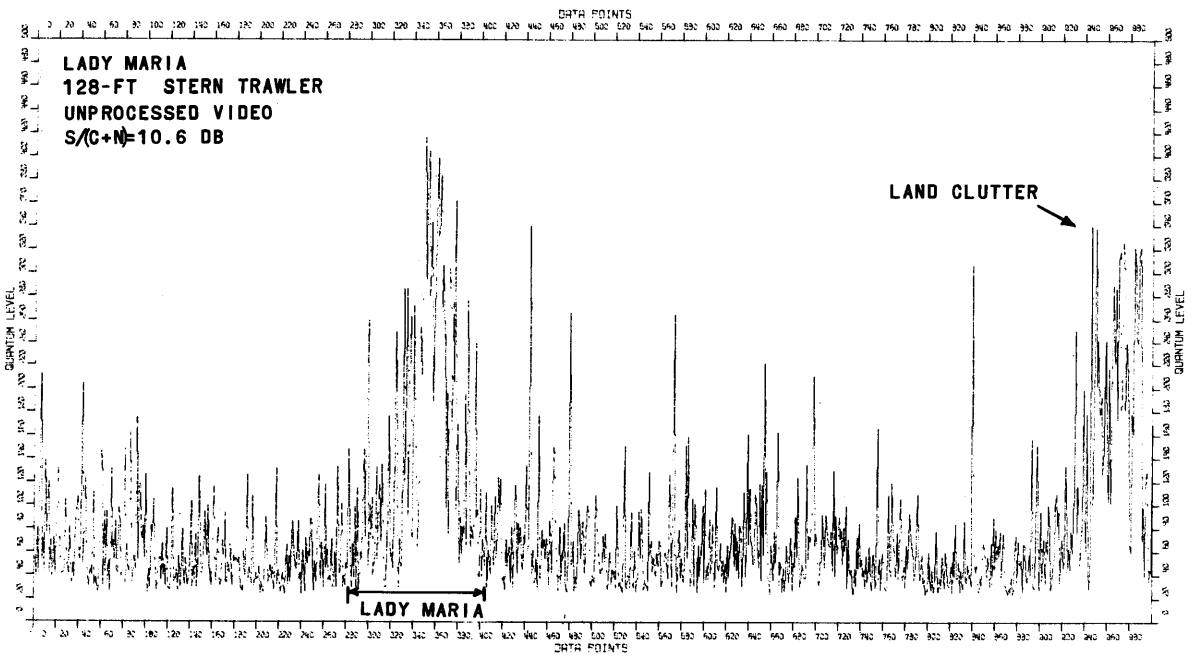

Fig. 12a —Unprocessed radar video data showing radar returns from sea clutter, the trawler *Lady Maria*, and land clutter at the extreme right of the data sample

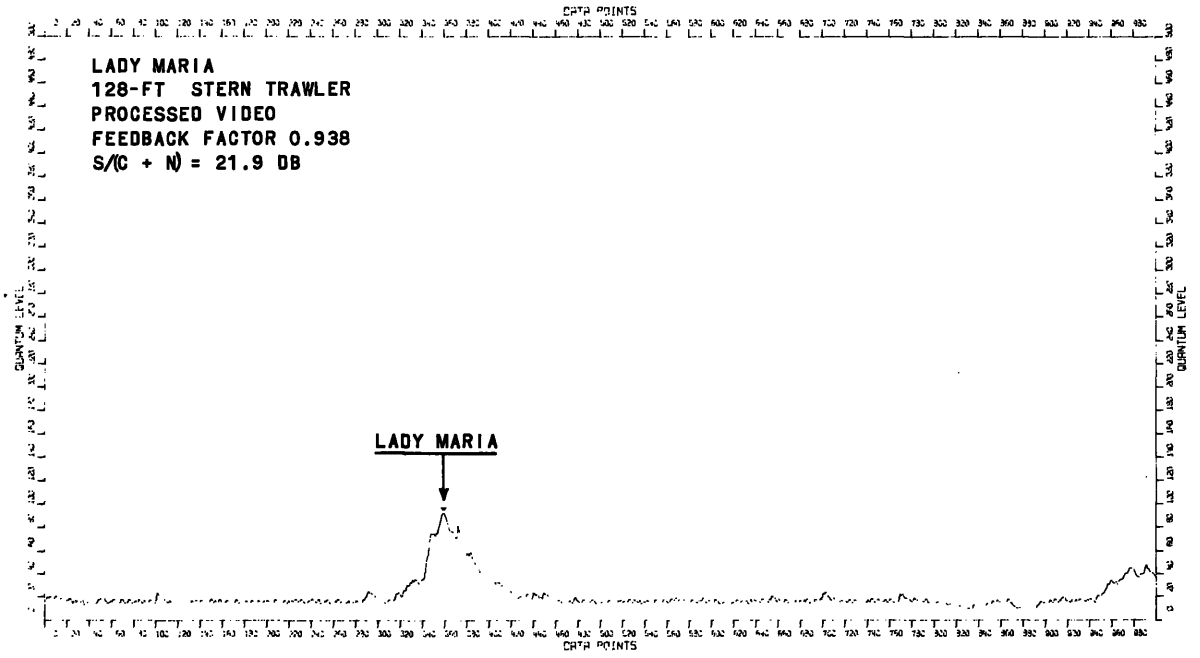

Fig. 12b —Processed radar video for the same data as in Fig. 12a with a feedback factor of 0.938

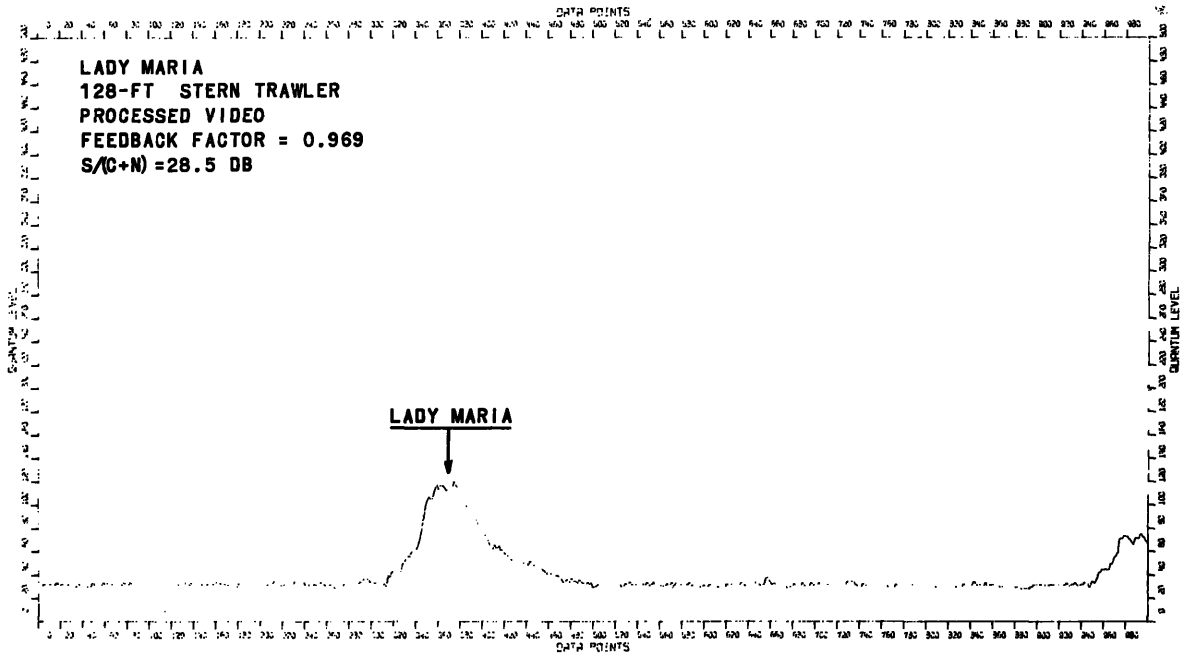

Fig. 12c —Processed radar video for the same data set as Fig. 12a with a feedback factor of 0.969

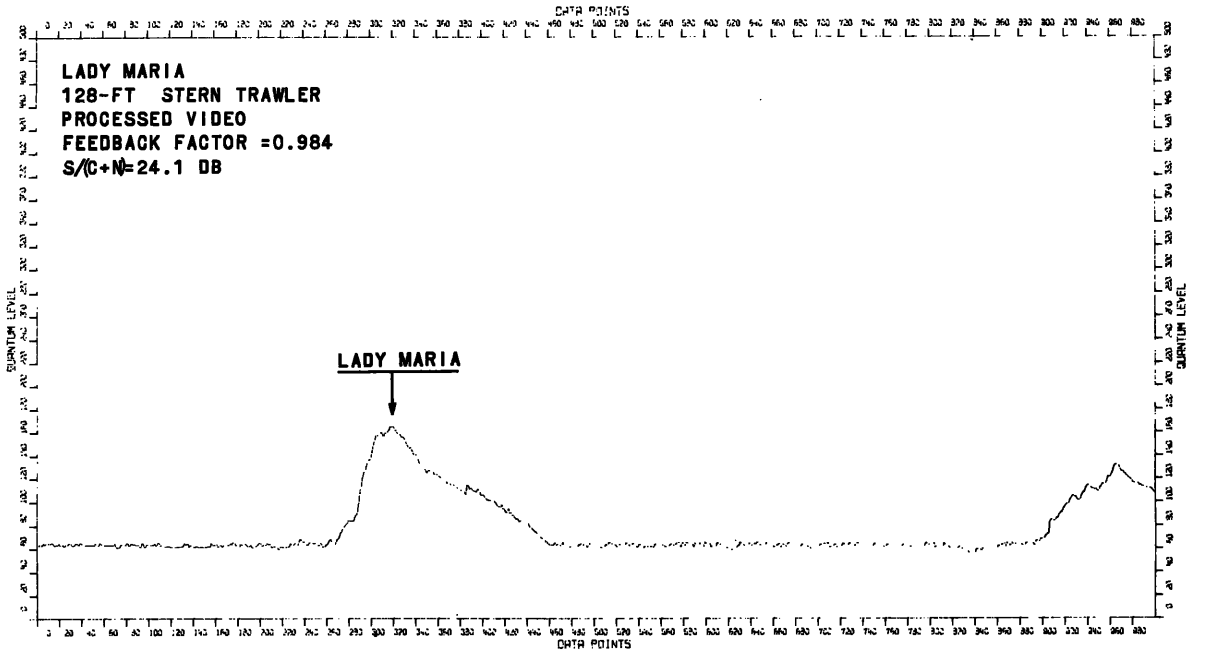

Fig. 12d —Processed radar video for the same data as in Fig. 12a with a feedback factor of 0.984

Figures 13a and 13b are of interest in that they show the system performance for a ship target immersed in saturation sea clutter. In the plot of unprocessed video data (Fig. 13a) the target can be discerned by the absence of the deep minima associated with the sea clutter. In the plot of the processed data (Fig. 13b) the target is more readily discerned; however the target-to-clutter ratio in this extreme case is too low to meet the requirements for automatic target detection.

Figures 14a and 14b are plots of unprocessed and processed radar video returns from the container ship *Atlantic Champagne*. Of interest in these plots are the spiky nature of the clutter and the appearance of land clutter at the extreme right in the plotted data.

Figures 15a and 15b are plots for the *Atlantic Champagne* which illustrate a part of the problem involved in detecting a ship target when it is operating in coastal waters. The source data for the two plots are identical. There is however an offset between the two plots; the ship returns for the unprocessed data are associated with data points 400 through 490, whereas for the processed data the ship returns are associated with data points 360 to 440. Inspection off these plots shows that the ship returns tend to be masked by land clutter. For the example shown the antenna was scanning in a clockwise direction, so that the ship returns were received first and then the land clutter returns. In this example, without prior knowledge as to the ship location, a positive distinction could not have been made between the ship returns and the land clutter. As presently configured the data-processing system is incapable of an automatic-target detection for a ship target near a land/sea interface when the geometry is such that the land clutter is included within the same resolution cell as the target.

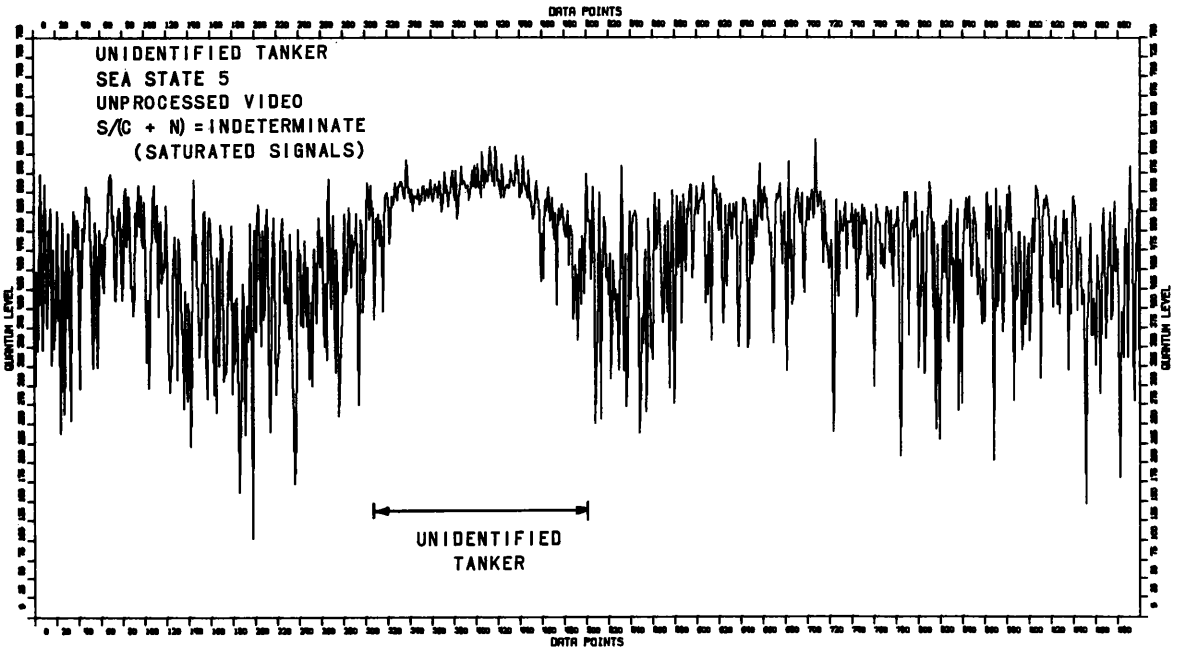

Fig. 13a —Unprocessed radar video data for an oil tanker about 400 feet long with the signal immersed in heavy sea clutter

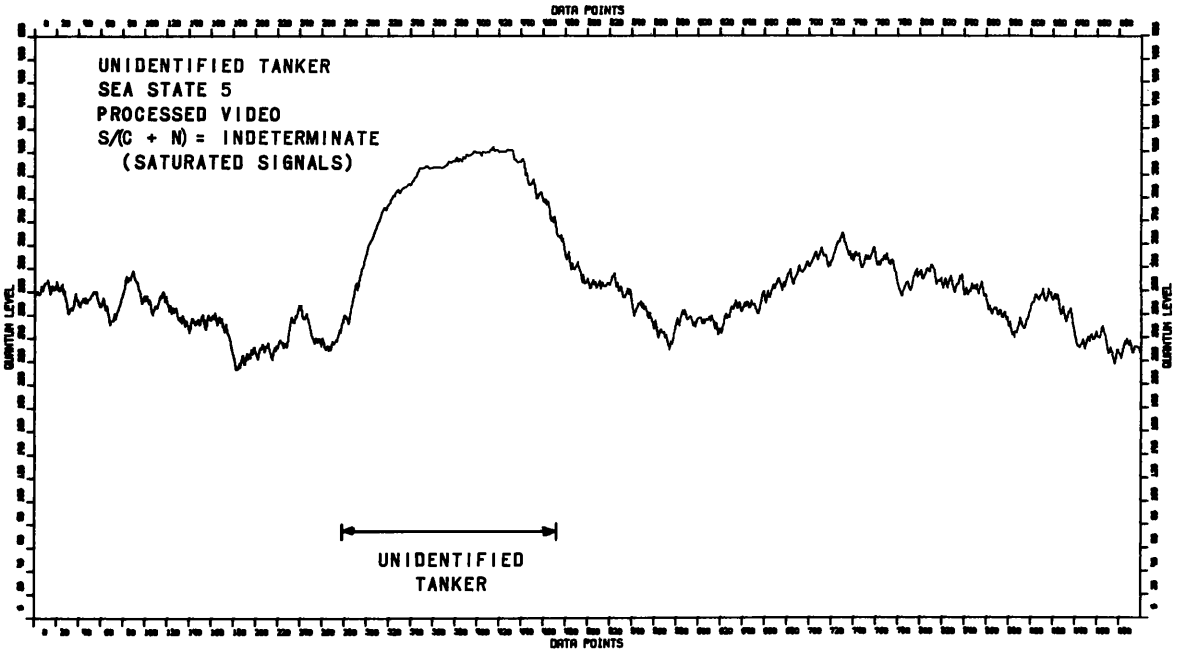

Fig. 13b —Processed radar video for the same data as in Fig. 13a with a feedback factor of 0.969

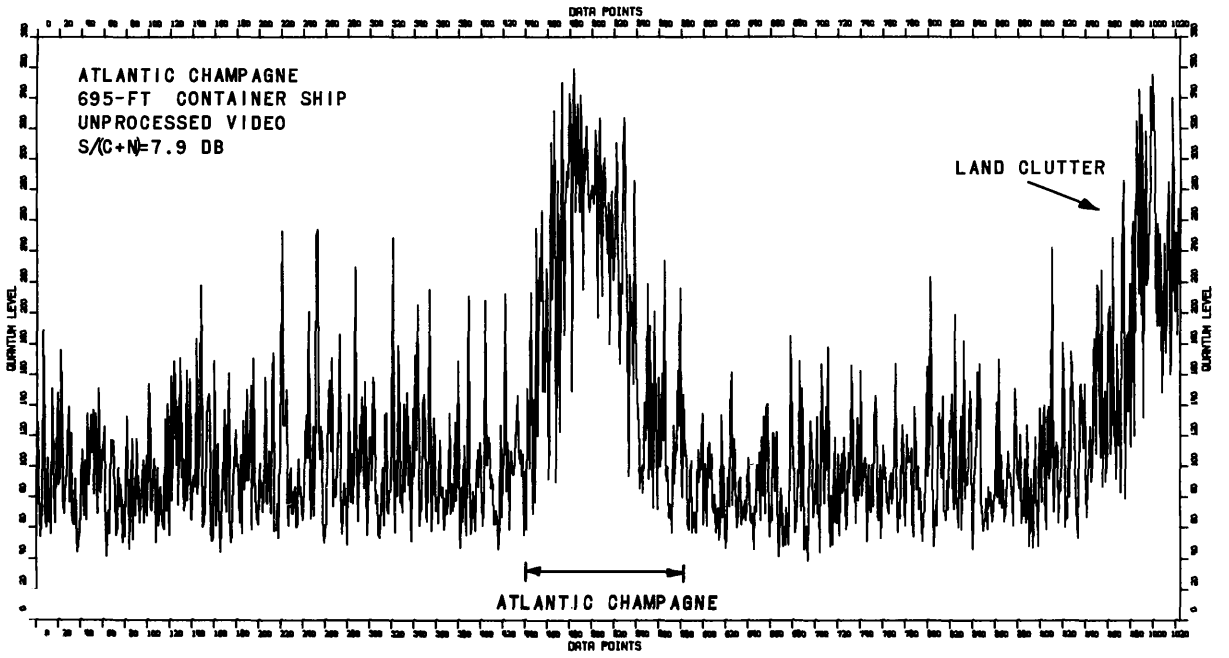

Fig. 14a —Unprocessed radar video for the *Atlantic Champagne*, showing sea clutter and also land clutter

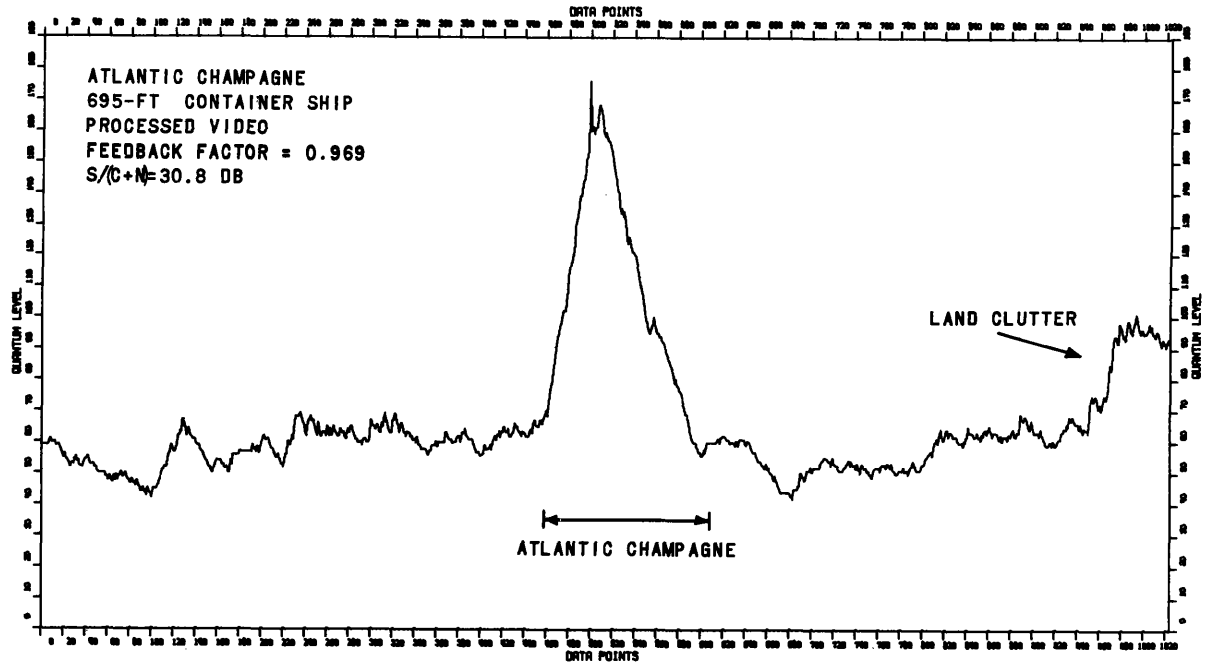

Fig. 14b —Processed radar video for the same data as in Fig. 14a

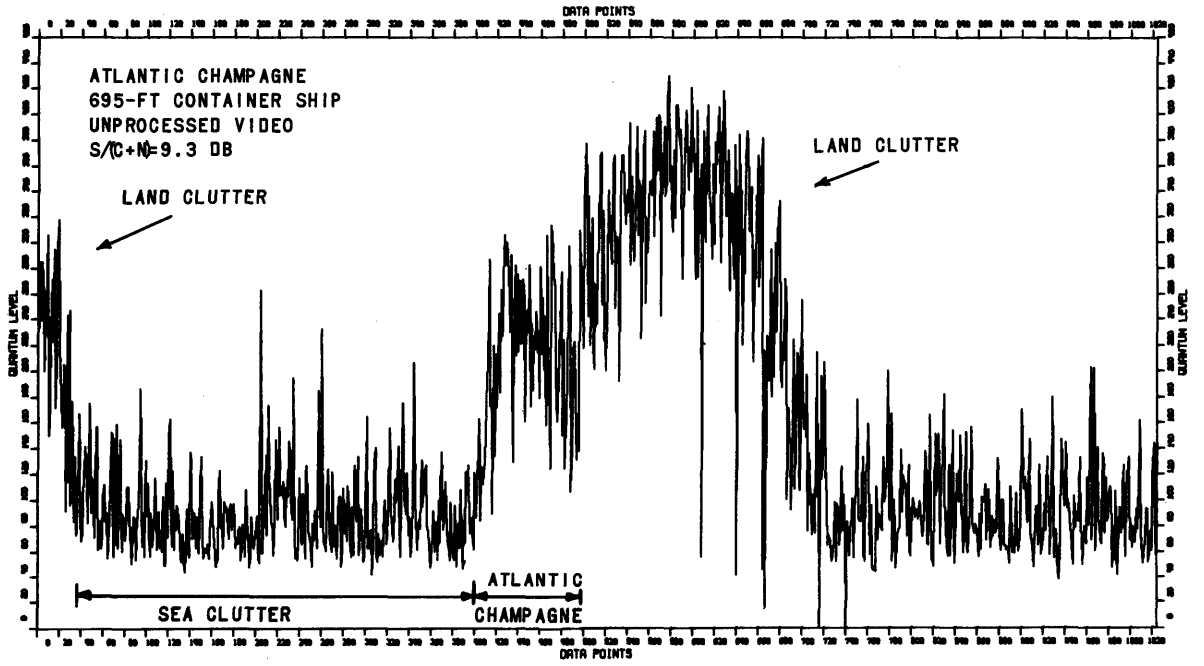

Fig. 15a —Unprocessed radar video data for the *Atlantic Champagne* near land

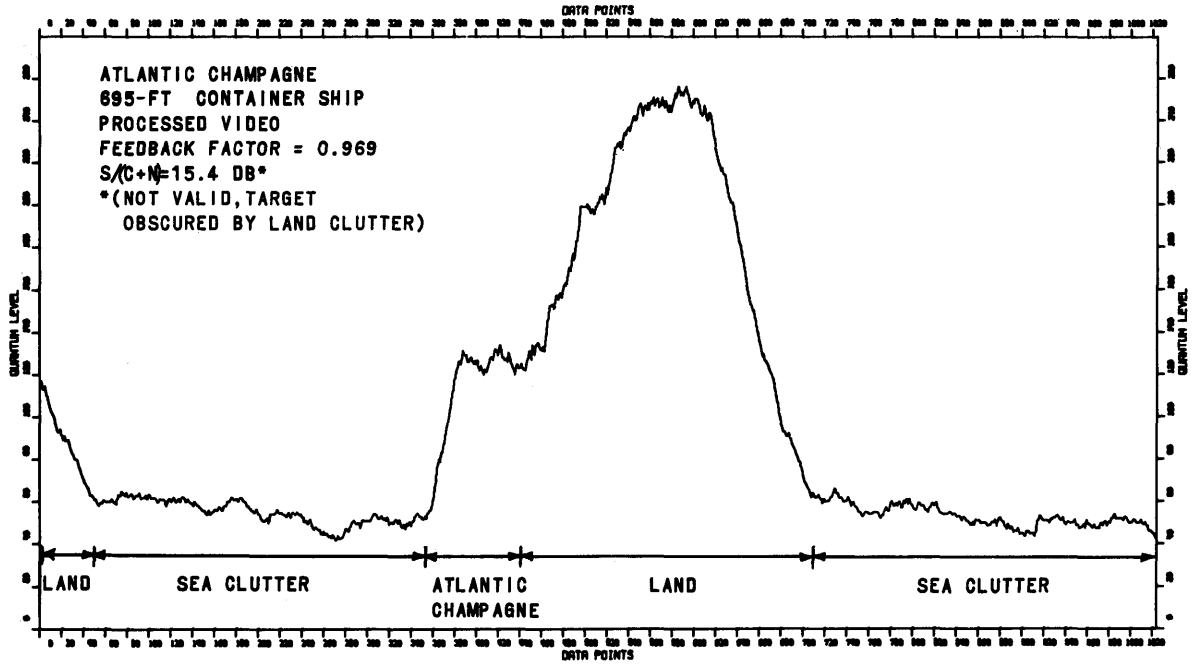

Fig. 15b —Processed radar video for the same data as in Fig. 15a (but offset about 40 pulses to the left)

The favorable geometry for detection close to land in Fig. 16a represents the conditions for the first set of *Atlantic Champagne* data of Figs. 14a and 14b. The unfavorable geometry in Fig. 16b represents the situation for the *Atlantic Champagne* data of Figs. 15a and 15b. In both cases the ship is approximately the same distance offshore; it is the relative position of the radar that makes the geometry either favorable or unfavorable.

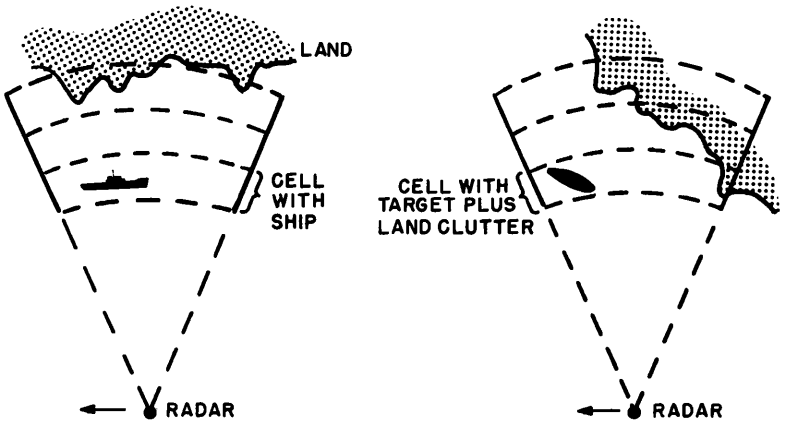

(a) Favorable (b) Unfavorable

Fig. 16 —Geometries favorable and unfavorable

Figures 17a and 17b are plots of data for the tanker *Mobil Aero*. For this data set the targetlike returns, particularly noticeable in the record of processed data (Fig. 17b) near data points 120 and 260, may be from sea clutter or from small trawlers observed to be operating around the track of the *Mobil Aero*. The cause of the minor signal peaks in this instance cannot be resolved positively, because the tracks of the small fishing trawlers were not recorded or confirmed by visual data records.

The remaining sets of unprocessed and processed radar-video data are shown in Figs. 18 through 24.

Table 6 is a tabulation of the $S/(C + N)$ ratios developed for each of the targets selected for analysis in this report. As described earlier, the "experimental" ratios are those derived directly from the experimental data acquired with the airborne test-bed radar.

The second set of $S/(C + N)$ ratios are the result of normalizing the radar transmitter powers to levels that match the particular requirements for scaling to the satellite radar system. The resulting second set of ratios are representative of the ratios to be anticipated for the receiver-video and data-processor outputs of the specified reference satellite radar sensor system. In this second set of ratios, with one exception, the processor output for all targets is greater than the required 16.0 dB. The one exception is a ratio of 15.5 dB obtained for a ship target (the *Owasco*) whose aspect was such that the radar cross section within a 50-foot range resolution cell was 180 square meters (Table 5) rather than the

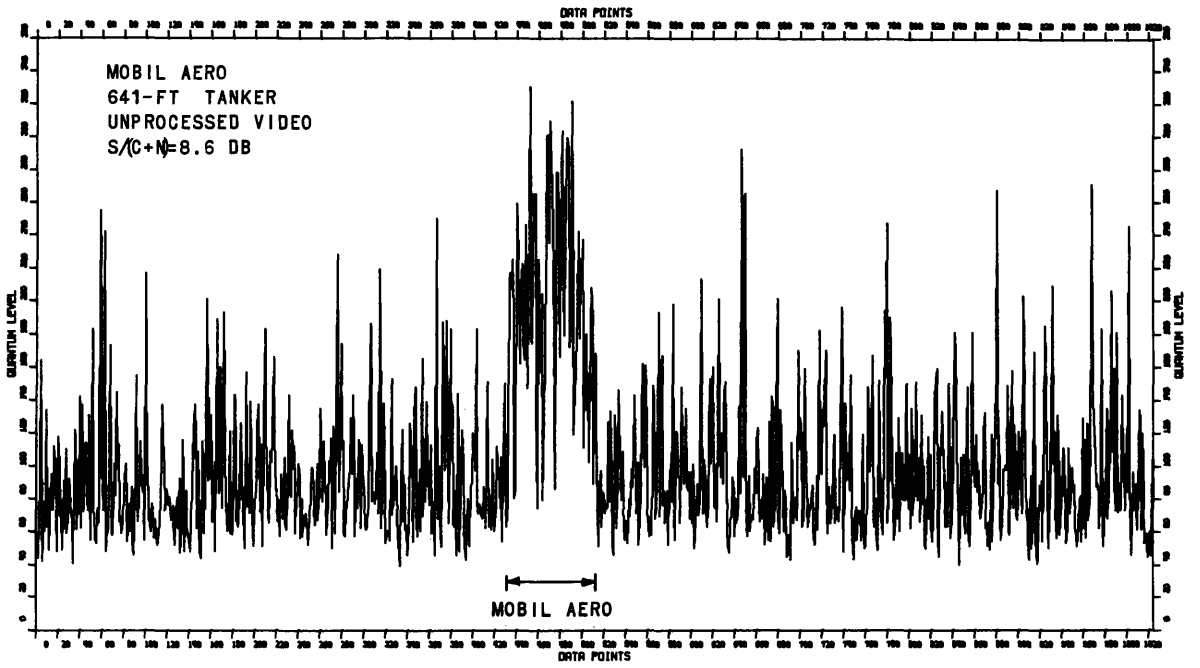

Fig. 17a —Unprocessed radar video data for the oil tanker *Mobil Aero*

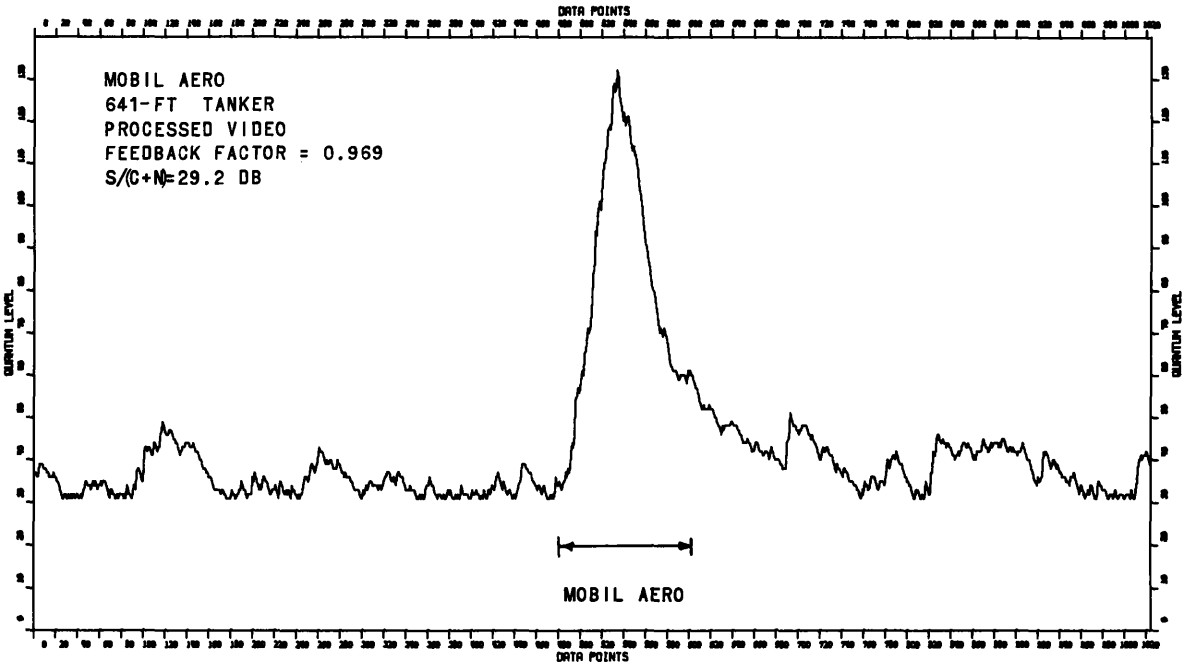

Fig. 17b —Processed radar video for the same data as in Fig. 17a

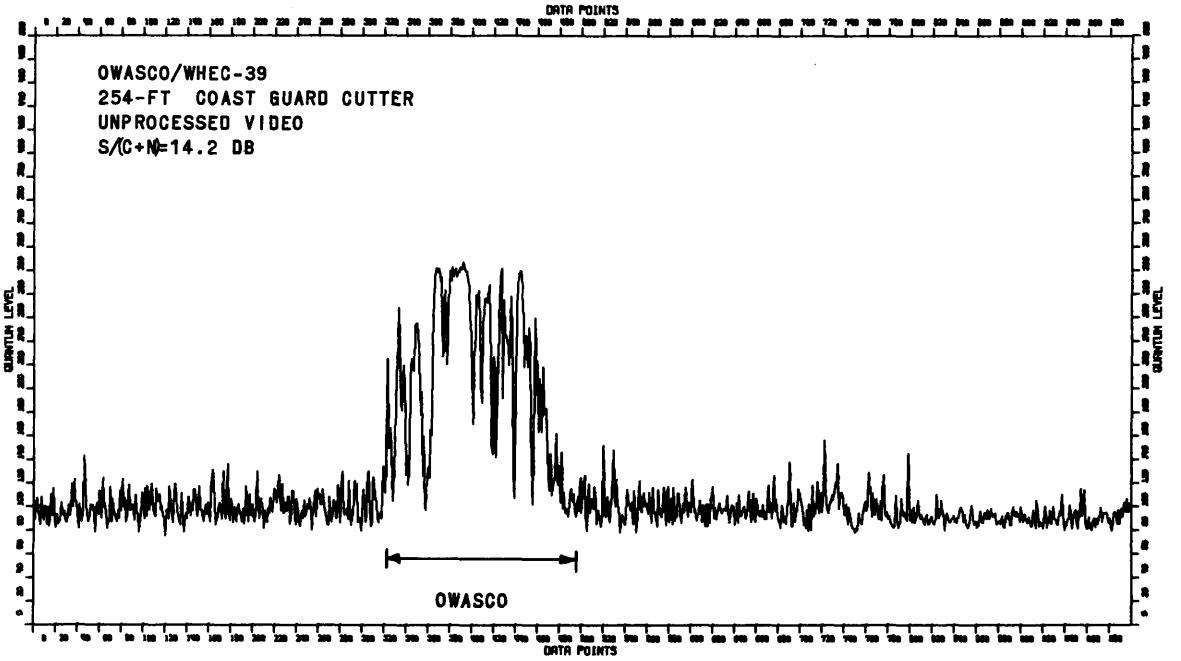

Fig. 18a —Unprocessed radar video data for the U.S. Coast Guard cutter *Owasco*

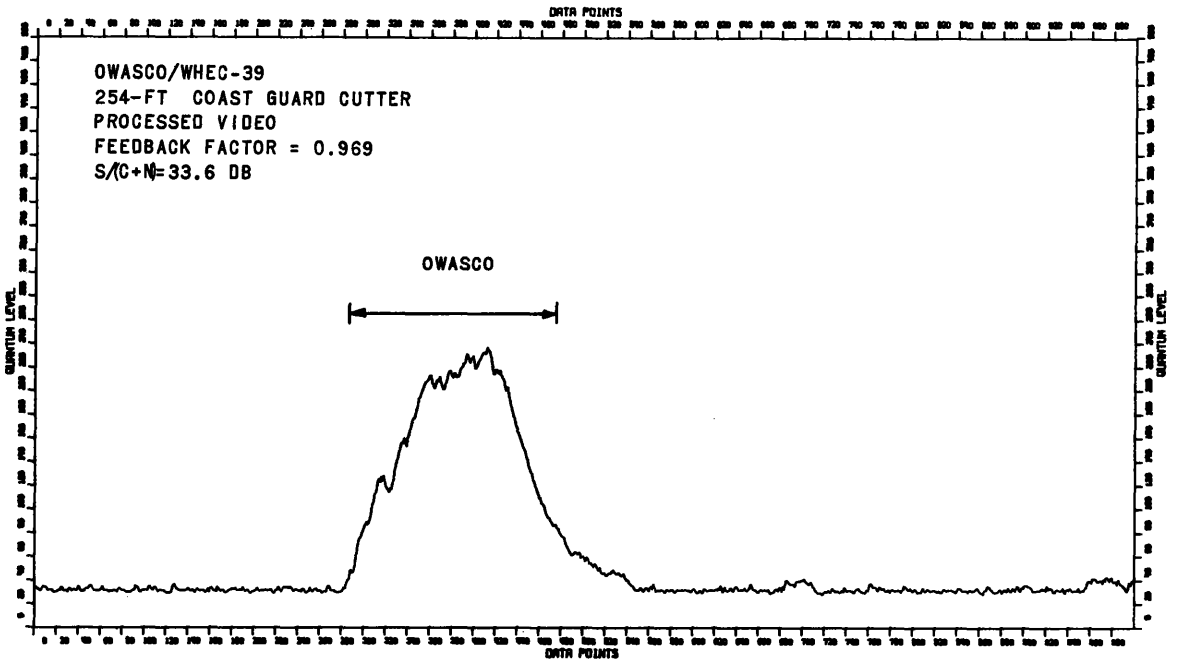

Fig. 18b —Processed radar video data for the same data as in Fig. 18a

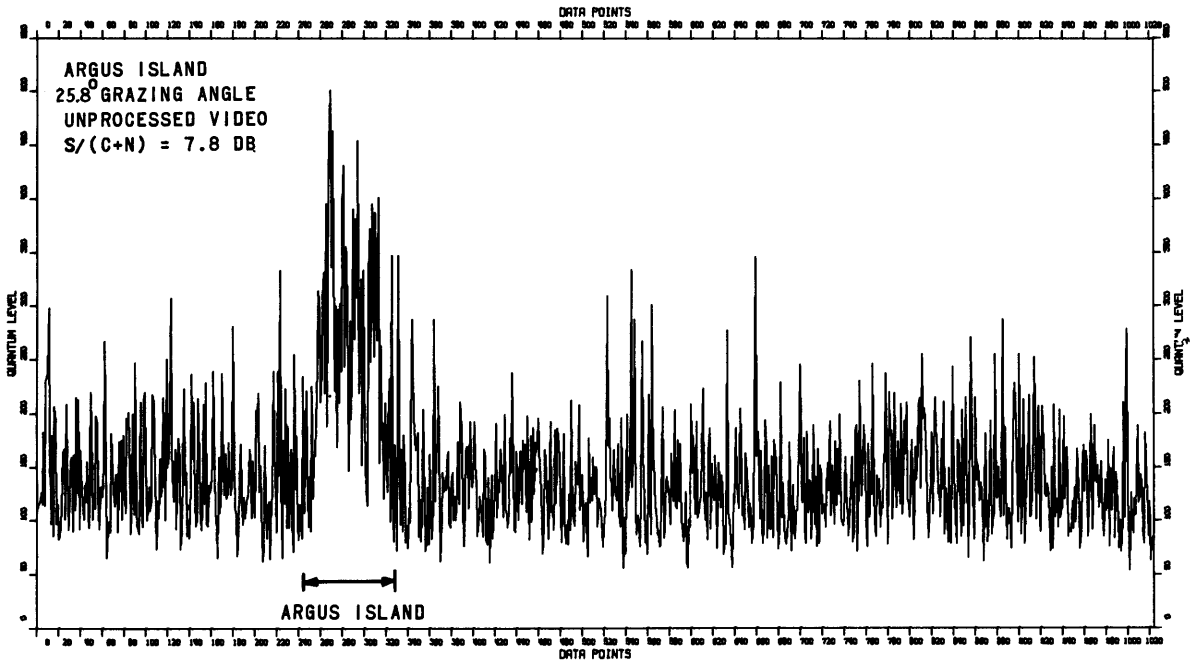

Fig. 19a —Unprocessed radar video data for *Argus Island* acquired at a steep grazing angle (25.8°)

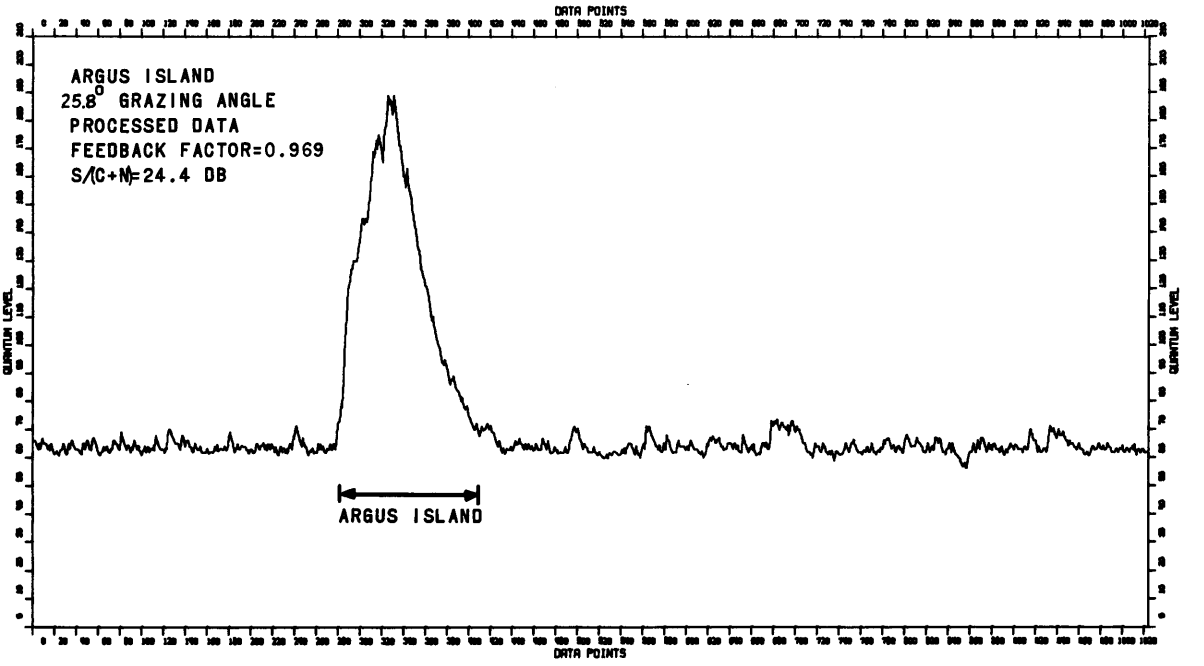

Fig. 19b —Processed radar video for the same data as in Fig. 19a

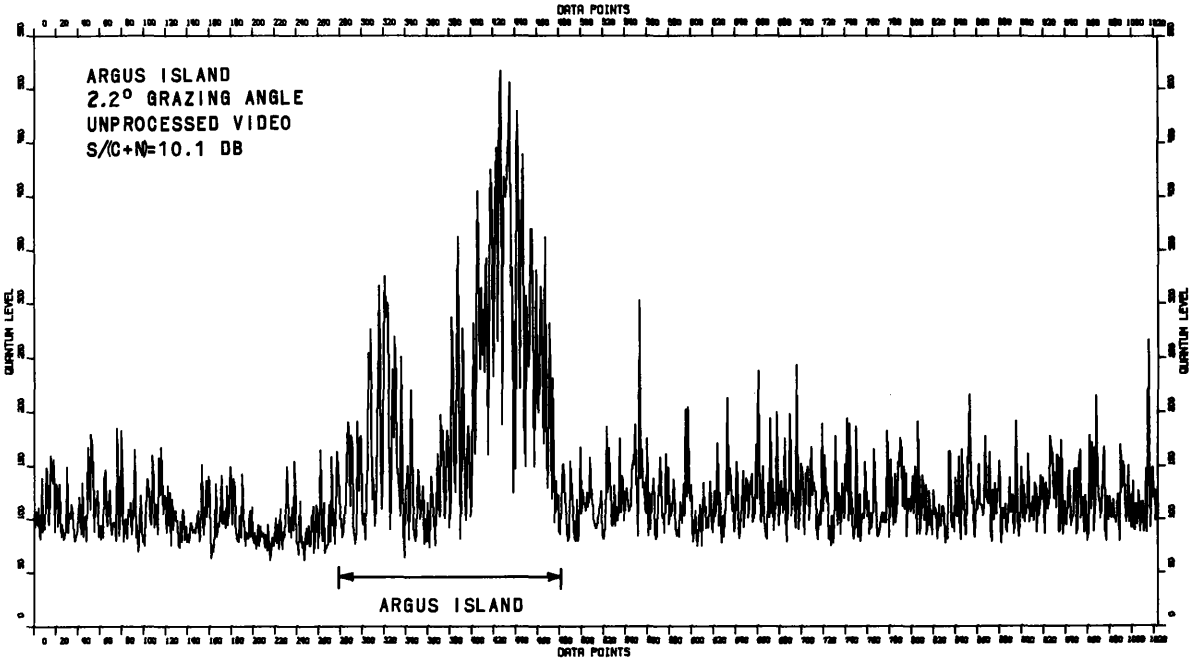

Fig. 20a —Unprocessed radar video data for *Argus Island* acquired at a shallow grazing angle (2.2°)

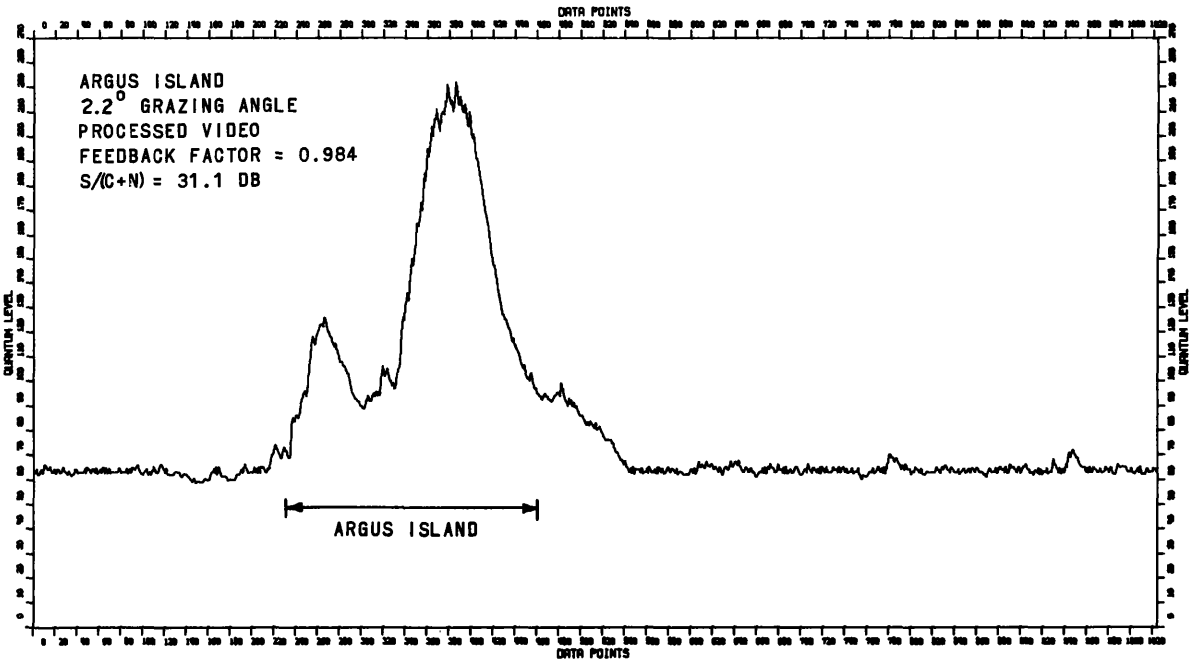

Fig. 20b —Processed radar video data for the same data as in Fig. 20a

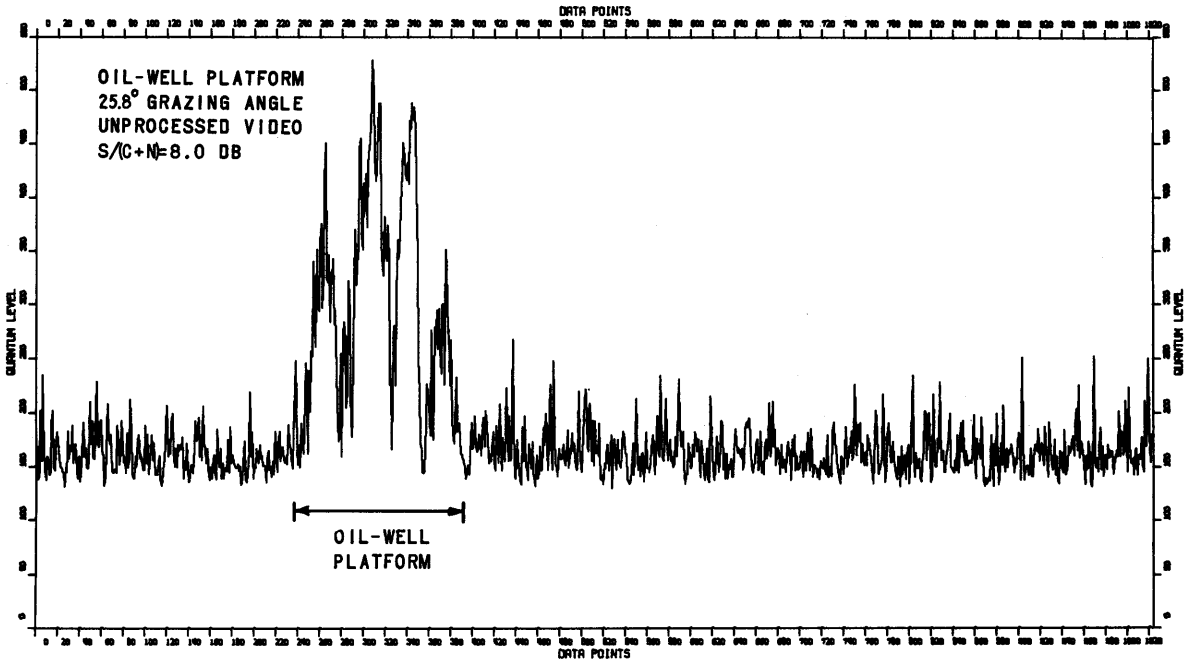

Fig. 21a —Unprocessed radar video for ocean oil-well platforms acquired at a grazing angle of 25.8°

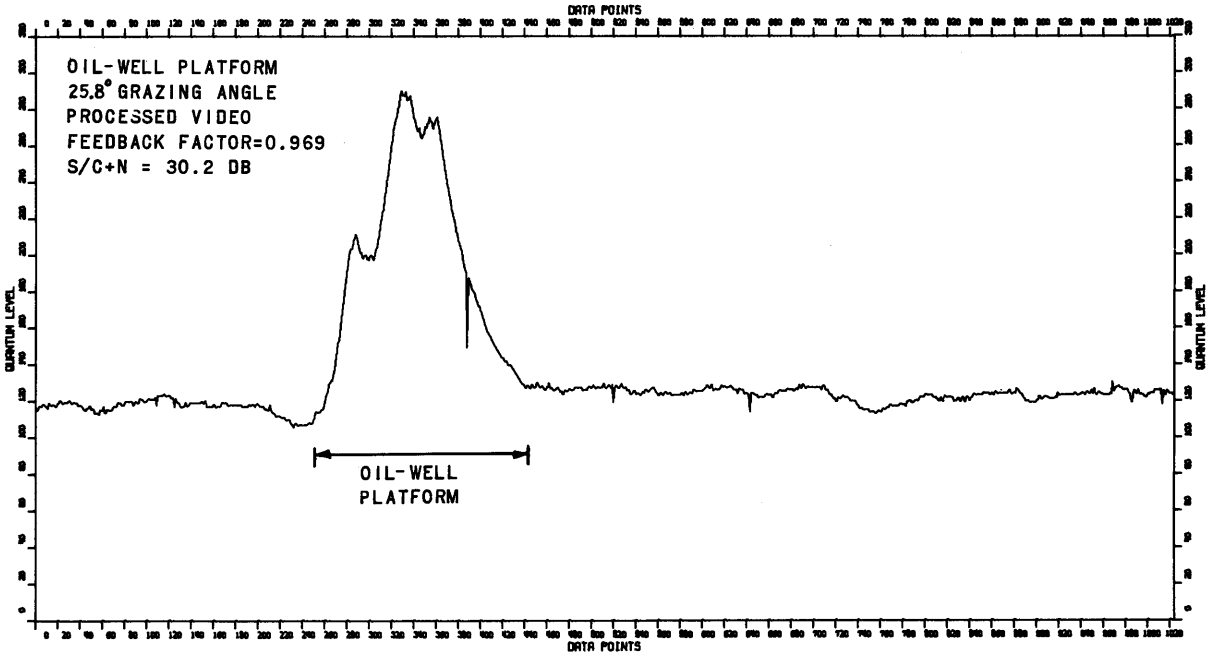

Fig. 21b —Processed radar video for the same data as in Fig. 21a

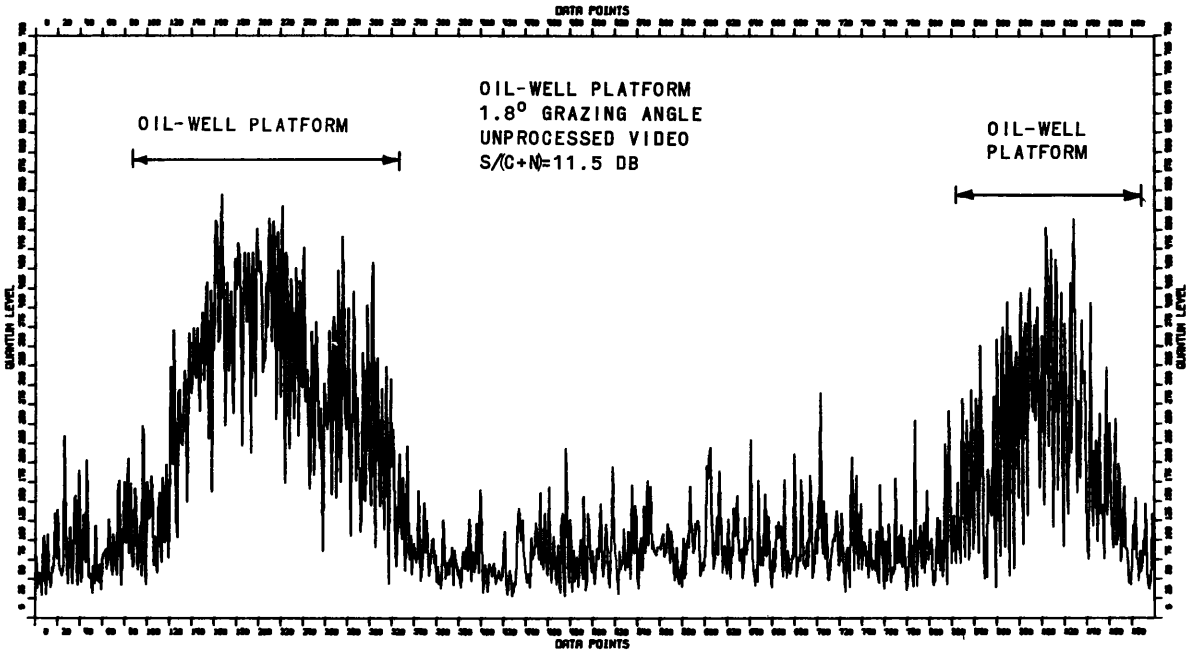

Fig. 22a —Unprocessed radar video for oil wells observed at long range and a shallow grazing angle (1.8°)

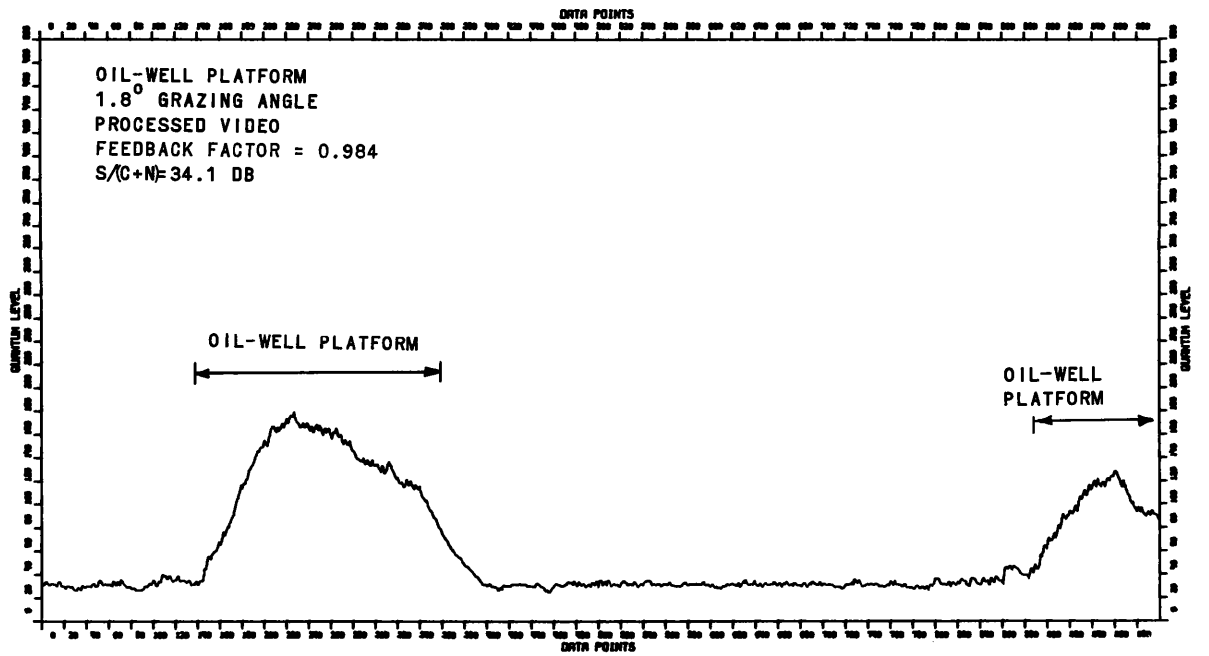

Fig. 22b —Processed radar video for the same data as in Fig. 22a

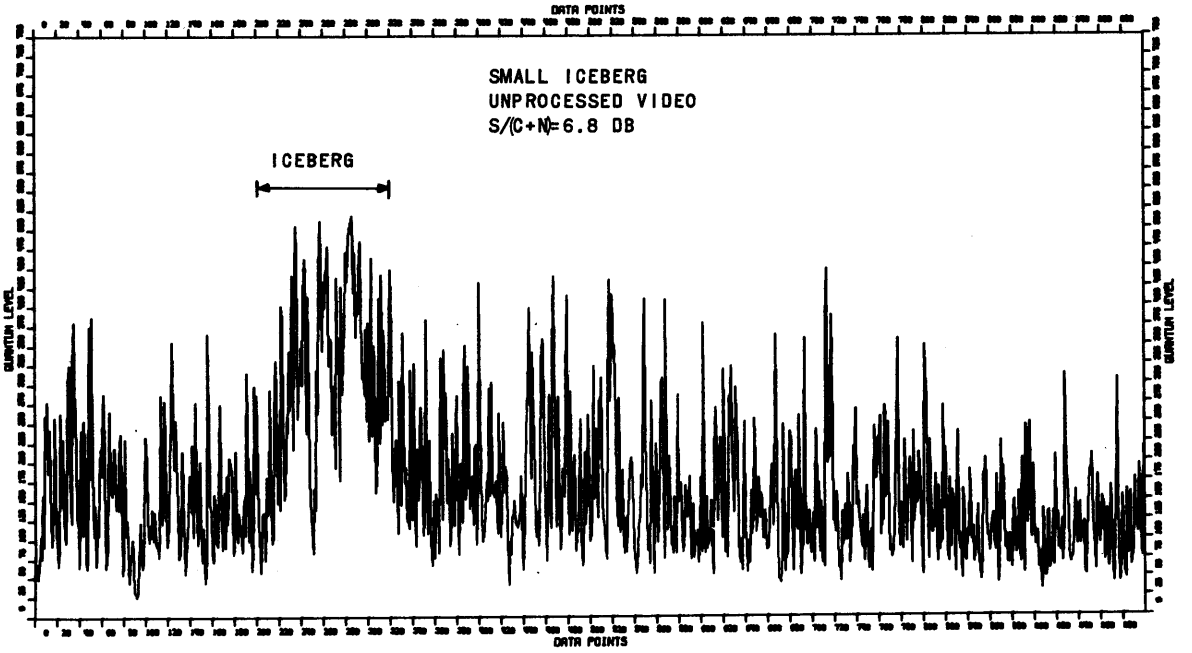

Fig. 23a —Unprocessed radar video data for the small iceberg observed July 26, 1971, 10 to 20 miles off the coast of Newfoundland

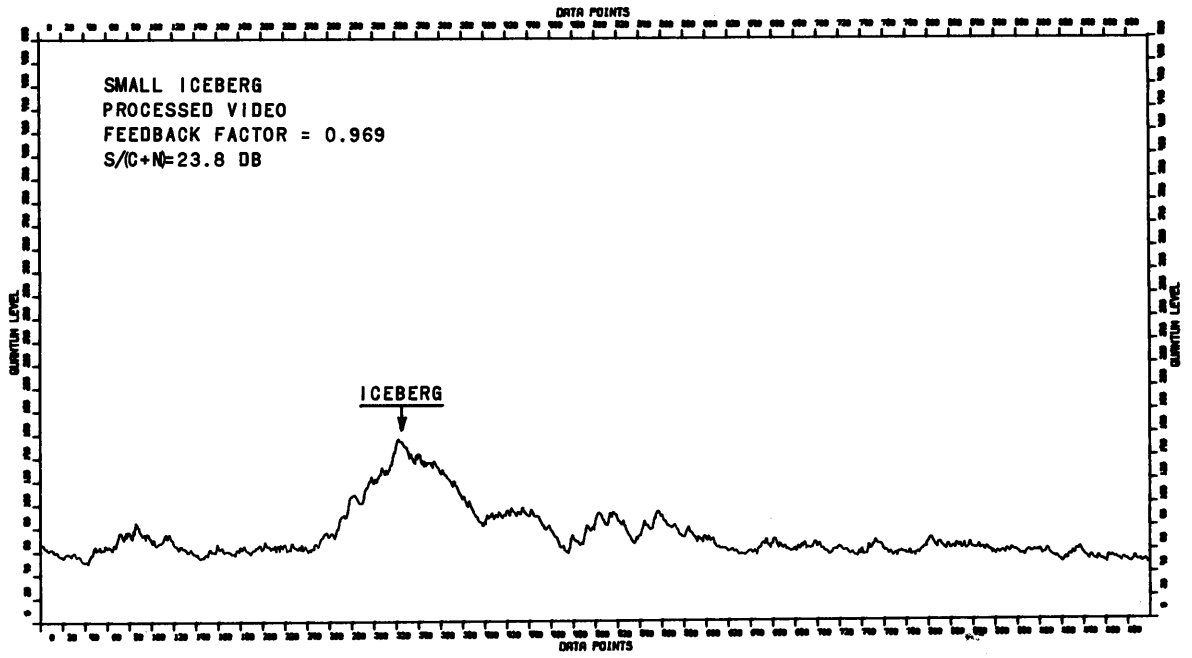

Fig. 23b —Processed radar video for the same data as in Fig. 23a

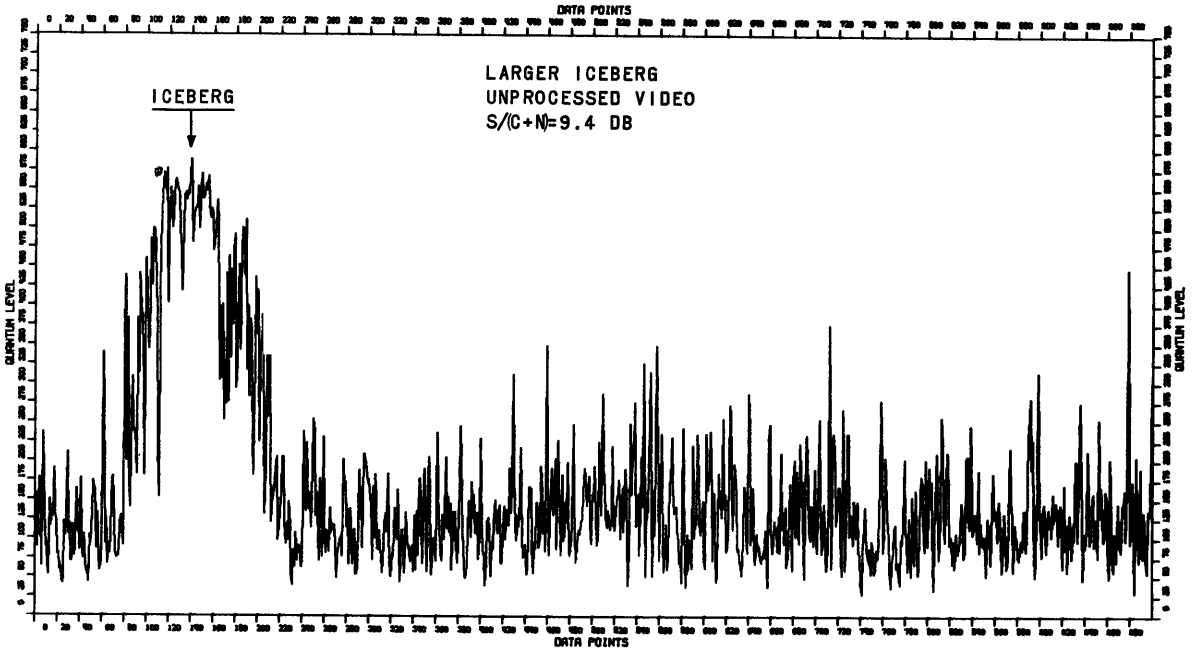

Fig. 24a —Unprocessed radar video for the large iceberg observed July 26, 1971, 10 to 20 miles off the coast of Newfoundland

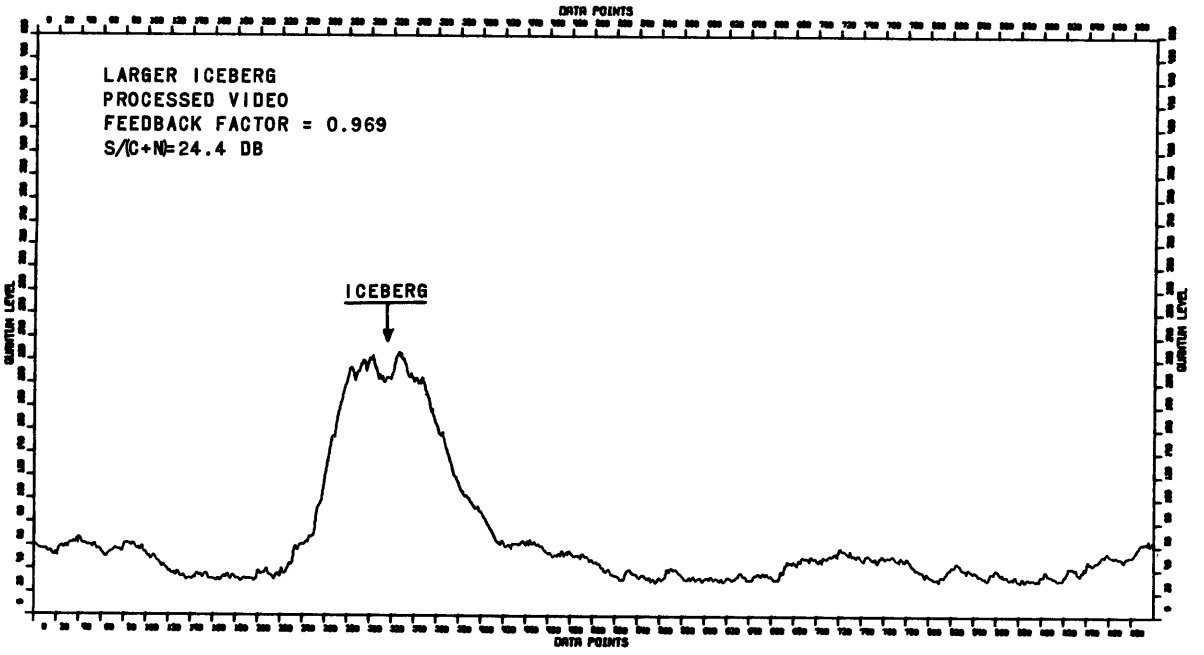

Fig. 24b —Processed radar video for the same data as in Fig. 24a

Table 6
Experimental and Normalized S/(C + N) Ratios for the Targets That Were Analyzed

Target	Sea State	Range (n.mi.)	Grazing Angle (deg)	S/(C + N) Ratio					
				Experimental		Normalized Power		Normalized Power and Cross Section	
				Video	Processed	Video	Processed	Video	Processed
Lady Maria	3	4.5	33.3	10.6	28.5	8.6	26.5	3.6	21.5
	3	6.2	23.5	11.3	32.2	8.1	29.0	2.8	23.9
	3	8.1	17.5	6.2	22.2	1.7	17.7	2.1	18.1
Owasco	1	4.0	37.7	3.5	16.2	2.8	15.5	3.5	16.2
	1	4.9	30.6	6.4	22.0	4.3	19.9	3.4	19.0
	1	6.9	21.9	14.2	33.6	13.9	33.3	2.5	21.9
	1	63.1	1.8	5.7	30.3	9.4	26.6	−1.7	18.8
Texaco Wyoming	5	6.0	24.4	11.2	25.0	9.9	23.7	2.8	16.6
	5	6.6	22.0	14.6	29.8	14.3	29.5	2.6	17.8
	5	7.9	18.1	6.7	25.4	8.8	27.5	2.2	20.9
Mobile Aero	5	6.3	23.1	13.0	35.0	12.1	34.1	2.7	24.7
	5	8.3	17.4	8.6	29.2	11.3	31.9	2.0	22.6
Atlantic Champagne	3	9.9	14.9	7.9	30.8	9.8	32.7	1.8	24.7
Tresfonn	4	61.5	1.8	7.3	35.1	7.1	34.9	−1.7	26.2
Argus Island	3	5.7	25.8	7.8	24.4	12.2	28.8	2.	19.3
	4	58.3	2.2	10.1	31.1	8.9	30.9	−1.7	19.3
Oil wells	3	5.7	25.8	8.0	30.2	12.4	34.7	2.9	25.1
	3	5.7	25.8	13.0	40.8	17.4	45.2	2.9	30.7
	3	58.3	1.8	11.5	34.1	19.8	42.4	−1.8	20.8
Small iceberg	2	4.5	33.3	6.8	23.8	5.6	22.6	3.6	20.6
Large iceberg	2	4.6	32.5	9.4	24.4	9.9	25.9	3.5	19.5

required minimum of 200 square meters. In Fig. 25 the points plotted are for the ship targets listed in Table 6, and the line then is indicative of the processor $S/(C + N)$ output anticipated from the satellite system as a function of the target-ship radar cross section.

The third set of ratios shown in Table 5 result from taking the data of the preceding steps and solving the radar equation for the $S/(C + N)$ ratio, using a normalized radar cross section of 200 square meters in place of the measured experimental radar cross section. The third set of ratios then shows, for both a normalized power level and a normalized radar cross section, the variation in $S/(C + N)$ ratios for a mixture of factors including: a variety of target, target aspects, and sea states; system calibration errors; variations in system status and performance; nonoptimum data processing; and data-reduction timing errors.

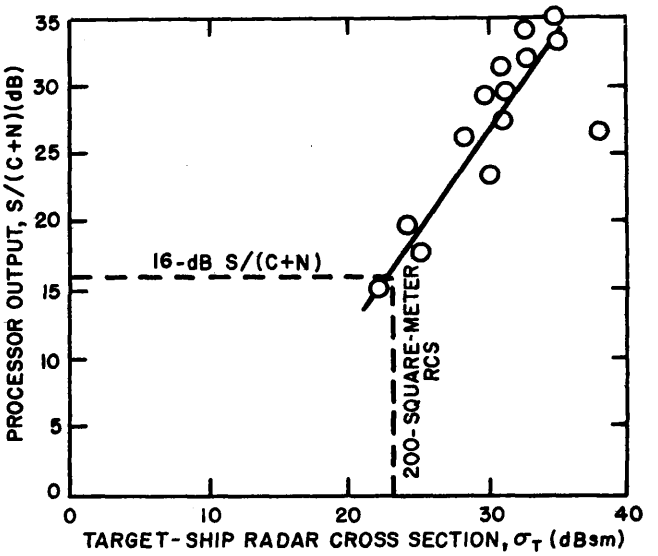

Fig. 25 —Data-processor $S/(C + N)$ output as a function of the radar cross section of the target ship

Experience has indicated that less-than-optimum measures of $S/(C + N)$ ratios should not be attributed to the radar system per se or to the basic video data on tape. In some cases of an initial marginal measure of $S/(C + N)$ ratios, replays of the same set of data with a different integration feedback factor provided significant improvement and an acceptable level of $S/(C + N)$. More frequently, a marginal value of a measured $S/(C + N)$ was determined to result from timing errors in the data-reduction equipment. Short-term and long-term drift problems with the timing and sample-and-hold circuitry were difficult to sense and to control. Replays of the same tape data with changes in the sample-and-hold gate position by 100 to 200 nanoseconds could and did make a considerable difference in the measured signal ratios.

In the third set of $S/(C + N)$ ratios of Table 5 the spread of 16.2 to 30.7 dB for the processor output is of interest in that the lowest value is better than the level originally specified for automatic target detection. Furthermore, experience indicates that given the time to optimize the data processor and optimally set the sample-and-hold gate, the same data set that yielded a $S/(C + N)$ ratio of 16.2 dB can reasonably be expected to result in a better ratio. The 30.7-dB value, the highest in this set of ratios, is not for a ship target but oil-well platforms. Using the experimental data as a guide, the expected processor output level for a ship target with a 200-square-meter radar cross section is indicated to be 17.5 dB.

Autocorrelation Coefficients

The correlation between successive signal returns from a target is sometimes measured by the autocorrelation coefficient $\gamma_{xx}(k)$. In the notation of Jenkins and Watts (13), the discrete-time autocovariance estimates for observations of pulses $x_1, x_2, \ldots, x_n$ from a discrete-time series of pulses is

$$C_{xx}(k) = \frac{1}{N} \sum_{t=1}^{N-k} (x_t - \bar{x})\,(x_{t+k} - \bar{x}),\ k = 0, 1, \ldots, N-1,$$

where (2)

$$\bar{x} = \frac{1}{N} \sum_{t=1}^{N} x_t.$$

Normalizing the discrete-time autocovariance estimates with the zero-lag autocovariance estimate $C_{xx}(0)$ yields the autocorrelation coefficient:

$$\gamma_{xx}(k) = \frac{C_{xx}(k)}{C_{xx}(0)}.$$

In Figs. 26 through 29 plots of autocorrelation coefficients vs lags of 0 to 100 are presented for a number of specific conditions. In Fig. 26 the plot is for noise generated by a computer random-number program. In Fig. 27 the autocorrelation coefficients for

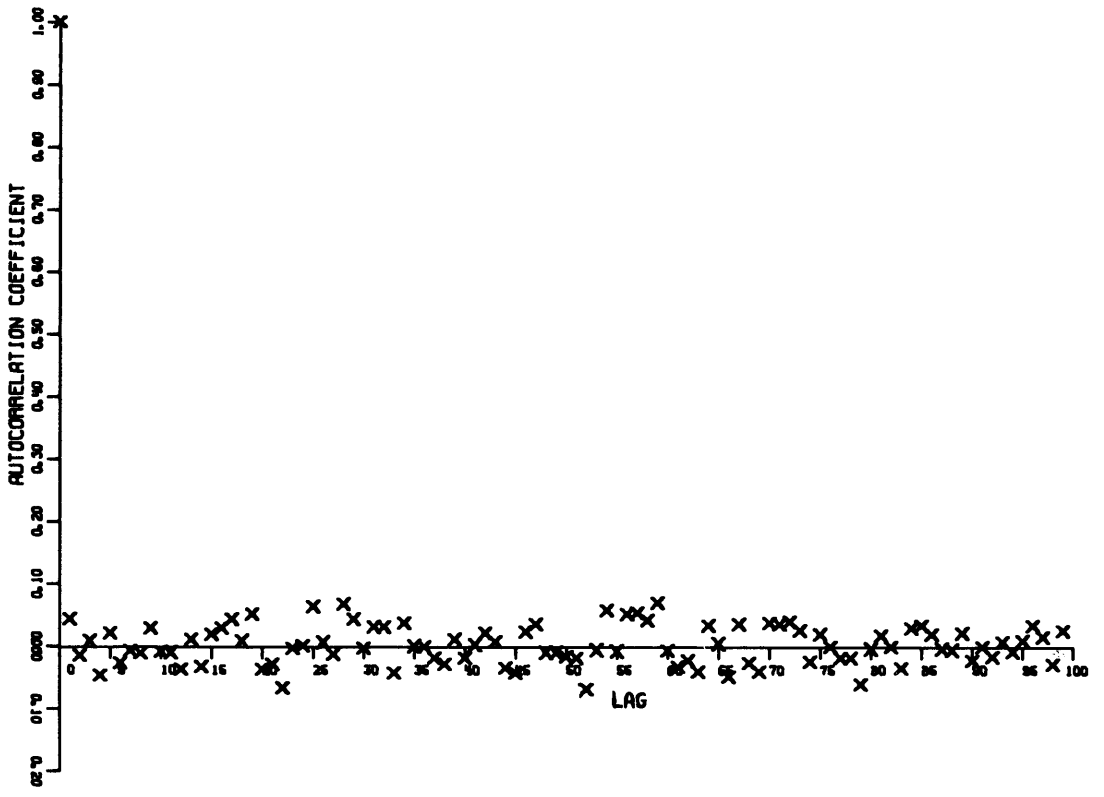

Fig. 26 (Unclassified)—Autocorrelation coefficients for a noise sample derived from a computer random-number generator, weighted for a normal distribution of noise

the system noise of the test-bed radar are plotted as a function of the lag window. Figures 26 and 27 and Fig. 28 serve as a reference and show that for a lag of 1 or more, the autocorrelation coefficient is low for a noiselike signal.

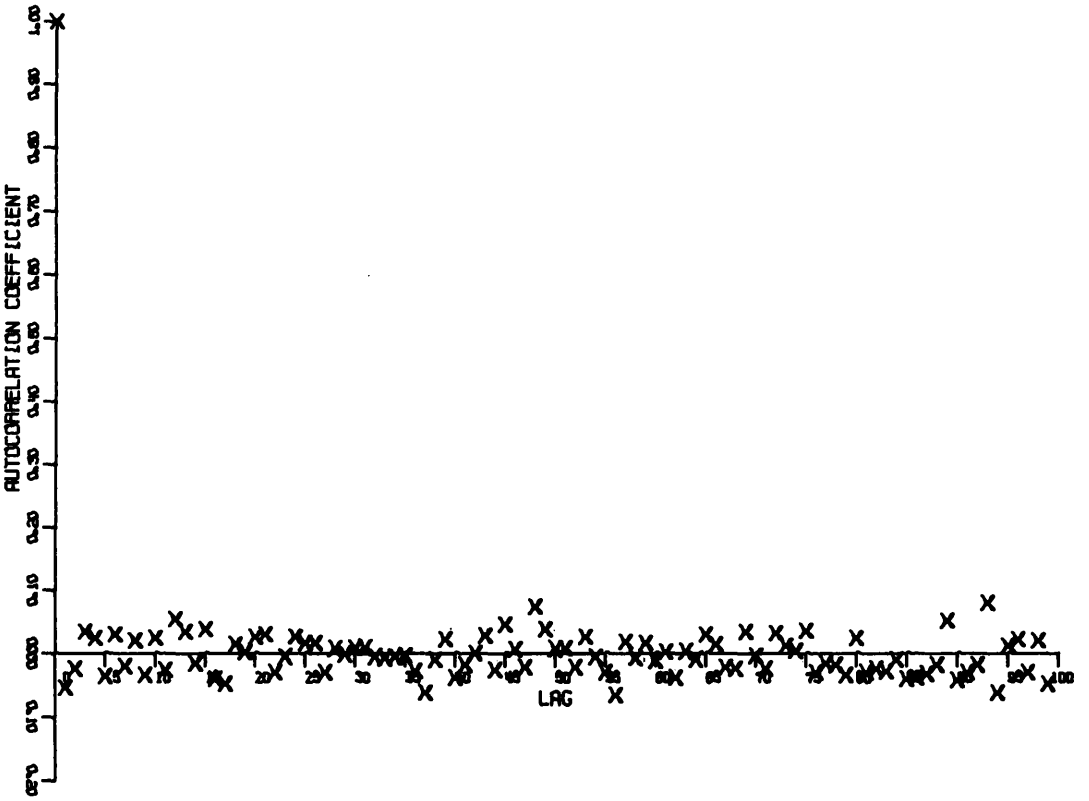

Fig. 27 (Unclassified)—Autocorrelation coefficients for the system noise in the receiving system of the test-bed radar

Figures 28a and 28b are plots of $\gamma_{xx}(r)$ for sea clutter, with the first based on data acquired with a nonscanning antenna and the second based on the same antenna and clutter environment but with the antenna scanning. In both cases, with a lag factor of 1 the autocorrelation coefficient is low, and the implication is that the clutter is essentially decorrelated. The coefficient at a lag of 1 for the scanning antenna is lower than for the nonscanning antenna; in fact for the scanning antenna the complete plot from $k = 0$ to 100 is much like the plots of γ_{kk} for noise in Figs. 26 and 27.

Figure 29a shows the result of determining the γ_{xx} for a clutter sample contaminated with data for a ship target (the *Owasco*). Accounting for the antenna rotation rate, the azimuth beam width, the radar pulse repetition rate, and a quasi-discrete target, approximately 86 pulses illuminated the ship per antenna scan. The contamination of the clutter by about 86 successive pulses out of a total data sample of 1024 is reflected by the high and positive autocorrelation coefficient which is maintained out to a lag factor of 85. In Fig. 29b autocorrelation data are presented for the *Owasco* which were acquired with a

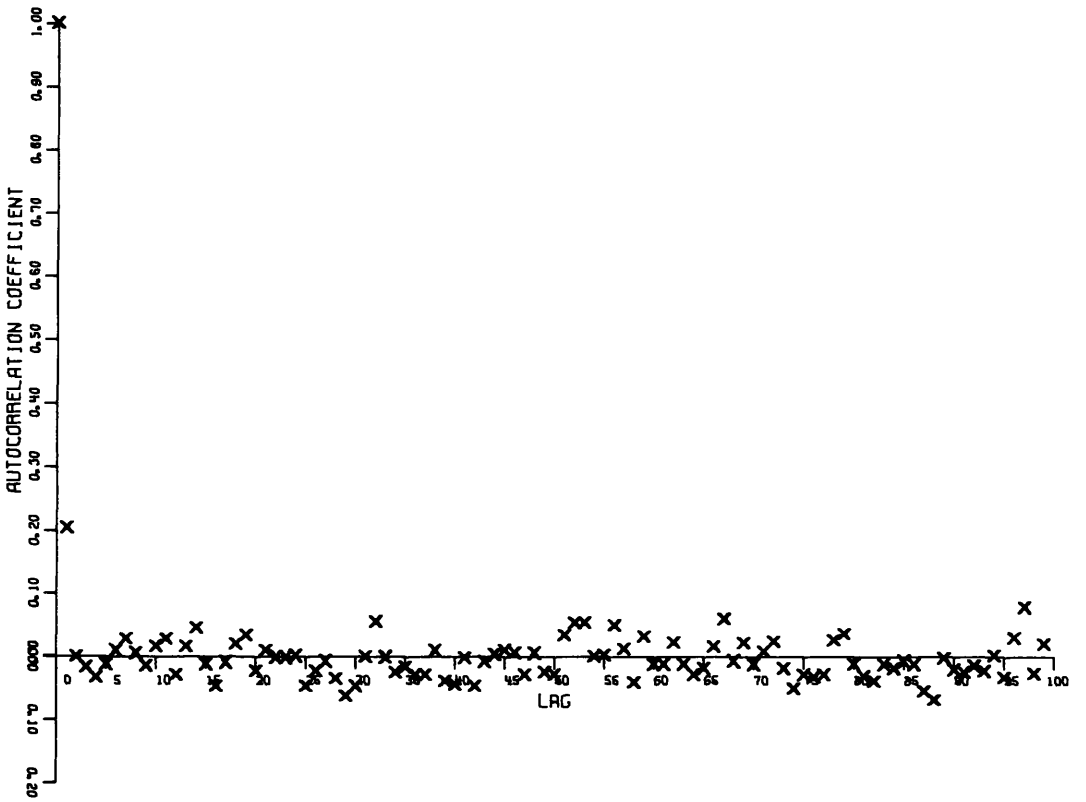

Fig. 28a (Unclassified)—Autocorrelation coefficients for sea clutter based on data acquired with a nonscanning antenna

fixed antenna. The fixed antenna provided a long sequence of successive pulse returns for the duration of the time that the target was within the 3-dB antenna azimuth beamwidth. The plot shows that the *Owasco* was a highly correlated target.

Radar Cross Sections

The radar cross sections of various targets (Table 5) calculated with test-bed-radar data serve several functions: comparison with cross sections from other radar systems, a check on the status and performance of the radar system, and information relative to the azimuth and aspect sensitivity of a target.

System calibration and in-flight calibration procedures have been mentioned earlier. One known weakness in the airborne data acquisition has been the inability because of time and aircraft availability to perform on-aircraft, in-flight measurements of the antenna patterns for the two antennas. Although such in-flight measurements are lacking, the relative detection capability and the integration gain achieved with the digital data processor, can still be demonstrated.

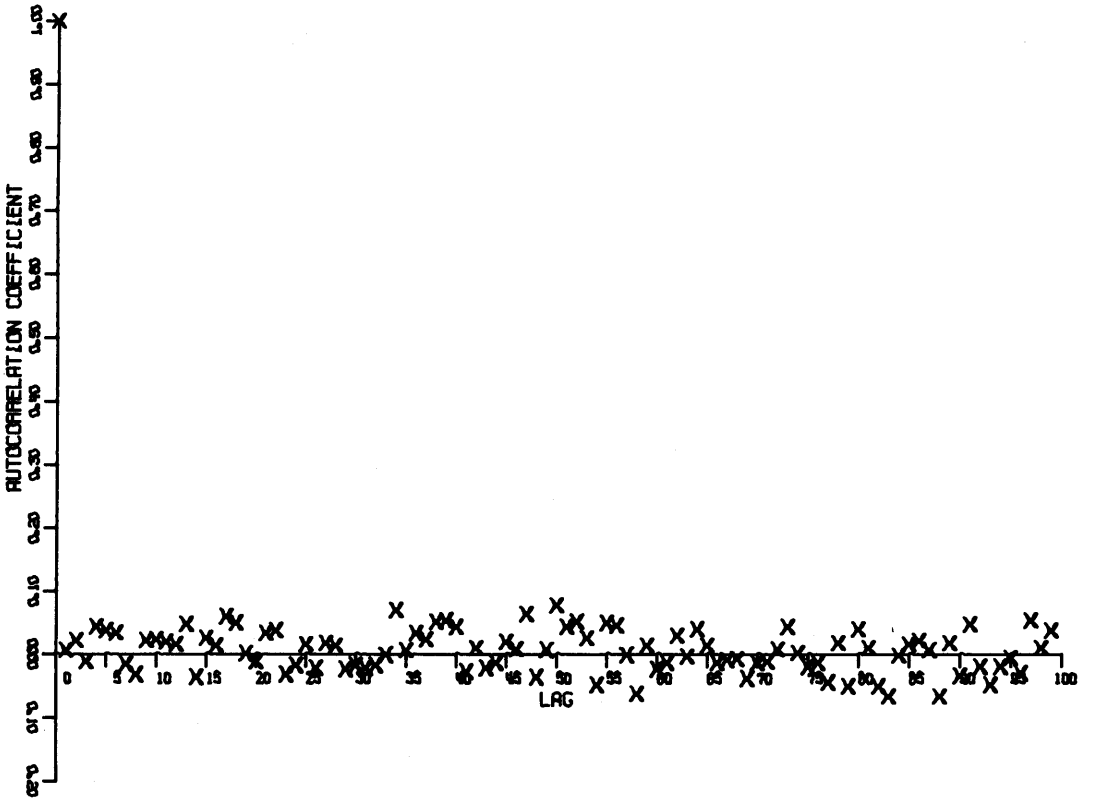

Fig. 28b (Unclassified)—Autocorrelation coefficients for sea clutter based on data acquired with a scanning antenna

The uncertainty in gain does raise questions regarding the significance and the validity of the radar cross sections derived from the test-bed-radar data. Gain and antenna-pattern measurements for each antenna were made on an antenna range and in anechoic chambers. The values of gains from those measurements were the values used in Eq. (1) for calculating radar cross sections. From experience with similar aircraft-mounted antennas in EC-121 aircraft for which on-aircraft pattern measurements were made, less beam depression and deformation as a consequence of being mounted on the aircraft would be expected for the small antenna looking down at a steep (28°) angle from the aircraft local horizontal than would be expected for the larger antenna whose mechanical boresight is almost on the horizon.

Lacking the on-aircraft patterns, the validity of the cross-section measurements is enhanced by a comparison of values derived for the test-bed radar with those of a highly calibrated radar. Reference 14 documents the results of radar-cross-section measurements of ships with a calibrated four-frequency airborne radar system.

In Fig. 30 L-band radar-cross-section data for horizontal polarization on transmission and reception has been extracted from Ref. 14 to develop the six vertical bars and dashed curve. Each bar represents the variation in radar cross section for a specific ship over an

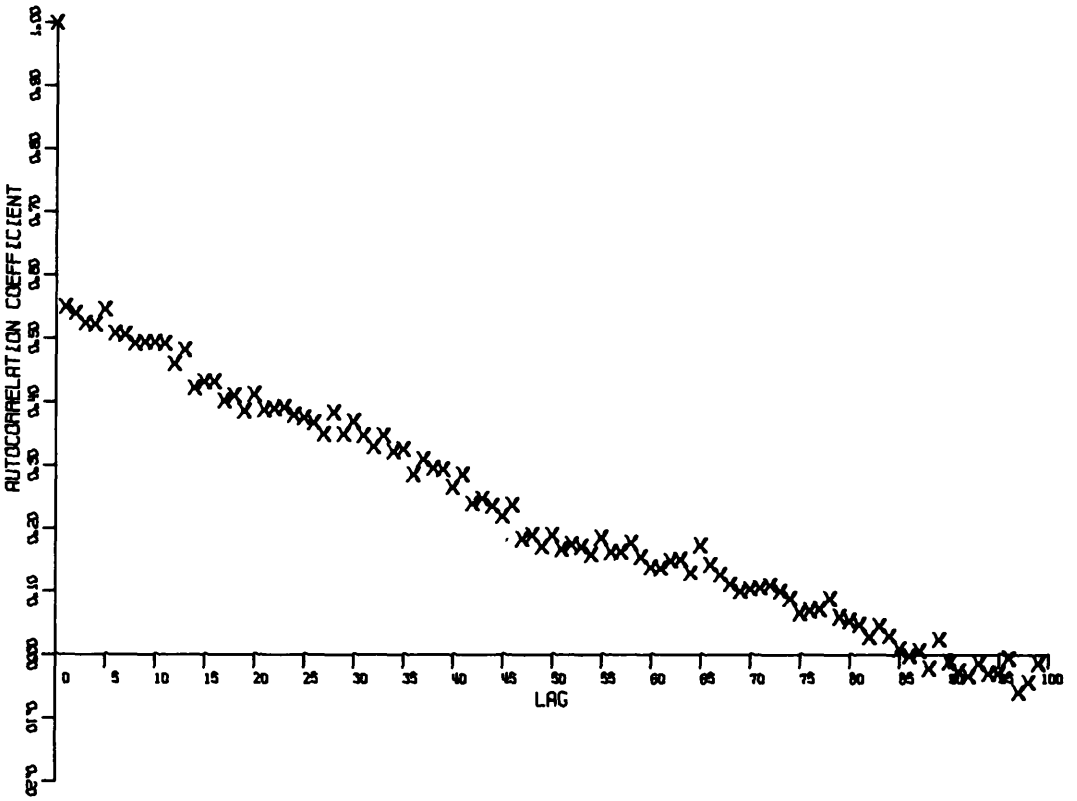

Fig. 29a —Autocorrelation coefficients for the *Owasco* based on scanning-antenna data

aspect variation of ±10° relative to the beam (90°) aspect. The ±10° variation is selected to provide for an averaging around the beam and to allow for the inexactness of determining the aspect of a ship target during data runs. The dashed curve is then a representative of the mean radar cross section for a nominal beam aspect related to length of the target.

The circular symbol marks a cross section for the *Lady Maria* derived from test-bed-radar data. The two triangular symbols mark similarly derived cross sections from two different sets of data for the *Owasco*. Comparing the test-bed-radar data points with the L-band values derived from Ref. 14 shows that the test-bed values are well within the bounds of the reference data and by chance lie almost on the dashed curve representing the anticipated mean radar cross section for the nominal 90° ship target aspect.

Only two test-bed-radar ship targets are represented in the comparison of data in Fig. 30 because of the 50-foot range of the resolution cell. A consequence of the 50-foot cell dimension is that few ship targets ever lie within the bounds of a single cell. The *Lady Maria* with a 28-foot beam and the *Owasco* with a 43-foot beam are the only targets analyzed that were capable of being totally included within a resolution cell. Except for the 90° aspect of the *Lady Maria* and of the *Owasco*, none of the other

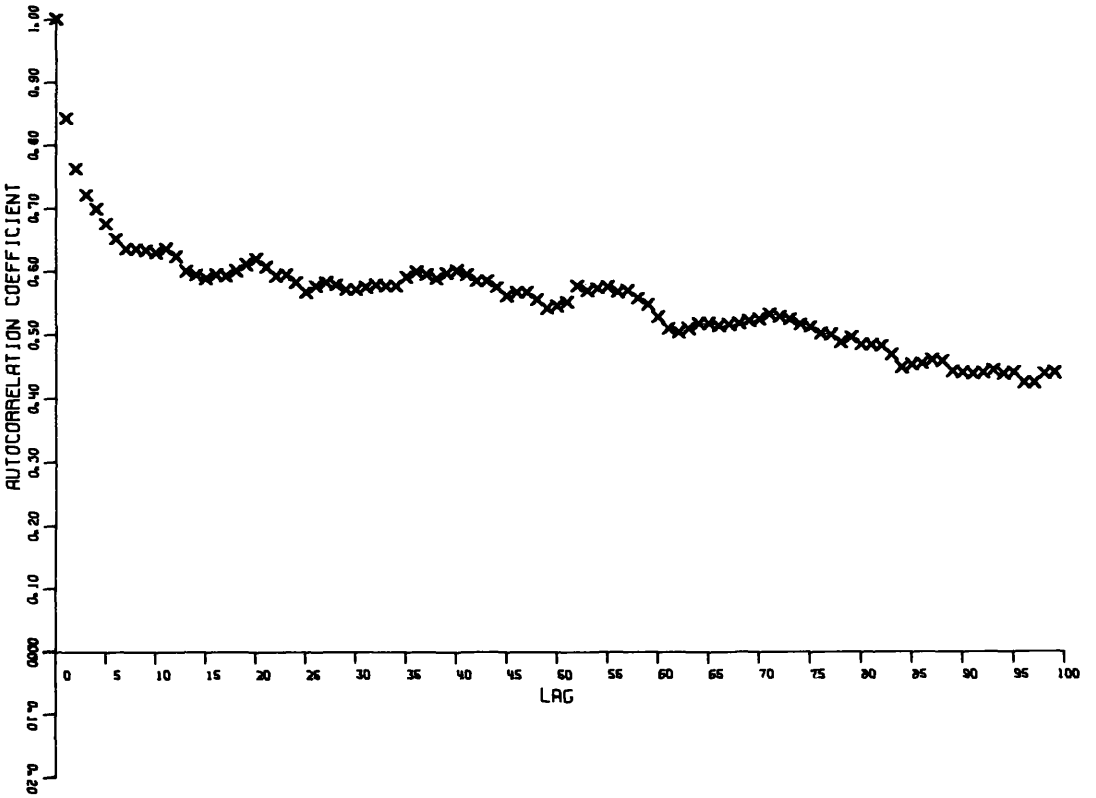

Fig. 29b —Autocorrelation coefficients for the *Owasco* based on nonscanning-antenna data

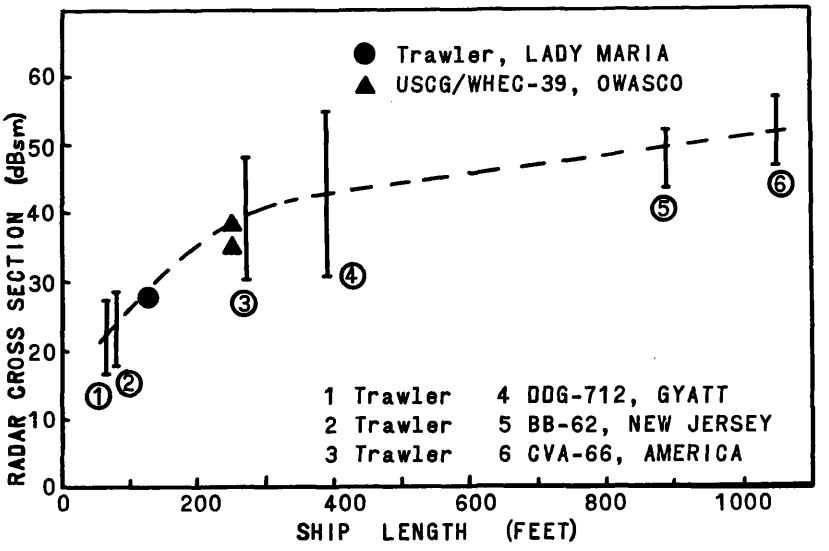

Fig. 30 —Data from Ref. 14 (six data bars for the radar-cross-section variation over ±10° of the beam aspect) and test-bed-radar data (three data points) showing the relationship between ship length and radar cross section for the nominal beam aspect of the target

aspects may be compared directly with the data in Ref. 14 (Fig. 31), nor may any of the other ship data obtained with the test-bed radar be compared as directly, because (Table 3) the targets cannot be totally included within a single resolution cell.

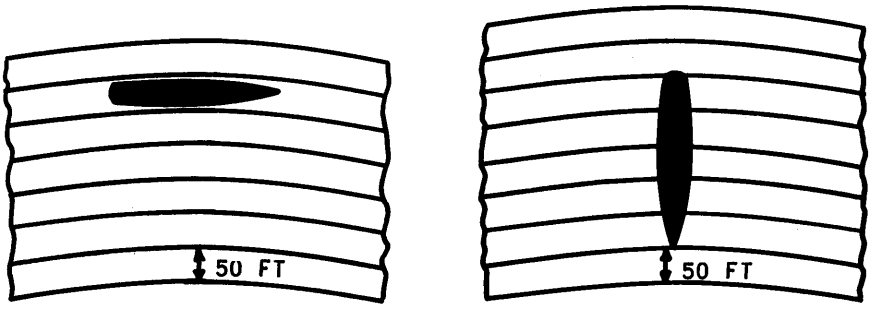

(a) Beam aspect (b) Bow aspect

Fig. 31 —Necessity of a beam aspect for the *Owasco* radar cross section to be totally included within a single resolution cell

The total radar cross section of a target that exists in several adjoining cells can be complex to assess. A simplistic approach that will be examined briefly is to assume a high degree of homogeneity for a target. The *Owasco* when viewed at a bow aspect yielded a radar cross section of 180 square meters. When viewed at a bow aspect (Fig. 31b), the 254-foot *Owasco* physically extended over five successive resolution cells. Assuming a homogeneity of radar cross section from one cell to the next, the radar cross section for the bow aspect of the *Owasco* would be 5 times the single cell value, or 900 square meters. Figure 32 (again extracting data from Ref. 14) shows the relationship between radar cross sections of ships and their beam dimensions. The circular symbols are L-band cross sections for different ships from Ref. 14 obtained using horizontal polarization on transmission and reception. The triangular symbol is the total bow-aspect cross section for the *Owasco* arrived at through the assumption of target homogeneity. Using this approach, the test-bed-radar data are in excellent agreement with the data of Ref. 14.

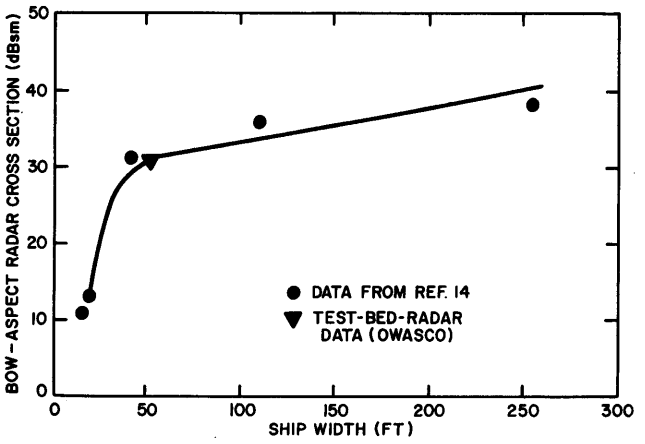

Fig. 32 —Data from Ref. 14 and obtained with the test-bed radar showing BOW aspect radar cross sections of ships at bow aspect versus ship width

Oil Wells and Icebergs

Ocean oil-well platforms and icebergs constitute targets which must be accounted for and hopefully discriminated from ship targets. Included in the data acquired during flight operations were a number of runs in geographic areas where some of these unique targets may be encountered.

The ocean oil-well platforms off the Louisiana coast start at the shoreline and are encountered to points 40 miles offshore. Figure 33 shows the distribution of wells in a 10-by-35-mile area in which data were acquired. In the 350-square-mile region there were 30 major platforms, making for a density of approximately 9 per 100 square miles. Radar cross secitons have been developed for two of the wells: 1270 and 7220 square meters. Though not analyzed, the observed strength of returns from most wells in the operating area is such that radar cross sections are estimated to be in excess of 1000 square meters for each of the observed oil-well platforms.

Icebergs also constitute unique geographically located ocean targets. The season geographical extent of icebergs is generally predictable (15). Of interest are the radar cross sections and population densities of icebergs that would be detected by an ocean-surveillance radar. The data acquired do not have statistical significance, but they are of value as a data sample. Two of the icebergs specifically analyzed are shown in Fig. 7; the nearer one in the photograph had a calculated cross section of 320 square meters, and the larger one had a calculated cross section of 860 square meters. The cross sections are for single, unique, chance aspects of each iceberg.

Based on a count of icebergs detected on a PPI display, the density of icebergs detectable by the test-bed radar was 4 per 100 square miles.

CONCLUSIONS

Large and small ship targets were detected with the airborne test-bed radar at steep and shallow grazing angles and in sea states of 1 to 5. Analysis of the data indicates that the primary objective of detecting a 200-square-meter fluctuating target with a 16-dB data-processor signal (clutter plus noise) ratio would be realized with the reference satellite radar sensor.

The analysis of experimental data from six ship targets, for a wide variety of grazing angles, relative aspects, and sea states, indicates that for scaled and equivalent performance the reference satellite-borne radar sensor would for these same ship targets have data-processor outputs for $S/(C + N)$ ratios ranging from 15.5 to 34.9 dB.

Data analysis indicates that for the interpulse intervals and scan rates used with the test-bed radar, the sea clutter was decorrelated. For the satellite system the data analysis indicates that the combination of the satellite orbital velocity and the scaled pulse-repetition frequency will result in equally decorrelated sea clutter.

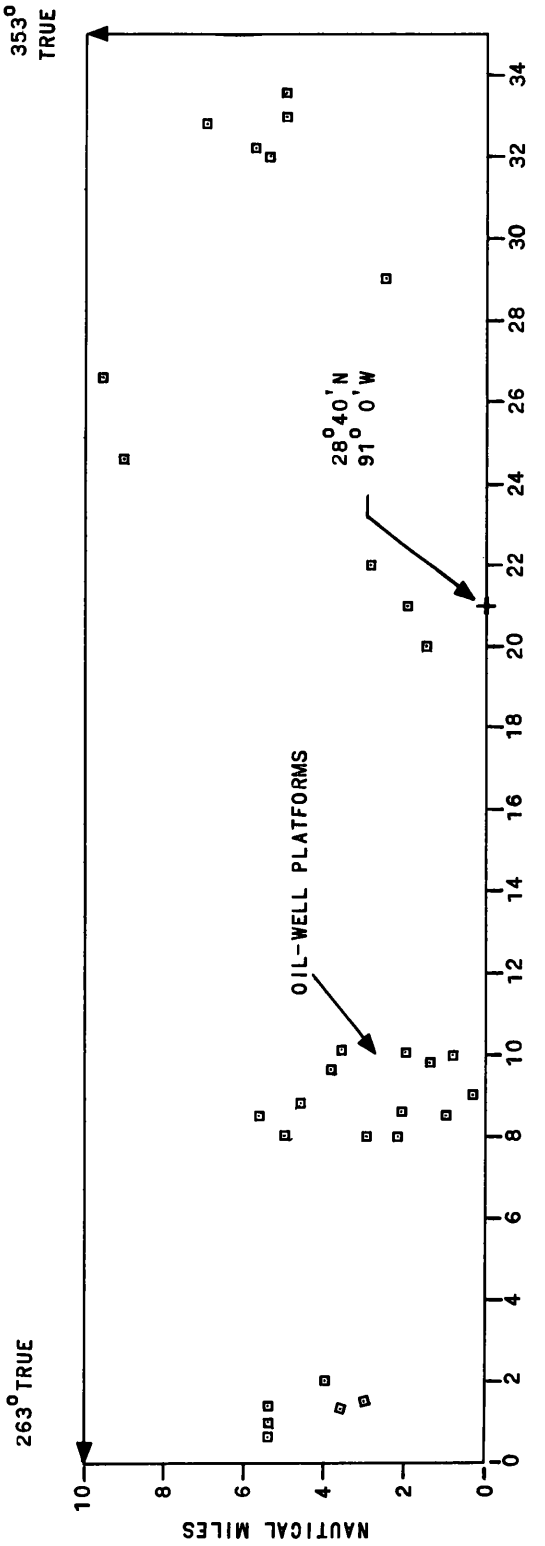

Fig. 33 (Unclassified)—Distribution of ocean oil-well platforms in the data acquisition area of the test-bed radar offshore from Louisiana (average water depth of 120 feet)

The radar cross sections measured with the test-bed radar are based on a pulse range resolution of 50 feet. A comparison of cross-section measurements made with the test-bed system with measurements made with other airborne L-band radar systems is valid only for those few targets that were small enough and oriented so as to be totally included within a single radar resolution cell. The required conditions did exist for two of the targets, and the results of those cross-section measurements are in good agreement with the results achieved with a calibrated precision radar.

Icebergs and ocean oil-well platforms are unique ocean surface targets that may constitute a real target-discrimination and data-handling problem for an ocean-surveillance radar sensor. Analysis of a limited data sample for each of these types of targets indicates that ship-sized radar cross sections are the normal expectation. The observed population densities in the areas sampled were 4 icebergs per 100 square miles in Newfoundland waters, and 9 oil wells per 100 square miles off the Louisiana coast. These densities are 100 to 300 times greater than the densities associated with worldwide surface-ship traffic.

REFERENCES

1. R.E. Ellis, editor, "Ocean Surveillance Radar Parametric Analysis," NRL Memorandum Report 1862
2. E.N. Carey and C.E. Fox, "Ocean Surveillance Radar Parametric Analysis, Case I — Forward Scan Radar," NRL Memorandum Report 1882
3. S. Angyal, D.F. Hemenway, and S.A. Zuro, "Ocean Surveillance Radar Parametric Analysis, Case II — Noncoherent Sidelooking Radar," NRL Memorandum Report 1874
4. R.K. Baldauf and A.E. Leef, "Ocean Surveillance Radar Parametric Analysis, Case III — Synthetic Aperture Sidelooking Radar," NRL Memorandum Report 1898
5. G.V. Trunk, "Ocean Surveillance Statistical Considerations," NRL Report 6804
6. J.M. Duls, "Graphical Analysis of Ocean Surveillance Radar Coverage," NRL Memorandum Report 1922
7. J.D. Wilson, "A Statistical Estimation of Aerospace Radar Ground Coverage," NRL Report 6790
8. R.L. Eilbert, S. Angyal, and S.A. Zuro, "Beam-Shaping Investigations for A Spaceborne Antenna," NRL Memorandum Report 1959
9. D.F. Hemenway and A.E. Leef, "Analysis of Low Frequency Clutter Characteristics and Target Detection Capabilities of A Synthetic Aperture Detection Radar (SADRAD)," NRL Memorandum Report 1954

10. R.L. Eilbert, "Radar System Scaling for Performance Evaluation," NRL Report 7125

11. "Lloyds Register of Ships," London, Lloyds Register Printing House, 1971.

12. G. Albrecht, "Weyer's Warships of the World," Annapolis, U.S. Naval Institute, 1971.

13. G.M. Jenkins and D.G. Watts, "Spectral Analysis and Its Applications," San Francisco, Holden-Day, 1968.

14. J.F. Diggs, J.A. Burkett, J.C. Daley, W.T. Davis, and J.T. Ransone, Jr., "Radar-Cross-Section Studies of Ships," NRL Report 7141

15. "Oceanographic Atlas of the North Atlantic, Section III, Ice," Naval Oceanographic Office, Publication 700, 1968.

APPENDIX A

THE TEST-BED RADAR

System Description

The test-bed radar system is composed of the five subsystem units identified in the following discussion.

Fig. A1 is a block diagram of the antenna subsystem, Unit 1. Pertinent performance characteristics of the two antennas are included in Table 2. The two antennas are shown in Fig. A2. The larger antenna consists of a parabolic cylinder with a 12-dipole collinear array feed. The smaller antenna is a 2-by-3-dipole-element array.

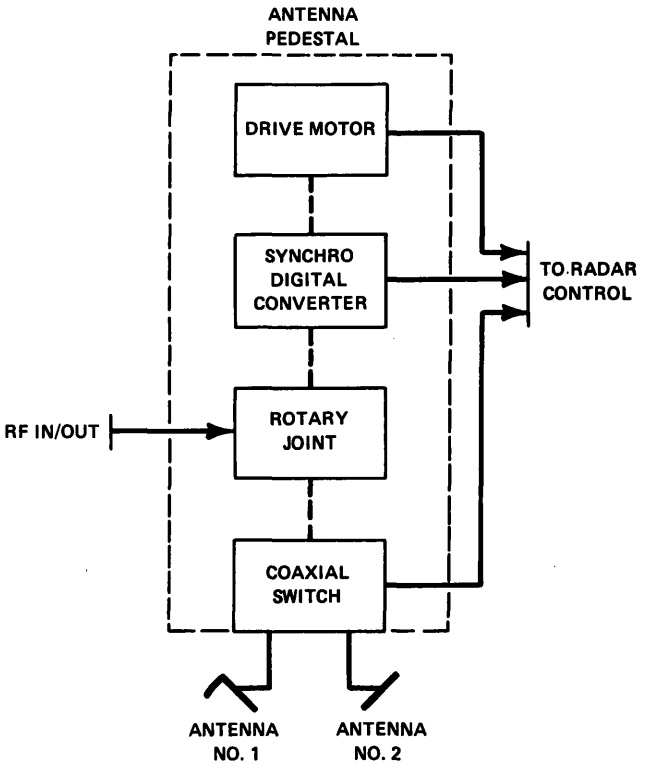

Fig. A1 (Unclassified)—Unit 1, the antenna subsystem

The two antennas are mounted back-to-back on the antenna pedestal and rotary joint (Fig. A3). The antenna subassembly was mounted in the lower radome of the EC-121 aircraft with a fixed tilt, so that with a nominal ±4.5° aircraft deck angle in flight the beam centers were at 1.5° amd 28° respectively for the large and small antennas. In

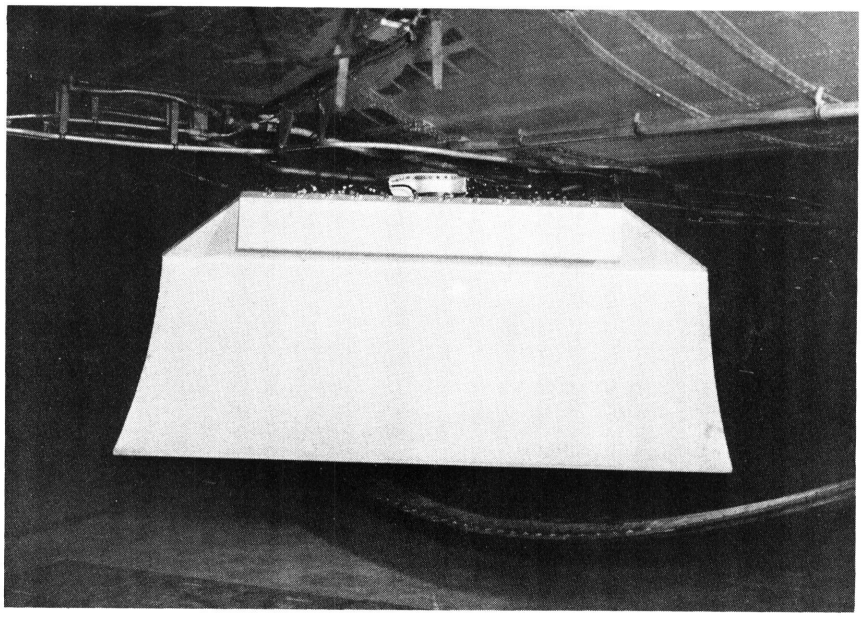

(a) The 12-dipole collinear-array-feed antenna used for shallow-grazing-angle data

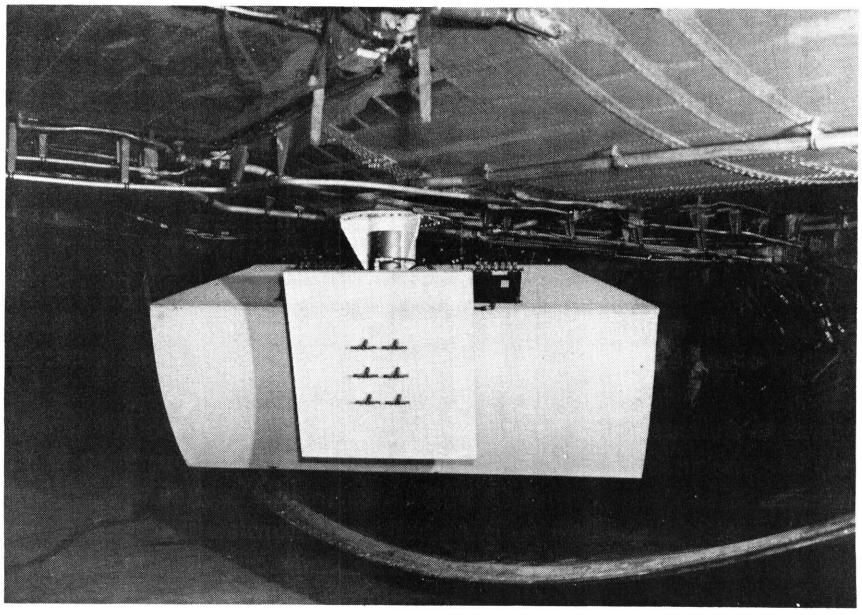

(b) The 2-by-3-element array used for steep-grazing-angle data

Fig. A2 (Unclassified)—The two antennas

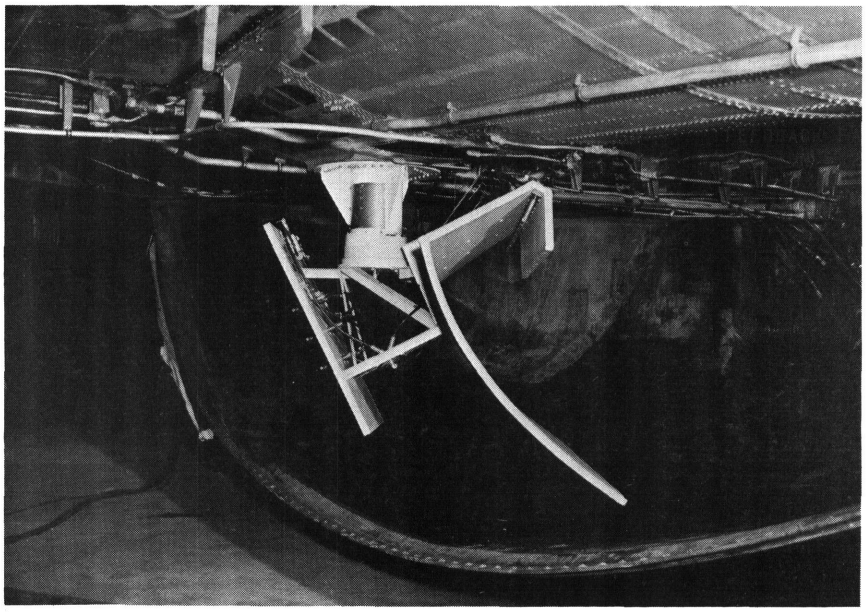

Fig. A3 (Unclassified)—The test-bed-radar antennas, pedestal, and rotary joint mounted on NRL EC-121K, BUNO 135753

flight only one antenna was used at a given time. A relay-actuated coaxial switch permitted selection and changeover in-flight of either antenna, with RF power on.

The antenna control and drive assembly permitted operation in one of three modes: continuous clockwise rotation, automatic sector scan, and manual control. Constant rotation rates were selectable from 0.5° to 60° per second.

The antenna-pedestal drive motor was equipped with a digital shaft encoder. The shaft encoder drove a digital antenna azimuth angle display at the radar control console. Pulse-width-coded antenna position was derived from the shaft data, mixed with the radar receiver video data, and recorded on the wideband magnetic tape recorder.

A block diagram of the system transmitter subassembly, Unit 2, is shown in Fig. A4. The 30-MHz stable crystal oscillator serves as the system master reference oscillator, providing outputs to the receiver subsystem, low-power transmitter stages, and the data processor subsystem. Several multiplier and mixer stages were used to develop the 1230-MHz transmitter frequency. Two stages of power amplification follow the final mixer. The first stage was a wideband, transistorized power amplifier, which provided 3 watts of peak power to drive the final stage, an electrostatically focused klystron (ESFK).

The output of the ESFK was a 20-microsecond chirp pulse with a 1230-MHz center frequency. The instantaneous bandwidth at the transmitter output was 15 MHz (3-dB point), and the peak output capability was 15 kilowatts.

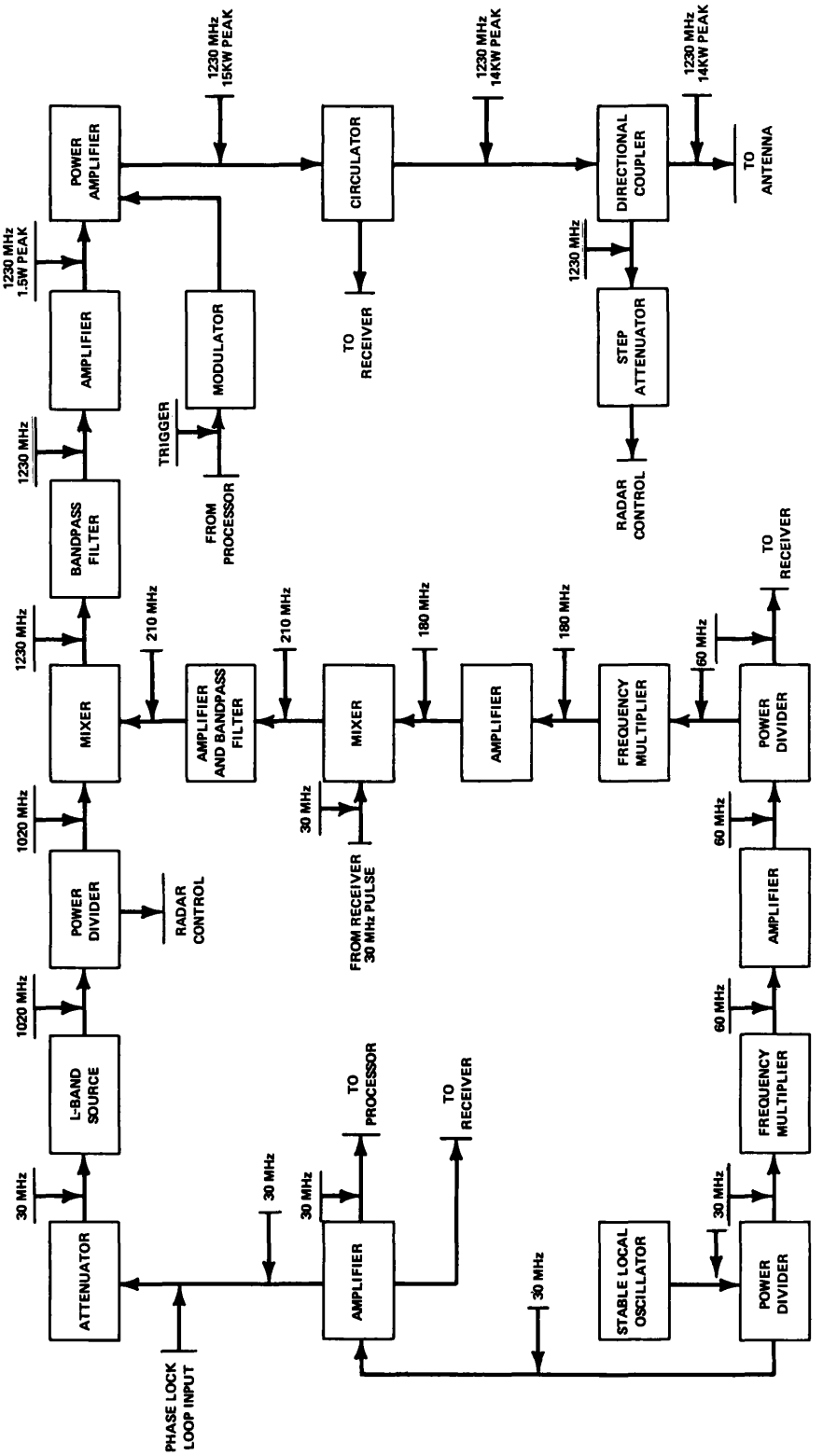

Fig. A4 —Unit 2, the transmitter subsystem of the test-bed radar

The ESFK was specifically developed for the test-bed radar both for providing the pulse power required for the airborne data acquisition and for obtaining experience and data for assessing a type of tube that was considered to have a potential for use in a space-borne radar sensor. Major parameters, specifications, and contractor test data for the ESFK are presented in Appendix B.

In normal use the transmitter was not operated at power levels above 6 kilowatts peak power. Effective transmitter power levels were reduced through reductions in the ESFK cathode voltage and through the use of calibrated attenuators in the receiver input line.

The receiver subsystem, Unit 3, is shown in Fig. A5. The first stage of the receiver was a wideband (1.0 to 2.0 GHz) low-noise (4.5 dB) traveling-wave-tube amplifier. The system noise figure, including line losses, the TWT noise figure, and the first-IF noise figure, was 10.9 dB.

Pulses were expanded and compressed with an Anderson Laboratories dispersive-delay-line assembly. The pulse expander and compressor used separate strip delay lines made from metal strips for the receiver expansion and compression channels. The center frequency of the unit was 30 MHz, the dispersive bandwidth was 14 MHz (3 dB), and the dispersion delay was 20 microseconds. The pulse expander output to the transmitter, Unit 2, was a gated and amplitude-limited pulse. In the receiver pulse-compression channel, limiting was not employed, but amplitude weighting of the received signal by hamming was used to achieve −35-dB suppression of range sidelobes and an effective pulse compression ratio of 200:1 with a 3-dB compressed pulse length of 0.1 microsecond.

The receiver minimum detectable signal, based on a measurement with a noncoherent, pulse, L-band signal source was approximately −105 dBm. Considering the matched-filter gain of 20 dB for the pulse-compression system, the receiver minimum detectable signal was approximately −125 dBm. The receiver bandwidths measured before and after pulse compression were 20 and 14 MHz respectively. The dynamic range of the complete receiver subsystem was 25 dB.

A block diagram for Unit 4, the system digital-data-processing subsystem is shown in Fig. A6. The processor derived all of the radar-system timing pulses from the 30-MHz signal generated by the transmitter stable local oscillator (Fig. A4). These timing pulses were in turn distributed from the processor to the transmitter, receiver, antenna, and control/monitoring subsystems. Within the processor, timing pulses were developed for each of the two PRF rates and for each of the 15 available processor range delays.

The radar video in the receiver was sampled at a 10-MHz rate by a high-speed analog-to-digital (A/D) converter. These samples were applied to a 1265-word integrator which accepted data for integration only over the time interval corresponding to the particular 10-mile range interval selected for data processing.

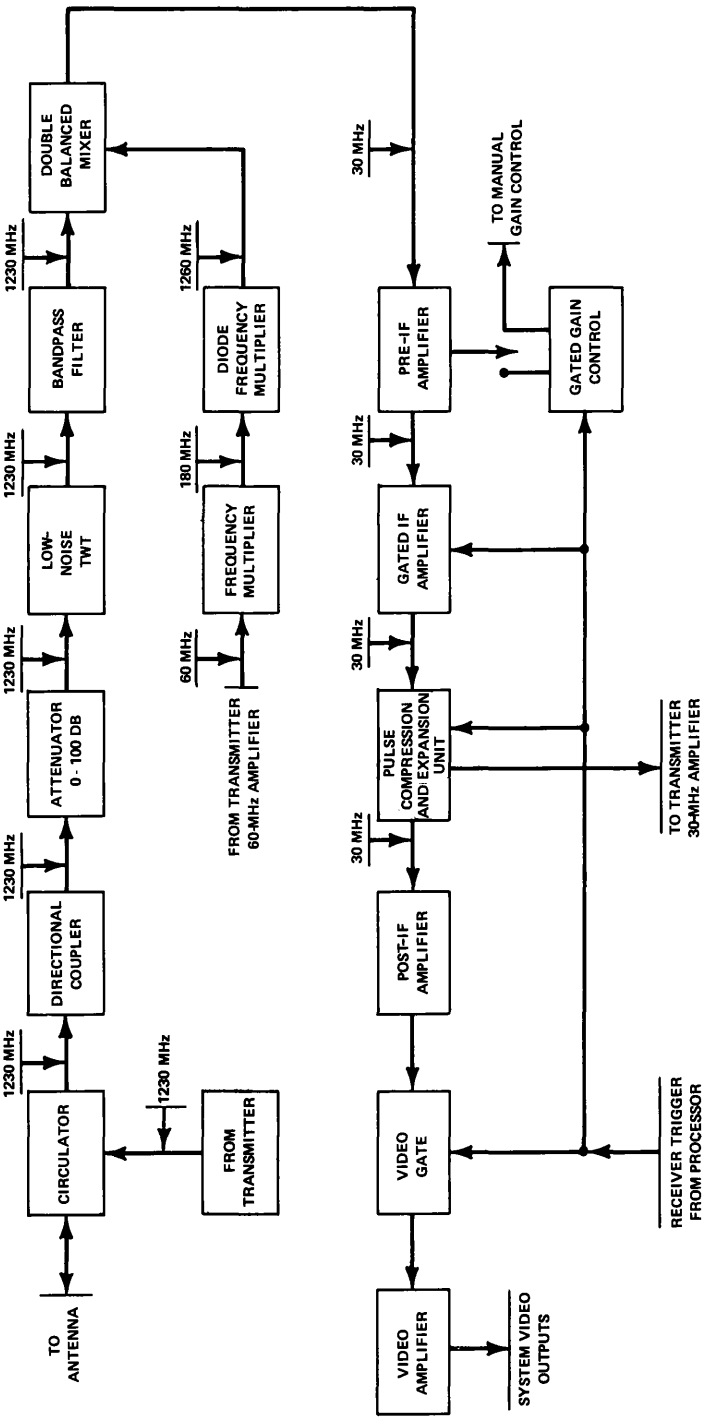

Fig. A5 —Unit 3, the receiver subsystem

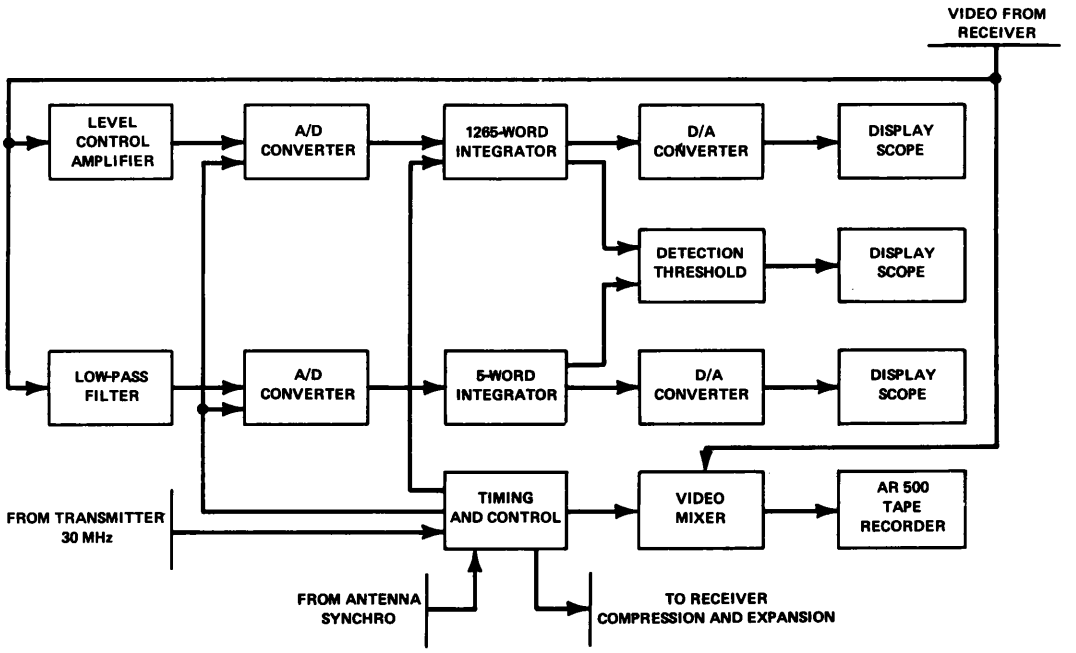

Fig. A6 —Unit 4, the digital-data processing subsystem

The radar video was also processed by a 40-kHz low-pass filter to provide an average clutter-plus-noise level, filtering out the effects of ship-sized targets which may have been present in the clutter sample.

In the detection-threshold circuitry the output of 1250-word signal integrator and the five-word clutter integrator were compared. A detection pulse was generated whenever the signal level was above a specified clutter threshold. Detailed circuit diagrams, descriptions, an analysis of the processor functions, and a discussion of subsequent data processing and analysis are the subject of NRL Report 7317 (A1).

A block diagram of Unit 5, the radar-system control and monitoring center is shown in Fig. A7. Included in this unit are the controls for the interface with the aircraft electrical system, controls for the solid-state inverters used as secondary power sources and as power conditioners, the radar system operating controls, the monitoring and calibration instrumentation and controls, photographic and magnetic tape recording equipment, and analog display equipment.

Aircraft and Radar Configuration

The test-bed radar was installed in an NRL Super Constellation aircraft, EC-121K, BUNO 135753 (Fig. A8). The aircraft was equipped with a standard APS-45 upper radome, APS-20 lower radome, and wing-tip tanks.

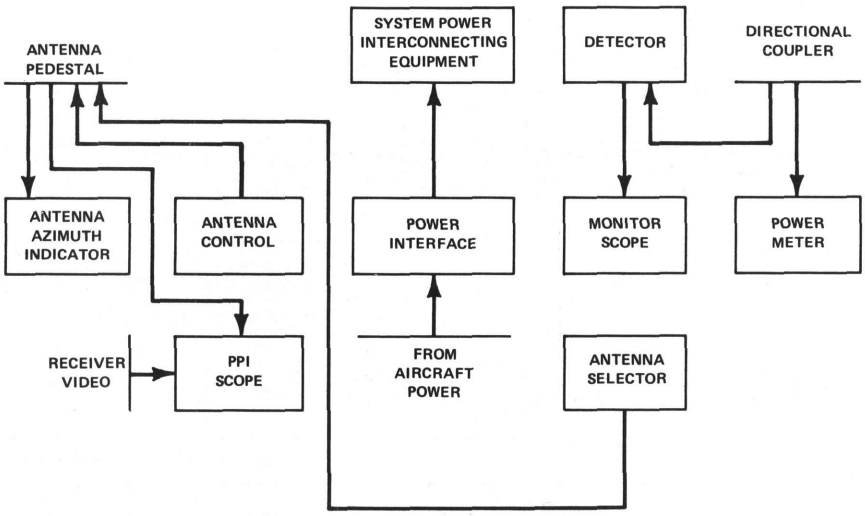

Fig. A7 (Unclassified)—Unit 5, the test-bed-radar control subsystem

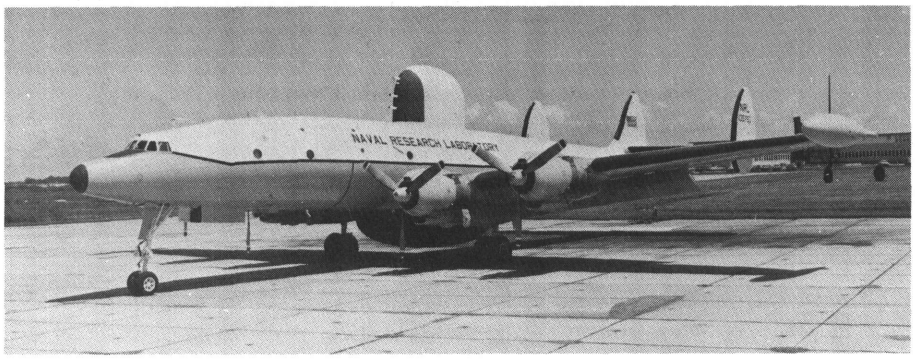

Fig. A8 (Unclassified)—The NRL EC-121K, BUNO 135753, used as a platform for the test-bed radar

Figure A9 shows the installed test-bed-radar equipment inside the aircraft. The system was assembled using a maximum of standard commercial components and subassemblies. As a consequence the test-bed system is not representative of materials, fabrication techniques, and packaging which would be used for a lightweight satellite-borne radar system.

The major units were the system control console and transmitter (355 lb), a high-voltage power supply and modulator (710 lb), a receiver and low-level exciter rack (375 lb), a data-processor rack (518 lb), a dual-mount antenna and pedestal (163 lb), a PPI (160 lb), and four solid-state frequency converters (86 lb each) for a total installed weight of 2625 pounds.

Total power requirements for the radar system and instrumentation were 3000 watts of single-phase, 60-hertz, 115-volt ac, 200 amperes of 28-volt dc, 1000 watts of single-phase, 400-hertz, 115-volt ac; and 1000 watts of three-phase, 400-hertz, 115-volt/phase ac.

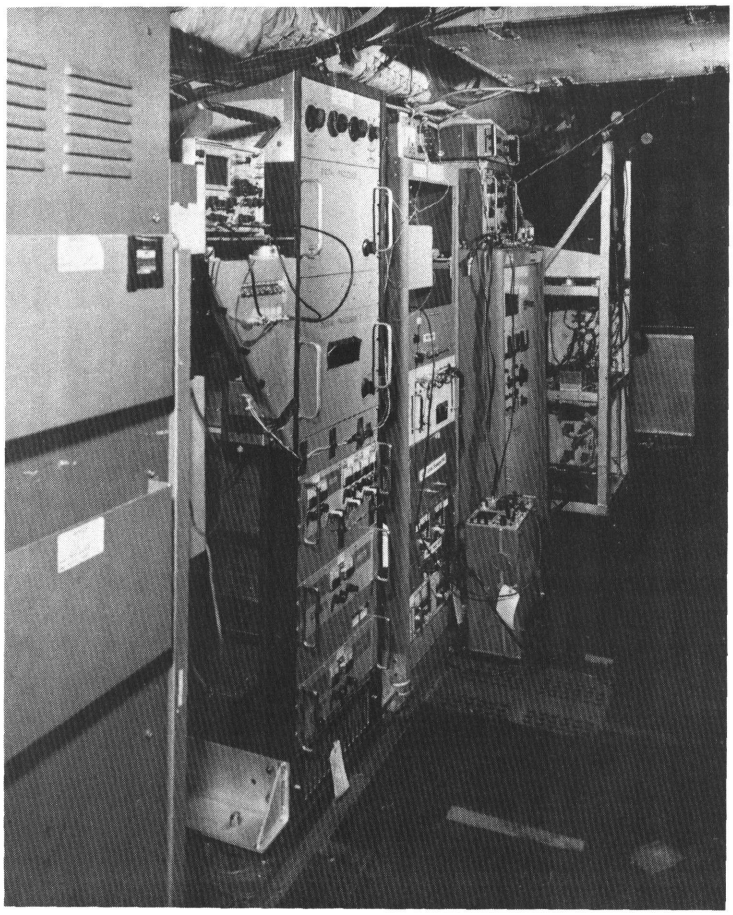

(a) View looking aft

Fig. A9 (Unclassified)—Aircraft installation of the test-bed radar

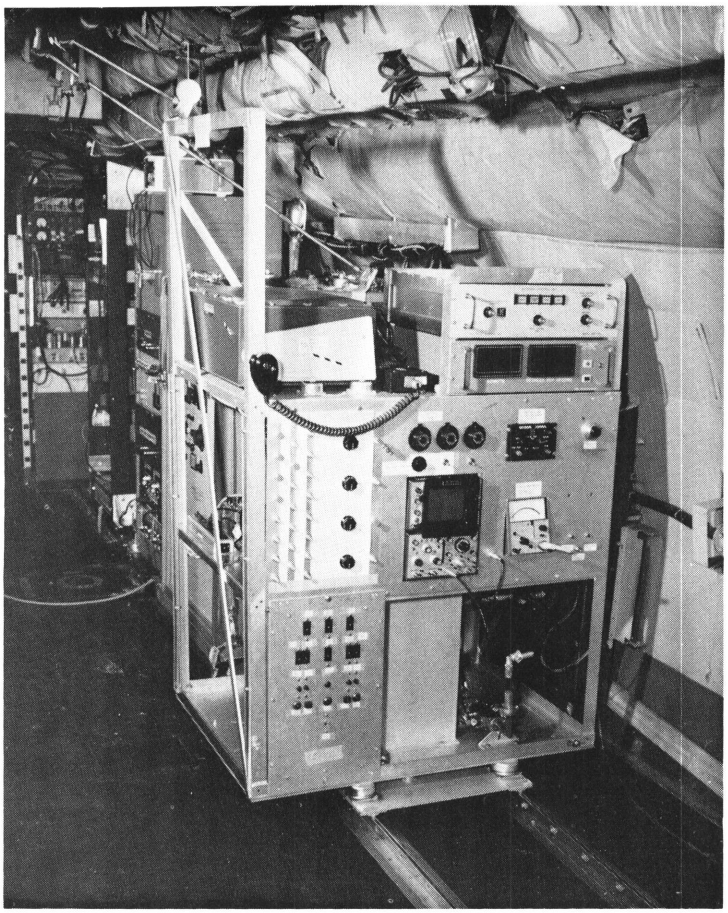

(b) View looking forward with the radar control console in the foreground

Fig. A9 (Unclassified)—Aircraft installation of the test-bed radar

APPENDIX A REFERENCE

A1. R.K. Baldauf and L.M. Leibowitz, "Digital Signal Processor for a Test-Bed Ocean Surveillance Radar," NRL Report 7317

APPENDIX B

THE LITTON INDUSTRIES ELECTROSTATICALLY FOCUSED KLYSTRON

Litton Industries developed two L-5428 electrostatically focused klystrons (ESFKs) for NRL use in the test-bed radar. The operating parameters and minimum performance goals for the tubes are compared with the test data in Table B1. The first klystron developed, tube S/N-1, though satisfactory for use in the test-bed radar, did not meet the goal specified for minimum gain and was marginal on bandwidth and efficiency. After the assembly and initial evaluation testing of S/N-1, Litton proposed that they be authorized to add an additional cavity to the original tube design to achieve better bandwidth, gain, and efficiency. The design change was authorized, and S/N-2 did result in significantly improved performance with a modest penalty of increased length and weight.

The Litton driver-modulator test set was not capable of being operated at the pulse lengths required for the test-bed radar, and all factory tests were performed with shorter pulse and higher repetition rates to demonstrate the peak and average power capabilities of the tubes. Additionally the Litton test set was not equipped for chirp modulation, and bandwidth performance was demonstrated with the pulsed CW RF drive being set at discrete frequencies.

Testing of the ESFKs at NRL and in the project aircraft disclosed serious problems. Both tubes suffered catastrophic failure through fractures of the ceramic windows in the coaxial output sections of the tubes. One failure (S/N-2) occurred at NRL, and the second failure (S/N-1) occurred on the aircraft. Tube disassembly, inspection, and failure analysis was performed by Litton. The failures resulted from the incorrect dimensioning of the center conductor of the coaxial output of the tube. The incorrect dimensioning resulted in overstressing of the ceramic window when commercial bullet connectors and external coaxial transmission lines were mated to the tube output connector. Both tubes were rebuilt by Litton under the warrantee provisions of the development contract. The rebuilt tubes were delivered with modified center conductors which have provided trouble-free service.

Both tubes exhibited objectionable in-band power instabilities at several discrete frequencies. NRL tests made with a pulsed CW drive revealed several discrete frequencies (one near the band center, 1232 MHz) for which power on a pulse-to-pulse basis varied by 3 to 6 dB. The discrete-frequency power instability was not evident when the chirp-modulated drive was applied to an ESFK.

Measurements of output power versus cathode voltage made at NRL did not satisfactorily approximate similar measurements reported by Litton. As an example Litton

Table B1 (Unclassified)
Litton Industries Test Data for Their Two L-J248 Electrostatically Focused Klystrons

Weight (lb)	Heater Voltage (V)	Heater Current (A)	Heater Power (W)	Cathode Voltage (kV)	Cathode Current (A)	Pulse Length (μsec)	Repetition Rate (pps)	Peak Drive Power (W)	Duty Cycle	Power Output		Gain (dB)	3-dB Bandwidth (MHz)	Test Frequency (MHz)	Efficiency (%)	Spurious Output Power (dB)	Second Harmonic Power (dB)	Input Capacitance (pF)
										Av (W)	Peak (kW)							
Specified by NRL																		
<35	12.5	5.2	65	21.0	3.2	20*	≤2000	3.0	0.007	100	>15.0	40	13.0	1230	25.0	−60.0	−30.0	no spec
Tube S/N-1 (five cavities; 19.5 in. long overall)																		
28.0	12.3	4.3	53.0	20.0	2.95	14.0*	451	3.0	0.0063	100.0	15.85	37.2	13.5	1230	26.9	−60.0	−40.0	95.0
Tube S/N-2 (six cavities; 21.85 in. long overall)																		
31.0	12.5	4.25	53.0	20.0	3.0	14.0*	343	1.77	0.0047	86.9	18.65	40.2	15.5	1230	31.1	−58.0†	−30.0	107

*The Litton test stand was not capable of operation with 20-μsec pulse lengths.
†At the limit of measurement sensitivity.

reported a peak power output of 21.3 kW with a 20-kV cathode voltage for S/N-1, whereas the highest output measured at NRL was 14 kW with a 21.5-kV cathode voltage. The major difference between the NRL and Litton test sets was that Litton conducted tests with a 14-microsecond pulse length and pulse repetition rates of 343 and 451 pulses per second, whereas NRL tests were conducted with a 20-microsecond pulse length and a repetition rate of 62.5 pulses per second.

Time has not permitted a verification of the aging characteristics of both tubes, but tube S/N-2 has exhibited a serious aging characteristic. During the initial periods of use, the application of a fixed level of cathode voltage immediately resulted in a stable level of power output. After 200 hours of operating time including over 100 airborne hours the initial application of a fixed level of cathode voltage would be followed by a 20 to 25 minute period before the power output reached stable operation.

During the phase of the program reported here the total operating time accumulated on the two tubes during use at NRL or in the project aircraft was 411 hours.

APPENDIX C

SCALED ANTENNA SPEEDS AND PEAK POWERS

Figures C1 and C2 are nomographs giving the values of antenna rotation speeds for the test-bed radar that are scaled to the sweep of the proposed satellite-borne ocean-surveillance radar. The two figures are for the two test-bed-radar subsystems scaled for the two most critical regions, Fig. C1 being for the steepest grazing angles and Fig. C2 being for the shallowest grazing angles. Tables C1 and C2 give the peak power values scaled for these regions.

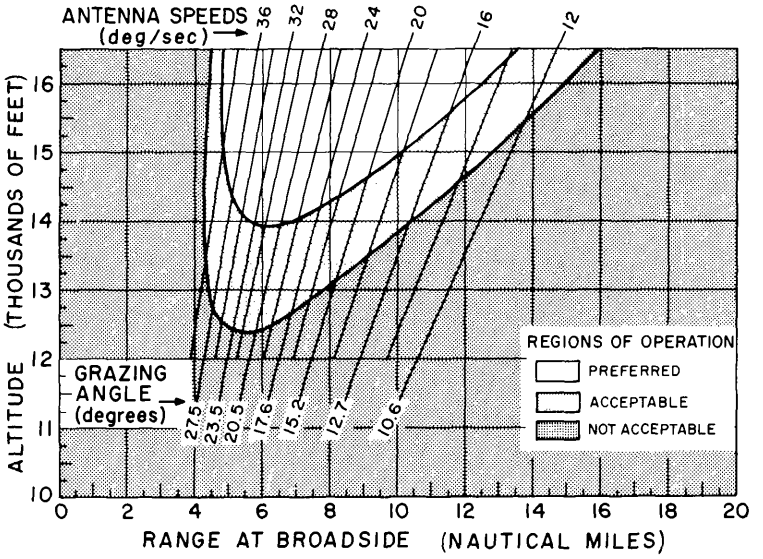

Fig. C1 —Antenna rotation speeds for the test-bed-radar subsystem scaled for the near-range steep grazing angles of a satellite-borne radar

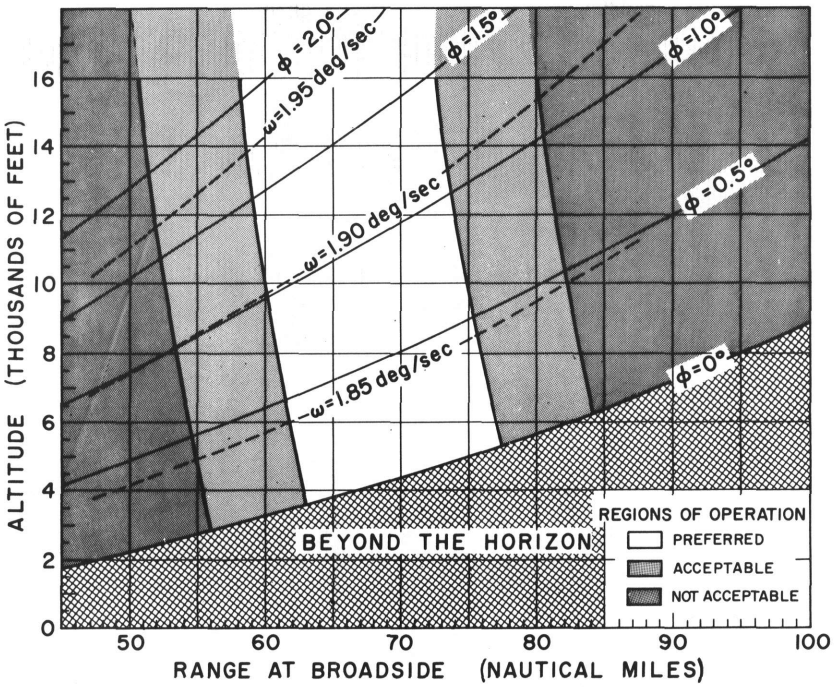

Fig. C2 —Antenna rotation speeds ω for the test-bed-radar subsystem scaled for the far-range shallow grazing angles ϕ of a satellite-borne radar

Table C1
Values of the Peak Power for the Steep-Grazing-Angle Subsystem at the Closest Approach to a Target with a Radar Cross Section of 200 Square Meters as Scaled to the Values for a Satellite-Borne Radar. The shadings correspond to the legend within Fig. C1.

Altitude (ft)	Power at Various Slant Ranges in Nautical Miles When the Aircraft is Closest to the Target (W)															
	4.5	5.0	5.5	6.0	6.5	7.0	7.5	8.0	8.5	9.0	10.0	11.0	12.0	13.0	14.0	15.0
16,000	58	73	80	98	125	162	210	266	336	426	675	1044	1570	2294	3267	4544
15,500	68	63	74	93	120	158	206	261	334	426	683	1061	1600	2343		
15,000	55	55	68	89	117	155	201	259	334	429	692	1081	1635			
14,500	46	51	64	85	114	153	198	258	335	433	704	1104				
14,000	38	47	61	83	112	149	196	259	338	439	718					
13,500	34	44	59	81	111	147	196	261	343	447						
13,000	31	41	57	79	108	146	195									
12,500		39	55	78												
12,000																

Table C2
Values of the Peak Power for the Shallow-Grazing-Angle Subsystem at the Closest Approach to a Target with a Radar Cross Section of 200 Square Meters as Scaled to the Values for a Satellite-Borne Radar

Altitude (ft)	Power at Various Slant Ranges in Nautical Miles When the Aircraft is Closest to the Target (W)															
	52	54	56	58	60	62	64	66	68	70	72	74	76	78	80	82
16,000	2.80	3.25	3.84	4.41	5.05	5.76	6.54	7.58	8.55	9.62	10.78	12.05	13.81	15.37	17.06	
15,000	2.77	3.21	3.81	4.38	5.02	5.72	6.49	7.54	8.51	9.58	10.74	12.01	13.78	15.34	17.04	
14,000	2.74	3.18	3.78	4.35	4.98	5.68	6.45	7.51	8.48	9.54	10.70	11.97	13.76	15.32	17.01	
13,000	2.71	3.15	3.75	4.32	4.95	5.65	6.42	7.48	8.45	9.51	10.67	11.93	13.75	15.31	17.00	
12,000	2.69	3.12	3.72	4.29	4.92	5.62	6.39	7.46	8.42	9.48	10.64	11.90	13.74	15.30	16.99	
11,000		3.10	3.70	4.27	4.89	5.59	6.36	7.44	8.40	9.46	10.62	11.88	13.74	15.30	16.99	
10,000		3.08	3.68	4.25	4.87	5.57	6.33	7.42	8.38	9.44	10.60	11.86	13.74	15.30	17.00	18.83
9,000		3.06	3.67	4.23	4.86	5.55	6.31	7.41	8.37	9.43	10.58	11.85	13.75	15.31	17.01	18.84
8,000		3.05	3.66	4.22	4.84	5.53	6.30	7.40	8.36	9.42	10.58	11.84	13.76	15.33	17.02	18.86
7,000		3.03	3.65	4.21	4.83	5.52	6.28	7.40	8.36	9.42	10.57	11.83	13.78	15.35	17.05	18.89
6,000			3.64	4.20	4.82	5.51	6.27	7.40	8.36	9.42	10.57	11.84	13.81	15.38	17.08	18.92
5,000			3.64	4.19	4.82	5.50	6.27	7.40	8.37	9.42	10.58	11.84	13.83	15.38	17.04	18.85

APPENDIX D (Unclassified)

DEFINITION OF UNITS IN EQUATION (1)

INTRODUCTION

The levels of RF power shown in Tables C1 and C2 were calculated in a computer program using Eq. (1), a version of the basic radar equation. Certain parameters which appear as factors in the equation should be discussed in detail. These are the antenna gain (G), the system transmitting losses (L), and the receiving system noise power (N_0).

ANTENNA GAIN, G

The values of the antenna gain at beam center for the two subsystems were listed in Table 2: 13.3 dB for the steep-grazing-angle system and 22.2 dB for the shallow-grazing-angle system. Since, in general, the target was not at the depression angle which corresponds to beam center, it was necessary to take into account the effect of the vertical pattern on antenna gain. For this purpose the following function was used to approximate the real antenna power pattern:

$$G = \frac{\pi^4}{16} \left[\frac{\cos^2 x}{\left(\frac{\pi^2}{4} - x^2 \right)^2} \right] G_0, \tag{D1}$$

where G_0 is the antenna gain at beam center and

$$x = F \sin (\psi_0 - \psi)$$

in which F is a factor relating to antenna size, ψ_0 is the depression angle to the beam center, and ψ is the depression angle to the target.

Equation (D1) describes the pattern of a rectangular aperture with a cosine-tapered illumination and sidelobes of approximately 25 dB. To relate this gain function to the actual vertical power pattern, the factor F was evaluated so that the theoretical relative

---

Note: This appendix is essentially the same as Appendix A in Ref. D1.

gain matched the actual relative gain at the half-power points of the pattern. That is, the following equation was solved for F:

$$\frac{G}{G_0} = \frac{\pi^4}{16}\left[\frac{\cos\left(F\sin\frac{\gamma_0}{2}\right)}{\frac{\pi^2}{4} - \left(F\sin\frac{\gamma_0}{2}\right)^2}\right]^2 = 0.5, \tag{D2}$$

in which γ_0 is the measured vertical half-power beamwidth of the antenna.

Equation (D2) yielded $F = 11.03$ for the shallow-grazing-angle subsystem and $F = 5.74$ for the steep-grazing-angle subsystem. Using these factors, Eq. (D1) was then solved for antenna gain for the appropriate value of depression angle.

SYSTEM TRANSMITTING LOSSES, L

The losses on transmission enter into the loss factor L in the denominator of the radar equation. Table D1 lists these losses for both subsystems and notes (under "Justification") how the loss values were obtained. As indicated by the table the tropospheric absorption was a constant for the steep-grazing-angle subsystem. However, at shallow grazing angles this loss factor did vary, both with grazing angle and with range. Table D2 shows values for the tropospheric loss factor in the region of interest. These values were obtained from curves presented in Ref. D2. For determining the tropospheric loss in the computer program, equations were used which gave straight-line approximations to these values with grazing angle as the dependent variable.

Table D1
System Transmission Losses for the Shallow-Grazing-Angle Subsystem and the Steep-Grazing-Angle Subsystem

Loss	Symbol	Magnitude of Loss (dB)		Justification
		Shallow Angle	Steep Angle	
Transmission line*	L_t	1.75	1.75	By measurement
Antenna pattern	L_p	1.60	1.60	Ref. D2
Radome (two-way)†	L_d	1.00	1.00	Calculated (Ref. D3)
Tropospheric absorption	L_α	See Table D2	0.10	Fig. 22 in Ref. D2

*Transmission-line loss from the antenna terminals to the directional coupler where the transmitter power is monitored.

†To be rigorous, only half the total radome loss should be applied here and the other half should be accounted for in the receiving-system noise temperature calculation. For the sake of simplicity, however, the entire loss is applied here.

Table D2
Two-Way Tropospheric Absorption at
1230 MHz and Shallow Grazing Angles

Range (n.mi.)	Absorption (dB)			
	0°	0.5°	1.0°	2.0°
50	1.05	0.95	0.90	0.80
60	1.20	1.15	1.05	0.90
70	1.40	1.30	1.20	1.00
80	1.60	1.45	1.30	1.10

RECEIVING-SYSTEM NOISE POWER, N_0

The losses in the receiving system are accounted for in terms of the receiving-system noise power N_0. Blake (D2) discusses the concept of system noise temperature, which is related to system noise power by the equation

$$T_s = \frac{P_n}{k B_n} = \frac{N_0}{k}, \tag{D3}$$

in which T_s is the overall receiving-system noise temperature, P_n is the available noise power of the receiving system, B_n is the noise bandwidth of the receiver, k is Boltzmann's constant (1.3805 watt-sec/K°), and N_0 is the noise power per unit bandwidth, the form of the parameter as used in the radar equation.

As Blake shows, each of the components of the receiving system contributes its own effective noise temperature, so that the overall system noise temperature is

$$T_s = T_a + T_r + L_r T_e, \tag{D4}$$

in which T_a is the antenna noise temperature, T_r is the transmission-line noise temperature, L_r is the transmission-line loss factor, and T_e is the noise temperature of the receiver.

Antenna Noise Temperature

If the sea is assumed to be a perfect (not necessarliy specular) reflector at 1230 MHz, then the effective noise-temperature contribution from the antenna is

$$T_a = \frac{T'_a + 290(L_a - 1)}{L_a}, \tag{D5}$$

in which L_a is the loss in the antenna, estimated to be 0.6 dB (or a loss factor of 1.15) for both subsystems and T'_a is the temperature of extraterrestrial noise sources as given by Fig. 11 in Ref. D2. For shallow grazing angles (approximately 1°)

$$T'_a = 65°K,$$

and for steep grazing angles (approximately 25°)

$$T'_a = 22°K.$$

After substituting the appropriate values into Eq. (D5), the resultant antenna noise temperature was found to be $94°K$ for the shallow-grazing-angle subsystem and $57°K$ for the steep-grazing-angle subsystem.

Transmission-Line Noise Temperature

For a transmission line with a loss factor L_r the noise temperature is

$$T_r = 290(L_r - 1). \tag{D6}$$

The measured line loss between the antenna and the receiver in the test-bed system was 5.9 dB, corresponding to a loss factor of 3.89 (the antilog of 5.9/10). Using this value in Eq. (D6), the transmission-line noise temperature was found to be $838°K$ (for both subsystems).

Noise Temperature of the Receiver

The effective noise temperature of a receiver with a noise factor NF is

$$T_e = 290(NF - 1). \tag{D7}$$

The receiver used in the airborne test-bed system had a noise figure of 4 dB, which corresponds to a factor of 2.51. Thus from Eq. (D7) the receiver had a noise temperature of $438°K$.

Overall System Noise Power

Substituting the preceding component noise temperatures into Eq. (D4), values for system noise temperature were found for each of the subsystems. The product of system noise temperature and Boltzmann's constant gave the overall system noise power per unit bandwidth N_o. The results are listed in Table D3.

Table D3
System Noise Power

Subsystem	System Noise Temperature (°K)	Noise Power Per Unit Bandwidth (watt-sec)
Shallow grazing angle	2636	3.639×10^{-20}
Steep grazing angle	2599	3.588×10^{-20}

THE CALCULATION OF RF POWER

To calculate the RF power required in the test-bed system for simulating the detection performance of the reference system, the form of the radar equation given as Eq. (1) was used, namely,

$$P_{av} = \frac{K\,(4\pi)^3\,\tau_c\,B_n\,N_0\,(PRF)\,R_s^4\,\left(\frac{S}{C+N}\right)_n\,L}{G^2\,\lambda^2\,S_i(n)\left[\sigma_T - \frac{\sigma_c\left(\frac{S}{C+N}\right)_n}{S_i(n_c)}\right]}. \tag{D8}$$

To convert to pulse power, which is the parameter that was monitored in the test-bed system, the following supplemental equation was used:

$$P_p = \frac{P_{av}}{\tau_c\,(PRF)\,(PCR)}. \tag{D9}$$

The symbols in these equations have the following definitions and values:

P_{av} = average transmitter power in watts.

P_p = pulse power in kilowatts which corresponds to the calculated average power.

K = (1852 meters/nautical mile)^4 = 11.76424×10^{12}.

$(4\pi)^3 = 1.984402 \times 10^3$.

τ_c = compressed pulselength in seconds.

B_n = receiver noise bandwidth in hertz.

$\tau_c B_n = 1$.

N_0 = receiving system noise power per unit bandwidth (discussed previously in this appendix) in watts per hertz.

(PRF) = the pulse repetition frequency in pulses per second

= 39.0 pps for the shallow-grazing-angle subsystem

= 62.5 pps for the steep-grazing-angle subsystem

R_s = radar slant range in nautical miles.

$\left(\frac{S}{C+N}\right)_n$ = integrated signal (clutter plus noise) ratio required for a probability of detection of 0.90 for fluctuating targets and a probability of false alarm of 10^{-1°. This ratio is a function of integration time. In the computer program the required value of $S/(C + N)$ was calculated from equations based on Fig. 10 of Ref. D4.

L = system transmitting losses (Table D1).

G = antenna gain (discussed previously in this appendix).

λ = wavelength in meters

= 0.24373 (1230 MHz).

$S_i(n)$ = integration improvement factor. The following equations are approximations to Fig. 2.24 in Ref. D5; these equations give values for the integration improvement factor when n pulses are integrated:

$= 1.01\, n^{0.944}, \; 1 \leqq n < 4,$

$= 1.282\, n^{0.775}, \; 4 \leqq n < 20,$

$= 1.675\, n^{0.688}, \; 20 \leqq n < 100,$

$= 2.59\, n^{0.593}, \; n \geqq 100,$

in which

$n = (\theta/\omega)\,(PRF),$

where θ is the effective azimuth beamwidth in radians and ω is the rotational velocity of the antenna in radians per second.

σ_T = the average cross section of a fluctuating target in square meters

= 200 square meters in this analysis.

σ_c = effective radar cross section of sea clutter within a resolution cell

$$= \sigma_0 K_1 R_s \theta \frac{c \tau_c}{2} \sec \phi,$$

in which

σ_0 = backscattering coefficient of the sea, which is dependent on frequency and grazing angle,

K_1 = conversion factor between square nautical miles and square meters

$= 3.429904 \times 10^6 \ m^2/(\text{n.m.i.})^2$,

R_s = slant range in nautical miles,

c = speed of light

$= 1.61875 \times 10^5$ n.m.i./sec, and

ϕ = grazing angle at the earth's surface

$$= \arccos\left(\frac{\cos \psi \ (r_e + h)}{r_e}\right),$$

where

r_e = earth radius

= 3440.0 n.m.i.

h = aircraft altitude in nautical miles, and

ψ = depression angle measured at the radar platform.

$S_i(n_c)$ = integration improvement factor modified from $S_i(n)$ for partial correlation of sea clutter. When the product of the decorrelation time (T_d) and pulse repetition frequency (PRF) is less than unity (no correlation between pulses), $S_i(n_c) = S_i(n)$ as defined previously. When $T_d \times (\text{PRF}) > 1$ (partial correlation between pulses), $S_i(n_c)$ is determined from $S_i(n)$ with

$$n_c = n/[T_d(\text{PRF})],$$

where

T_d = decorrelation time

$= \lambda/(\theta\ V_t)$,

in which

V_t = velocity of aircraft

= 311 feet/sec.

PCR = pulse compression ratio

= 200

APPENDIX D REFERENCES

D1. R.L. Eilbert and S.A. Zuro, "Operating Guidelines for the Airborne Radar Test System," NRL Memorandum Report 2260 (Secret report, Unclassified title), Apr. 1971.

D2. L.V. Blake, "A Guide To Basic Pulse-Radar Maximum-Range Calculation, Part 1—Equations, Definitions, and Aids to Calculation," NRL Report 6930 (Unclassified), Dec. 23, 1969.

D3. S. Wolin, "Tables of Transmission and Reflection Coefficients of Lossy, Symmetrical Dielectric Radome Sandwiches," NADC-EL-52188 (Unclassified), Oct. 22, 1953.

D4. G.V. Trunk, "Ocean Surveillance Statistical Considerations," NRL Report 6804 (Secret Report, Unclassified title), Nov. 1968.

D5. M.I. Skolnik, "Introduction to Radar Systems," McGraw-Hill, 1962.

Security Classification

DOCUMENT CONTROL DATA - R & D

(Security classification of title, body of abstract and indexing annotation must be entered when the overall report is classified)

1. ORIGINATING ACTIVITY *(Corporate author)* Naval Research Laboratory Washington, D.C. 20390	2a. REPORT SECURITY CLASSIFICATION 2b. GROUP 3

3. REPORT TITLE

Analysis of Experimental Data from a Scaled Ocean-Surveillance Radar

4. DESCRIPTIVE NOTES *(Type of report and inclusive dates)*

An interim report on a continuing NRL Problem

5. AUTHOR(S) *(First name, middle initial, last name)*

D.F. Hemenway

6. REPORT DATE	7a. TOTAL NO. OF PAGES	7b. NO. OF REFS
March 7, 1972	76	20

8a. CONTRACT OR GRANT NO.	9a. ORIGINATOR'S REPORT NUMBER(S)
NRL Problem R02-46 b. PROJECT NO. PM 16-40 058C 2W44150000 c. d.	NRL Report 7388 9b. OTHER REPORT NO(S) *(Any other numbers that may be assigned this report)*

10. DISTRIBUTION STATEMENT

11. SUPPLEMENTARY NOTES	12. SPONSORING MILITARY ACTIVITY
	Department of the Navy Navy Material Command, Navy Space Project Office— PM-16, Washington, D.C. 20360

13. ABSTRACT

(U) To validate various theoretical models used in the design and specification of a proposed satellite-borne, ship-detection, ocean-surveillance radar, an airborne test-bed radar system has been developed and used to acquire experimental data. The major operating and performance parameters of the test-bed radar are either identical to or are scaled to the equivalent parameters of the satellite sensor.

(S) The analysis of experimental data acquired with the test-bed radar indicates that the satellite radar system should meet the objective of automatically detecting ship targets with radar cross sections equal to or greater than 200 square meters. The analysis of the experimental data covers a variety of ships, ship aspects, ship lengths, sea states, and grazing angles. All of the ship-target data analyzed resulted in measures of processed-radar-video signal/(clutter plus noise) ratios ($S/(C + N)$) greater than 16 dB. The same data normalized for a satellite sensor system indicates that the 16-dB $S/(C + N)$ required for automatic detection would be realized for 200-square-meter ship targets.

(U) The experimental data confirm that for the 0.016-second interpulse time period the sea clutter is for practical purposes completely decorrelated.

DD FORM 1 NOV 65 1473 (PAGE 1)

S/N 0101-807-6801

Security Classification

14. KEY WORDS	LINK A		LINK B		LINK C	
	ROLE	WT	ROLE	WT	ROLE	WT
Radar detection						
Ocean surveillance						
Airborne radar						
Scaling						
Radar cross section						
Ships						
Icebergs						
Off-shore drilling rigs						
Sea clutter						
Autocorrelation coefficients						
Signal-to-clutter-plus-noise ratios						
Power spectrum						